ABSTRACT

Title of dissertation: LARGE-EDDY SIMULATION OF HIGH REYNOLDS NUMBER FLOWS IN COMPLEX GEOMETRIES

Senthil Radhakrishnan
Doctor of Philosophy, 2007

Dissertation directed by: Professor Ugo Piomelli
Department of Mechanical Engineering

Large-eddy simulation (LES) of wall-bounded flows is limited to moderate Reynolds number flows due to the high computational cost required to resolve the near wall eddies. LES can be extended to high Reynolds number flows by using wall-layer models which bypass the near-wall region and model its effect on the outer region. Wall-layer models based on equilibrium laws yield poor prediction in non-equilibrium flows, in which Wall-Modeled LES (WMLES) that model the near wall region by Reynolds-Averaged Navier-Stokes (RANS) equation and the outer region by LES, has the potential to yield better results. However, in attached equilibrium flows, WMLES under-predicts the skin friction due to slow generation of resolved eddies at the RANS/LES interface; application of stochastic forcing results in faster generation of resolved eddies and improved predictions. In this work, wall-layer models based on equilibrium laws and WMLES are tested for four non-equilibrium flows.

Flow over a contoured ramp, with a shallow separation followed by a recovery region, was studied. LES using equilibrium laws was unable to resolve the shallow separation. WMLES predicted the mean velocity reasonably well but over-predicted the Reynolds stresses in the separation and recovery region; application of the stochastic forcing corrected this error. Next, the flow past a two-dimensional bump, in which curvature and pressure-gradient effects dictate the flow development, was studied. WMLES predicted the mean velocity accurately but over-predicted the Reynolds stresses in the adverse pressure gradient region; application of the stochastic forcing also corrected this error. Same trends were seen in a three-dimensional flow studied. A turbulent oscillating boundary layer was also investigated. WMLES was found to be excessively dissipative, which resulted in incorrect prediction of the flow development. LES calculation based on equilibrium laws and dynamic models predicted the flow development correctly. In summary, in flows that are steady in the mean, WMLES with stochastic forcing gave more accurate results than the logarithmic law or RANS. For the oscillating boundary layer, in which stochastic forcing could not be applied, the logarithmic law yielded the best results.

LARGE-EDDY SIMULATION OF HIGH REYNOLDS NUMBER FLOWS IN COMPLEX GEOMETRIES

by

Senthilkumaran Radhakrishnan

Dissertation submitted to the Faculty of the Graduate School of the
University of Maryland, College Park in partial fulfillment
of the requirements for the degree of
Doctor of Philosophy
2007

Advisory Committee:
Ugo Piomelli, Professor (Chair)
Elias Balaras, Associate Professor
Richard Calabrese, Professor (Dean's Representative)
Kenneth Kiger, Associate Professor
Arnaud Trouvé, Associate Professor

ACKNOWLEDGMENTS

I would like to express my sincere gratitude to my advisor Professor Piomelli for his guidance and encouragement during the course of this work. I would like to thank Professor Elias Balaras who co-advised me initially when I started working on this project.

I would like to sincerely thank all the committee members: Professors Elias Balaras, Richard Calabrese, Ken Kiger and Arnaud Trouvé for spending their valuable time.

I am extremely grateful to Dr. Alexandre Silva Lopes who provided the original finite volume code and explained various aspects of the code and large-eddy simulation patiently. I would like to thank Victor Ovchinnikov for his friendship and all the help he provided. Thanks are also due to other members of CFD laboratory: Nikolaos Beratlis, Vincenzo Pezza, Marcos Vanella and Luis Bravo.

This work was supported by the Office of Naval Research under Grant Number N00014-03-1-0491, and by the National Science Foundation under Grant Number 0452380. The Department of Mechanical engineering supported me as a Teaching Assistant for three semesters.

Table of Contents

List of Tables

List of Figures

NOMENCLATURE

Abbreviations

DES	Detached Eddy Simulation
DNS	Direct Numerical Simulation
FV	Finite Volume
LES	Large Eddy Simulation
LDEV	Lagrangian Dynamic Eddy Viscosity
MPI	Message Passing Interface
NS	Navier-Stokes
RANS	Reynolds-Averaged Eddy Simulation
RST	Reynolds Stress Transport
SA	Spalart Allmaras
SDLDEV	Scale-Dependent Lagrangian Dynamic Eddy Viscosity
SST	Shear Stress Transport
WMLES	Wall Modeled Large Eddy Simulation

Roman symbols

C_f	Skin-friction coefficient
C_p	Pressure coefficient
Re_θ	Reynolds number based on boundary layer momentum thickness, θ
$R_{uu,x}$	Streamwise correlation of the u-velocity
$R_{vv,x}$	Streamwise correlation of the v-velocity
$R_{uu,y}$	Wallnormal correlation of the u-velocity
$R_{vv,y}$	Wallnormal correlation of the v-velocity
S_{ij}	Strain-rate tensor
U_∞	Free-stream velocity
k_o	Roughness length
k_s	Roughness height
p	Pressure
u (u_1)	Streamwise velocity component
u_τ	Friction velocity
v (u_2)	Wallnormal velocity component
w (u_3)	Spanwise velocity component
x (x_1)	Streamwise coordinate
y (x_2)	Wallnormal coordinate
z (x_3)	Spanwise coordinate

Greek symbols

δ_s	Stokes layer thickness
δ_ν	Viscous length scale
ν	Molecular kinematic viscosity
ν_t	Turbulent viscosity
τ_{ij}	Subgrid scale stress
τ_w	Wall shear stress
θ	Boundary-layer momentum thickness

Superscripts and subscripts

$(^+)$	Nondimensional quantity normalized using the viscous length scale δ_ν and the friction velocity u_τ
$\overline{()}$	The operation of Reynolds-averaging, or grid-filtering, depending on the context
$<>$	The operation of Reynolds-averaging
$(')$	Denotes a fluctuation from the mean
$\hat{()}$	The operation of test-filtering
$()_{rms}$	Root-mean-square of a variable

Chapter 1

Introduction

Most flows of engineering interest, such as the flow over an aircraft, around a car, etc., occur at high Reynolds numbers and understanding of their physics is crucial for the design of vehicles with high aerodynamic performance. Conducting wind tunnel experiments to study these flows is often expensive and numerical simulations could provide an attractive low-cost alternative. The most reliable computational strategy, Direct Numerical Simulation (DNS) in which all the scales of motion are computed accurately, is currently feasible only for low-Reynolds number flows. Simulations of practical interest have traditionally been in the domain of the Reynolds-Averaged Navier-Stokes Equation (RANS) modelling in which the transport due to the turbulent eddies is entirely modelled. Large-Eddy Simulation (LES) in which only the small eddies are modelled while the large ones are computed accurately, represents a compromise between DNS and RANS. Although LES has been used with great success, in wall-bounded flows, however, LES suffers from similar cost requirements as DNS.

The most common approach used to predict high-Reynolds number flow is based on the Reynolds averaged Navier-stokes(RANS) equations. In the most common formulation, the unknown Reynolds stresses are related to the mean strain rate

through a additional "eddy" viscosity. Various models exist to obtain the eddy viscosity, which are typically calibrated with simple flows such as attached boundary layer, mixing layer etc. Hence these models perform well when used to compute flows that are similar to their calibration flows. In separated flows, however, RANS model do not perform well. The size of the eddies present in the separation region is dependent on the geometry of the flow and these models are not calibrated to account for the geometry- specific scales. Although RANS models are computationally cheap and widely used to predict engineering flows today, their accuracy is limited in practical configurations.

Direct Numerical Simulation (DNS) of the Navier-Stokes equation is the most accurate technique to predict flows. In DNS, all the scales of the motion present in turbulent flows must be resolved accurately. This imposes formidable resolution requirements on the simulation – the grid should be fine enough to resolve the smallest scale motion and the time step used in the simulation should be smaller than the smallest time scale present in the flow. The number of grid points required to resolve all the scales of the motions is proportional to $Re_L^{9/4}$ and the number of time steps required is proportional to $Re_L^{3/4}$. Overall the cost of DNS scales as Re_L^3 (See the review articles of Reynolds [101], and Moin and Mahesh [83]). Because of the high compuational cost required, it will not be feasible to simulate high Reynolds number flows with DNS in the near future.

Large eddy simulation (LES) is a technique that is intermediate between DNS

and RANS in terms of the computational requirement. In LES, only the large scales of the motion which depend on the geometry are fully resolved. The effect of the small scale motions, which are homogeneous and isotropic, is modeled by the eddy viscosity approximation. Although the cost of LES is lower that that of DNS, it is still limited by the computational requirement in the near wall region.

The near wall region of wall bounded flows contains quasi-streamwise and hairpin vortices that are responsible for the high momentum transfer observed near the wall. These vortices result in the generation of streaks that are typically about 2000 wall units (here distance is nondimensionalized with the kinematic viscosity and the friction velocity, $u_\tau = \sqrt{\tau_w/\rho}$, where τ_w is the wall shear stress) in the streamwise direction and 20 to 80 wall units wide in the spanwise direction. To resolve these streaks in the inner layer, the streamwise and spanwise grid spacing has to be of order 100 and 20 wall units, respectively. Chapman [23] estimated that the number of points required to resolve the inner layer is proportional to $Re^{1.8}$. Even though this is less than DNS requirement, simulations that resolve the inner layer for high Reynolds number flows are not feasible with the present day computational resources. Chapman also estimated that the number of points required to resolve the flow in the outer layer is proportional to $Re^{0.4}$.

LES for high Reynolds number flows can be performed only if the wall layer is not resolved and its effect on the outer flow is modeled in a statistical sense. This would make the overall cost of LES proportional to $Re^{0.6}$. Most wall layer models

supply the wall stress to the outer flow, which is applied as the boundary condition at the wall along with zero transpiration velocity through the boundary for the wall-normal component. Four classes of wall layer models can be identified: (i) Models based on equilibrium laws that calculate the wall shear stress using scaling arguments that are valid in equilibrium flows (ii) Models based on a zonal approach that use parabolized boundary layer equations in the inner layer on a grid that is refined along the wall-normal direction to calculate the wall shear stress. (iii) Models based on hybrid RANS/LES approach that use RANS in the inner layer and LES in the outer layer (in principle the latter approach is similar to the zonal one, but with an increased coupling between the flow field in the inner region and the outer region). (iv) Models based on optimal control theory that enforce a set of given conditions (scaling laws etc) to calculate the wall shear stress. Some of the salient features of each of these models are described below. For an in depth review of wall models, the reader is referred to review articles by Cabot and Moin [19], and Piomelli and Balaras [95].

1.1 Equilibrium laws

The earliest wall layer model was introduced by Deardorff [32] in his channel flow calculation. He restricted the second derivatives of the velocity at the first off-wall grid point to be

$$\frac{\partial^2 \bar{u}}{\partial y^2} = -\frac{1}{\kappa Y^2} + \frac{\partial^2 \bar{u}}{\partial z^2} \tag{1.1}$$

$$\frac{\partial^2 \bar{w}}{\partial y^2} = \frac{\partial^2 \bar{w}}{\partial x^2} \tag{1.2}$$

Here, x, y, z are the streamwise, wall normal and spanwise direction respectively and u, v and w are the streamwise, wall-normal and spanwise velocity component respectively. The above equation forced the plane averaged velocity profile to satisfy the logarithmic law in the mean at the first point off the wall (which is at a distance Y from the wall). His results do not compare well with the experimental data, probably due to poor resolution in the outer layer.

Schumann [107] proposed a model in which he correlates the shear stress at the wall to the velocity at the first grid point off the wall by

$$\tau_{xy}(x,z) = \frac{\langle \tau_w \rangle}{\langle \bar{u}(x,Y,z) \rangle} \bar{u}(x,Y,z) \tag{1.3}$$

$$\tau_{yz}(x,z) = \nu \frac{\bar{w}(x,Y,z)}{Y} \tag{1.4}$$

In channel flow, the mean stress $\langle \tau_w \rangle$ is set to the value of the streamwise pressure gradient. Alternatively, it can be calculated by requiring that the plane-averaged velocity at the first grid point off the wall satisfy the logarithmic law [48]. Schumann performed a channel flow calculation with this model and obtained results that matched well with the experimental data.

Piomelli *et al.* [97] obtained better results by slightly modifying Schumann's model. Elongated structures present in the near wall region are usually inclined. To account for this inclination, they related the wall shear stress at a point to the

instantaneous velocity downstream of that point by

$$\tau_{xy}(x,z) = \frac{\langle \tau_w \rangle}{\langle \bar{u}(x,Y,z) \rangle} \bar{u}(x+\Delta_s, Y, z) \tag{1.5}$$

$$\tau_{yz}(x,z) = \nu \frac{\bar{w}(x+\Delta_s, Y, z)}{Y} \tag{1.6}$$

where Δ_s is a streamwise displacement whose value can be obtained from DNS or experimental data.

Marusic *et al.* [76] constructed another variation of Schumann model by matching the spectra of wall shear stress to the spectra of the streamwise velocity. This effectively increases the wall stress fluctuations compared to the Schumann model. This model was tested by Stoll and Porte-Agel [129] in LES of atmospheric boundary layer with surface roughness. The Schumann model and the shifted model of Piomelli *et al.* [97] predicted an incorrect dependence of mean velocity, streamwise Reynolds stresses and spectra of the resolved velocity on the surface roughness whereas the model proposed by Marusic *et al.* [76] did not show this incorrect dependence and gave better results than the other models tested.

The models described above are applicable to simple flows where the logarithmic law is valid so that the mean wall stress can be calculated. Thus, they cannot be applied to complex-geometery flows, in which the logarithmic law may not be satisfied due to wall curvature, pressure gradient or flow separation. These models could be used only if the mean wall shear stress is known *a priori*.

Wu and Squires [141, 139] performed LES of a turbulent flow over a swept and

unswept bump using an approach similar to that of Schumann [107]. They obtained the mean wall shear stress from a separate RANS calculation and used it to correlate the instantaneous wall stress to the instantaneous velocity. They obtained results that matched well with the experimental data. A drawback of their approach is that it assumes that the RANS simulation provides a reasonable prediction of the mean wall shear stress, which is not always true.

1.2 Zonal Approaches

Zonal approaches are based on the assumption that the interaction between the inner layer and the outer layer is weak. The earliest approach of this type is the Two-Layer Model (TLM), proposed by Balaras and Benocci [7]. In the inner layer, this method solves the following boundary-layer equations on a grid that is refined in the wall-normal direction only.

$$\frac{\partial \bar{u}_i}{\partial t} + \frac{\partial \left(\bar{u}_n \bar{u}_i\right)}{\partial x_i} = -\frac{\partial \bar{p}}{\partial x_i} + \frac{\partial \left[\left(\nu + \nu_t\right) \frac{\partial \bar{u}_i}{\partial x_n}\right]}{\partial x_n} \tag{1.7}$$

The subscript n indicates the wall-normal direction and the subscript i takes the value of 1 and 2 when the wall plane is $x-z$ plane. u_n is the normal component of the velocity and is calculated by imposing mass conservation in the inner layer. While integrating the boundary layer equation in the inner layer, the no-slip boundary condition is applied at the wall and the velocity from the outer flow calculation is the effective freestrean velocity at the edge of the inner layer. This method in-

volves solving two additional one-dimensional problems, and hence has a marginally higher cost than the methods based on the equilibrium boundary conditions. Note that inversion of a Poisson equation, which is typically costly, is not needed here. The wall shear stress components obtained by the integration of the above boundary layer equation are used as boundary condition for the outer-flow calculation.

Balaras and Benocci [7] and Balaras *et al.* [8] used an algebraic eddy viscosity model in the inner layer:

$$\nu_t = (\kappa y)^2 D(y) |\bar{S}| \tag{1.8}$$

where κ is the von Kármán constant, y is the distance from the wall, $|\bar{S}|$ is the magnitude of the resolved strain-rate tensor, and $D(y)$ is a damping function needed to obtain the correct beahavior of ν_t at the wall

$$D(y) = 1 - exp\left[-\left(y^+/A^+\right)^3\right] \tag{1.9}$$

Balaras *et al.* [8] computed channel flow at various Reynolds numbers (Re_τ) between 200 and 2000 using the TLM model. They obtained results that are in good agreement with resolved LES, DNS, experiments and the calculation that used equilibrium-based boundary condition. They also employed the TLM model to compute the flow in a square duct and the flow in a rotating channel. In the square duct geometry, the TLM model predicted the secondary flow in corners accurately, which cannot be predicted with the models based on the logarithmic law.

In the rotating channel flow, the models based on the logarithmic law failed due to numerical instability. Results obtained for this flow with the TLM model are in good agreement with the resolved DNS and experiments.

Cabot [18] and Diurno *et al.* [35] performed a calculation of the flow over a backward-facing step for a range of Reynolds numbers using a TLM. They used a variety of models to obtain the inner layer eddy viscosity. The mean velocity and the Reynolds stress profiles were insensitive to the inner layer treatment. The skin friction coefficient was sensitive to the eddy viscosity model used in the inner layer. Two-Layer models cannot be expected to perform well in the flows where the interaction between the inner layer and the outer layer is strong.

1.3 Hybrid RANS/LES models

The first Wall-Modeled LES (WMLES) using the hybrid RANS/LES approach was performed by Nikitin *et al.* [90]. The particular hybrid approach used by Nikitin *et al.*, is based on the Detached-Eddy Simulation (DES) method. The original intended application of DES, as proposed by Spalart *et al.* [127], was massively separated flows. In these applications, the attached boundary layer was modeled using the RANS approach, the separated-flow regions were simulated by LES. When Nikitin *et al.* [90] applied this technique as a wall-model for computing high-Reynolds number turbulent channel flow by allowing the LES region to penetrate into the boundary layer, the skin-friction coefficient was under-predicted by 15% and the

mean velocity showed a shift in the logarithmic law in the LES region. At the interface, between the RANS and LES regions, the resolved eddies are not generated fast enough to balance the decrease in the modeled Reynolds stress. In order to maintain momentum balance, the velocity gradient had to increase in this transition region, forming the so-called "DES buffer layer" [6]. The DES buffer layer has artificially strong streamwise coherent motion and is responsible for the errors in the predicted flow field.

Piomelli *et al.* [96] obtained improved results with WMLES using this approach by including a stochastic forcing term in the transition region. The stochastic forcing generated small-scale fluctuations that acted as "seeds" for the development of realistic, energy-carrying eddies in the LES region. They found that, with the correct amount of forcing, they could successfully remove the shift in the logarithmic law, and improve the prediction of the skin friction coefficient. Although this work showed a promising approach to the solution of the RANS/LES interface problem, the magnitude of the stochastic forcing proposed required *ad hoc* adjustments as the grid or the Reynolds number were changed. A more robust control algorithm to modulate the magnitude of the stochastic force was proposed by Keating and Piomelli [60], and tested in turbulent channel flows. This method adjusts the force magnitude to minimize the extent of the RANS/LES transition region; it resulted in accurate flow prediction with minimal user input in the cases tested.

Various authors, who used other hybrid RANS/LES methods, have observed

the mismatch in the mean velocity at the interface and have also suggested ways to improve the mean velocity prediction. For example, Hamba [49, 50], performed channel flow simulation using various hybrid RANS/LES methods and suggested a method to improve the mean velocity prediction through additional filtering. In the hybrid methods that he used, the filter width in the RANS region is larger than the filter width in the LES region at the RANS/LES interface. To remove this inconsistency, he defined two wall-normal velocity components at the interface; one based on the LES filter width and another based on the RANS filter width. The RANS velocity is obtained from the LES velocity by additional filtering. This method introduces source terms in both continuity and momentum equation and provides forcing at the interface region similar to the forcing used in [96, 60].

Temmerman *et al.* [130] calculated channel flow and a separated flow in a channel constricted by a curved hill using hybrid RANS/LES method. In their hybrid method, the eddy viscosity in the RANS region is defined by $C_\mu k_{mod}^{0.5} l_\mu$, where C_μ is a constant, k_{mod} is the modeled turbulent kinetic energy and l_μ is the length-scale which is either explicitly prescribed or obtained by solving an additional variable such as dissipation. They obtained the constant, C_μ, by equating the RANS eddy viscosity to the LES eddy viscosity at the interface. They were able to remove the shift in the mean velocity, when they used the C_μ value obtained instantaneously at every point rather than using an averaged value along the homogeneous direction. Use of spatially and temporally varying C_μ results in an unsteady forcing of the flow

field in a manner analogous to the stochastic forcing used in [96, 60].

Davidson and Peng [31] calculated channel flow and flow past a hill that has a separation zone using a hybrid RANS/LES method which is based on $k-\omega$ model in the RANS region and a one equation subgrid scale turbulent kinetic energy model of Yoshizawa [142] in the LES region. They also observed the mean velocity mismatch at the interface in the channel flow and obtained better results in the separated flow, which they attributed to the enhanced convective and diffusive transport across the interface in the latter flow. Davidson and Dahlstrom [30] computed channel flow and flow past a asymmetric plane diffuser using a hybrid RANS/LES method based on a one-equation model for turbulent kinetic energy. In their simulation, forcing was provided at the interface by adding a source term to the three momentum equations based on velocity fluctuations taken from a DNS database. With a carefully chosen coefficient for the source term, they were able to remove the mean velocity shift in the channel flow. Davidson and Billson [29] explored using forcing from various types of fluctuations: DNS fluctuations, synthetically generated isotropic and non-isotropic fluctuations and white noise. They conclude that, in terms of the complexity and the quality of the flow field predicted, synthetically generated isotropic fluctuations offered the best results.

1.4 Control-based wall-layer models

Nicoud *et al.* [89] proposed a wall-layer model based on optimal control theory which uses the wall shear stress as a control variable to force the mean velocity in the LES region towards a desired solution (for instance, logarithmic profile). They defined a cost function that measured the deviation of the mean velocity from the logarithmic law of the wall. They used adjoint techniques to calculate the gradient of the cost function with respect to the streamwise and spanwise wall shear stresses. They performed LES of channel flow at $Re_\tau = 4000$ with a coarse mesh. The mean velocity, the wall-normal and the spanwise Reynolds stresses predicted by this model showed better agreement with reference data than by the predicted quantities obtained using either Schumann model with streamwise shift or the TLM model. The streamwise wall shear stress predicted by this model showed poor correlation with the streamwise velocity at the first point off the wall, perhaps, an indication that the strong correlation between the wall shear stress and the streamwise velocity employed by the Schumann model is not a necessary condition. This model increased both production and the dissipation in the near wall region. Although good prediction of the flow field was obtained with this model, the need to solve the adjoint equations at every time step raises the cost of the calculation by 13 times compared to an LES using equilibrium model. Templeton *et al.* [131] proposed a variation of this model that decreased the overall cost of this model to thrice that of the LES using equilibrium laws.

Nicoud *et al.* [89] also proposed another model that used the results from the sub-optimal control simulation (method described above) to estimate the wall-shear stress. They used a linear stochastic estimation to calculate a kernel that when convolved with the fluctuating velocity field gives fluctuating wall shear stress. The kernel was obtained by using the flow field at a $Re_\tau = 4000$ obtained from sub-optimal control simulation. This kernel was found to give results that match the results obtained from sub-optimal control simulation. The same kernel (calibrated at $Re_\tau = 4000$) was found to give better results than equilibrium models for $Re_\tau = 640, 20,000$.

1.5 Plan of the present dissertation

While WMLES based on DES methodology has been extensively tested in equilibrium channel flows and various strategies to improve its performance has been proposed, so far, its performance in non-equilibrium flows, where perturbations due to additional imposed strains could cause a change in the eddy generation mechanism at the RANS/LES interface and affect the accuracy of the predicted flow field, has not been tested. WMLES, due to its decreased computational cost requirement, has the potential to be used as a predictive tool, however, most engineering applications are computed using RANS, often with commercial codes. Another objective of this work is to compare the performance of several RANS turbulence models to that of WMLES. The geometry of the flows examined was chosen based on the following

considerations: the geometry had to be simple, so that high-quality grids could easily be generated, and numerical errors could be controlled; the configuration had to be characterized by the presence of challenging non-equilibrium phenomena; high-quality experimental data had to be available to allow comparison between the numerical techniques. Four representative cases are examined: a flow with a mild separation, a flow subjected to multiple perturbations through pressure-gradient and curvature changes, a three-dimensional flow that includes streamwise curvature and spanwise pressure gradients and an oscillating flow.

First, we examine the flow on a contoured ramp, which was studied experimentally by Song and Eaton [124]. This flow is characterized by a shallow separation region due to an adverse pressure gradient; it is very important to predict accurately the mean velocity profile upstream of separation, since incorrect prediction of the separation point may result in significant errors in the development of the flow downstream and in the recovery region.

Second, we perform calculations of the flow past a two-dimensional bump, which was studied experimentally by DeGraaff [33] and Webster *et al.* [137]. Wu and Squires [140, 139] carried out LES of this flow at a lower Reynolds number than the one used in this study. This flow is subjected to extra strain rates by the wall curvature and streamwise pressure gradient. It is also subjected to sudden perturbations through the change in wall curvature: to give accurate results a model must be able to predict the correct response to perturbations.

Third, we perform calculations of the flow past a three-dimensional bump, which was studied experimentally by DeGraaff [33] and Webster *et al.* [138]. Wu and Squires [141] also simulated this flow at a lower Reynolds number than the one used in this study. This flow experiences a spanwise pressure gradient, in addition to same strain rates and the sudden perturbations that the two-dimensional bump experiences. Because of the addition of the spanwise pressure gradient, the initially two-dimensional turbulent boundary layer becomes three-dimensional and relaxes back to its two-dimensional state only behind the bump, after the removal of the spanwise pressure gradient. In three-dimensional turbulent boundary layers, all six Reynolds stresses are non-zero and the direction of shear-stress vector $(\tan^{-1}\langle v'w'\rangle/\langle u'v'\rangle)$ does not coincide with the direction of the velocity-gradient vector $(\tan^{-1}\langle \partial w/\partial y\rangle/\langle \partial u/\partial y\rangle)$, where $\langle v'w'\rangle, \langle u'v'\rangle$ are the resolved shear stresses, $\langle \partial w/\partial y\rangle, \langle \partial u/\partial y\rangle$ are the wall-normal derivatives of the mean spanwise and horizontal velocities and $\langle\rangle$ refers the Reynolds-averaged quantities. This poses a significant challenge to isotropic eddy viscosity models which cannot account for the lack of alignment in the direction between the shear-stress vector and the velocity gradient vector. This problem has additional complexities compared to the two-dimensional bump problem and is a good candidate to test the performance of WMLES for three-dimensional flows.

The fourth test case chosen is the turbulent oscillating boundary layer on a flat plate. Despite the simple configuration chosen, the flow is characterized by strong

non-equilibrium effects and is in accordance with the objective of this dissertation. The flow evolution over the time period is dictated by favorable and adverse pressure gradient effects and the turbulent transport mechanism is significantly altered compared to a steady boundary layer. The flow development is dictated by the turbulence transport mechanism near the wall which poses a significant challenge to WMLES since it does not resolve this mechanism in the near wall region. Numerical results are compared to the measured values from Jensen *et al.* [55] experiments.

In the following chapter, we will discuss the numerical approach and the models used. We will then present the problem formulation and discuss the results for each of the four flows studied. Finally, we will make some concluding remarks.

1.6 Accomplishments

The following list summarizes the important contributions of this work:

- Performed extensive modification of an in-house finite volume Navier-Stokes solver including implementation of new boundary conditions, development of a parallel version of poisson solver that solves a series of two-dimensional Helmholtz equations obtained by applying Fast Fourier Transform to the poisson equation, implementation of Scale-Dependent Lagrangian Dynamic Eddy Viscosity subgrid scale model.

- Demonstrated inapplicability of log-law boundary condition, a widely used wall-model, to flows that have shallow separation.

- Demonstrated the importance of generation of resolved eddies at the RANS/LES interface in LES that use RANS as a wall-model for the accuracy of the predicted flow field.

- Demonstrated the improvement in the predicted flow field when stochastic forcing is applied at the RANS/LES interface to accelerate the generation of resolved eddies.

- Demonstrated that high Reynolds flow of geophysical interest can be simulated accurately by an appropriate choice of wall models and SGS models.

Chapter 2

Governing Equations and Numerical Methods

This chapter presents the governing equations, the various models used and the numerical technique employed for the discretization of the governing equations. In this work, the large-eddy simulations were performed with the Smagorinsky, the Lagrangian, the Scale-Dependent Lagrangian and the Wall-Modeled Large-eddy Simulation (WMLES) version of the Spalart-Allmaras model. RANS computations were performed with the $k-\epsilon$, the Shear stress transport (SST), the Reynolds stress transport model (RSTM) and the RANS version of the Spalart-Allmaras model.

2.1 Large Eddy Simulations

In large-eddy simulations, the governing equations are obtained by applying a low pass filter to the Navier-Stokes equations [69]. When the filtering is done implicitly through the grid resolution and the discretization error, it attenuates the amplitude of all the modes whose wavenumber is larger than the grid spacing. In case of explicit filtering, it attenuates all the modes whose wavenumber is larger than the filter width (often a function of the grid spacing). The following integral

relation describes the filtering operation with a kernel $G(\mathbf{x}, \mathbf{x}')$ on the function $f(\mathbf{x})$:

$$\overline{f}(\mathbf{x}) = \int \mathbf{G}(\mathbf{x}, \mathbf{x}')\mathbf{f}(\mathbf{x}')\mathbf{d}\mathbf{x}' \tag{2.1}$$

Using the above filtering operation, f can be decomposed into a large scale resolved component, $\overline{f}$, and a subgrid scale unresolved component, f' such that

$$f(\mathbf{x}) = \overline{\mathbf{f}}(\mathbf{x}) + \mathbf{f}'(\mathbf{x}) \tag{2.2}$$

Appling the filter to the Navier-Stokes equations yields

$$\frac{\partial}{\partial t}\overline{u}_i + \frac{\partial}{\partial x_j}\overline{u}_i\,\overline{u}_j = -\frac{1}{\rho}\frac{\partial}{\partial x_i}\overline{p} + \nu\frac{\partial^2}{\partial x_j \partial x_j}\overline{u}_i - \frac{\partial}{\partial x_j}\tau_{ij} \tag{2.3}$$

$$\frac{\partial}{\partial x_i}\overline{u}_i = 0, \tag{2.4}$$

where

$$\tau_{ij} = \overline{u_i u_j} - \overline{u}_i\,\overline{u}_i \tag{2.5}$$

is the subgrid scale stress tensor. The filtering operation has introduced the subgrid scale stress tensor, which accounts for the effect of filtered high frequency component or the small scale motion on the resolved large scale motion. To solve the filtered governing equations (2.3) and (2.4), the subgrid scale stress tensor must be modeled in terms of the filtered quantities denoted by $\overline{u}_i$. In the following section, various approaches commonly used to model the subgrid scale tensor is discussed.

2.1.1 Subgrid scale modeling

The most widely used model to calculate the subgrid scale tensor is based on Boussinesq [14] eddy viscosity assumption in which the subgrid scale stress tensor is assumed to depend on the resolved strain rate tensor ($\overline{S}_{ij}$) by the following relation

$$\tau_{ij} - \frac{1}{3}\tau_{kk}\delta_{ij} = -2\nu_t \overline{S}_{ij} \tag{2.6}$$

$$\overline{S}_{ij} = \frac{1}{2}\left(\frac{\partial \overline{u}_i}{\partial x_j} + \frac{\partial \overline{u}_j}{\partial x_i}\right) \tag{2.7}$$

where ν_t is the eddy viscosity and is an unknown. Various models widely used to calculate the eddy viscosity are described in the following sections.

2.1.2 Smagorinsky model

Smagorinsky [116] derived the following expression for the eddy viscosity by assuming that the energy production equals the energy dissipation.

$$\nu_t = (C_s\Delta)^2 \left|\overline{S}\right| \tag{2.8}$$

where

$$|\overline{S}| = \left(2\overline{S}_{ij}\overline{S}_{ij}\right)^{\frac{1}{2}} \tag{2.9}$$

and Δ is the filter width associated with the kernel function $\overline{G}(\mathbf{x}, \mathbf{x}')$ in Eq. (2.1) and C_s is the Smagorinsky constant. Assuming that the filter cutoff is in the inertial subrange where the energy spectrum obeys Kolmogorov law [63], (*i.e.*, $E(k) =$

$C_K \epsilon^{\frac{2}{5}} k^{\frac{-2}{3}}$), Lilly [70] calculated the value of the Smagorinsky constant as 0.17. However, Deardorff [32] in his calculation of turbulent channel flow found that this value of C_s causes excessive damping of turbulent fluctuations and used a decreased value of 0.1. In wall-bounded flows, the above expression for the eddy viscosity overpredicts the subgrid scale stresses in the near wall region. Moin and Kim [82] used Van Driest [133] wall-functions to damp the eddy viscosity in the near wall region. With this modification, the eddy viscosity takes the following form,

$$\nu_t = (C_s \Delta)^2 \left(1 - \exp(\frac{y^+}{A^+})\right)^2 \left|\overline{S}\right| \tag{2.10}$$

where $A^+ = 25$. In the case of transitional flows, Piomelli *et al.* [98] report that the Smagorinsky model is excessively dissipative which results in delayed transition and poor agreement with DNS results. Based on the difference in the value of the shape factor for turbulent ($H_t = 1.7$) and laminar ($H_l = 2.5$) regime, they propose the following modification to the eddy viscosity expression.

$$\nu_t = (C_s \Delta)^2 \left(\frac{H_l - H}{H_l - H_t}\right)^2 \left|\overline{S}\right| \tag{2.11}$$

With the above modification, they obtained better agreement with the DNS results.

2.1.3 Dynamic model

From the discussion in the preceding section, it is clear that often *ad hoc* modifications are needed to obtain accurate flow prediction with the Smagorinsky model. This difficulty was overcame with the introduction of Germano identity [43]

which was used by Germano *et al.* [44] to determine dynamically the eddy viscosity using the resolved quantities. In the dynamic modeling procedure, the Navier-Stokes equations are filtered again with a second filter known as 'test filter' whose filter width $\widehat{\Delta}$ is larger than the original grid filter. The LES equations filtered with the test filter can be written as follows

$$\frac{\partial}{\partial t}\widehat{\overline{u}}_i + \frac{\partial}{\partial x_j}\widehat{\overline{u}}_i\,\widehat{\overline{u}}_j = -\frac{1}{\rho}\frac{\partial}{\partial x_i}\widehat{\overline{p}} + \nu\frac{\partial^2}{\partial x_j \partial x_j}\widehat{\overline{u}}_i - \frac{\partial}{\partial x_j}T_{ij} \tag{2.12}$$

where the 'subtest scale' stress tensor for the above equation is

$$T_{ij} = \widehat{\overline{u_i u_j}} - \widehat{\overline{u}}_i\widehat{\overline{u}}_j \tag{2.13}$$

and the resolved stress tensor is

$$L_{ij} = \widehat{\overline{u}_i\overline{u}_j} - \widehat{\overline{u}}_i\widehat{\overline{u}}_j \tag{2.14}$$

The subgrid scale stress tensor for the LES equation is

$$\tau_{ij} = \overline{u_i u_j} - \overline{u}_i\overline{u}_j \tag{2.15}$$

Germano's identity relates the above three stresses through the following expression

$$L_{ij} = T_{ij} - \widehat{\tau}_{ij} \tag{2.16}$$

Assuming that T_{ij} and τ_{ij} have the same form as they do in the Smagorinsky eddy viscosity model, they may be written as

$$\tau_{ij} - \frac{1}{3}\delta_{ij}\tau_{kk} = -2C_s\overline{\Delta}^2\left|\overline{S}\right|\overline{S}_{ij} \tag{2.17}$$

and

$$T_{ij} - \frac{1}{3}\delta_{ij}T_{kk} = -2C_s\widehat{\overline{\Delta}}^2\widehat{|S|}\,\widehat{\overline{S}}_{ij} \tag{2.18}$$

where $\overline{S}_{ij}$ and $\widehat{\overline{S}}_{ij}$ are the rate of strain tensors associated with the grid-filter (Δ) and test-filter ($\widehat{\Delta}$) respectively. Using Eq. (2.14), (2.17) and (2.18), we have

$$L_{ij} - \frac{1}{3}\delta_{ij}L_{kk} = 2C_sM_{ij} \tag{2.19}$$

where

$$M_{ij} = \widehat{\overline{\Delta}}^2\widehat{|S|}\,\widehat{\overline{S}}_{ij} - \overline{\Delta}^2\widehat{\left|\overline{S}\right|\overline{S}}_{ij} \tag{2.20}$$

L_{ij} can be calculated from the resolved quantities using Eq. (2.14). Originally Germano *et al.* [44] calculated C_s by contracting both sides of the Eq. (2.19) with the strain rate tensor S_{ij}. This procedure lead to numerical difficulties as the contraction of M_{ij} and S_{ij} sometime yields small number which results in a large eddy viscosity. To avoid this, Germano *et al.* averaged the left and right hand side of Eq. (2.19) over the homogeneous direction after contracting them with S_{ij}.

Lilly [71] proposed a method of evaluating C_s using least square minimization. Lilly observed that L_{ij} being a symmetric trace free matrix has five independent elements which gives us five equations for a single unknown C_s. He derived an expression for C_s by minimizing the difference between the right and left hand side of Eq. (2.19) in a least square sense. His method reduces to contracting Eq. (2.19) with M_{ij} on both sides.

In wall-bounded flows, the dynamic model predicts lower C_s without having to use *ad hoc* wall functions. It predicts a lower C_s in shear flows compared to isotropic

flows as expected. Although it shows significant improvement over the Smagorinsky model, its implementation is fraught with numerical issues. It predicts both positive and negative eddy viscosity with a large range. The rapid variation of eddy viscosity over the flow field causes the numerical schemes to become unstable. A remedy, that is often used to alleviate some of the numerical difficulties, is to average along homogeneous directions. For example in channel flow, averaging is performed along the horizontal planes and in spatially varying two-dimensional problems, averaging is performed along the spanwise direction. Also negative eddy viscosity is clipped so that the total viscosity is non-negative.

2.1.4 Lagrangian Dynamic model

In many problems in complex geometries, there is a lack of statistical homogeneity along any direction which poses difficulty in performing the averaging operation in dynamic models. Meneveau *et al.* [79] proposed averaging along the fluid pathline which extended the application of dynamic models for inhomogeneous problems. This model uses Lilly's [71] approach of least square minimization of the error to calculate the model coefficient. Unlike the original dynamic model where the error is calculated instantaneously at every point, in this model, the error is calculated as the total error accumulated by a particle along its pathline.

Performing least square minimization of the total error with respect to the model coefficient (C_s^2) yields

$$C_s^2(\mathbf{x},t) = \frac{I_{LM}}{I_{MM}} \tag{2.21}$$

where

$$I_{LM} = \int_{-\infty}^{t} L_{ij}(\mathbf{z}(t'),t')M_{ij}(\mathbf{z}(t'),t')W(t-t')dt' \tag{2.22}$$

$$I_{MM} = \int_{-\infty}^{t} M_{ij}(\mathbf{z}(t'),t')M_{ij}(\mathbf{z}(t'),t')W(t-t')dt' \tag{2.23}$$

where the function $W(t-t')$ is used to increase the weight of current events compared to the past ones.

$$W(t-t') = \frac{e^{-(t-t')/T}}{T} \tag{2.24}$$

Meneveau *et al.* [79] chose the above weight function so that I_{LM} and I_{MM} can be evaluated as the solution to the following transport equations.

$$\frac{DI_{LM}}{Dt} = \frac{\partial I_{LM}}{\partial t} + \overline{\mathbf{u}} \cdot \nabla I_{LM} = \frac{1}{T}(L_{ij}M_{ij} - I_{LM}) \tag{2.25}$$

$$\frac{DI_{MM}}{Dt} = \frac{\partial I_{MM}}{\partial t} + \overline{\mathbf{u}} \cdot \nabla I_{MM} = \frac{1}{T}(M_{ij}M_{ij} - I_{MM}) \tag{2.26}$$

The free parameter T in this model controls the extent of the Lagrangian averaging in time; Meneveau *et al.* suggest the following expression based on the consideration that T should be large enough to attenuate the noise in the coefficient.

$$T = 1.5\Delta(I_{LM}I_{MM})^{-\frac{1}{8}} \tag{2.27}$$

Instead of solving the two transport equations (Eq. 2.25 and 2.26), which is computationally expensive, they suggest transforming the total derivative term to

a Lagrangian framework in which it can be cast as a temporal derivative term evaluated along the pathline. The finite difference approximation of the two transport equation is given by the following expression

$$I_{LM}^{n+1}(\mathbf{x}) = H\ \left\{\varepsilon\, L_{ij}^{n}(\mathbf{x})\, M_{ij}^{n}(\mathbf{x})\ + (1-\varepsilon)\, I_{LM}^{n}(\mathbf{x} - \overline{\mathbf{u}}^{n}\Delta t)\right\} \tag{2.28}$$

$$I_{MM}^{n+1}(\mathbf{x}) = \varepsilon\, M_{ij}^{n}(\mathbf{x})\, M_{ij}^{n}(\mathbf{x})\ + (1-\varepsilon)\, I_{MM}^{n}(\mathbf{x} - \overline{\mathbf{u}}^{n}\Delta t) \tag{2.29}$$

$$\varepsilon = \frac{\Delta t/T^{n}}{1 + \Delta t/T^{n}} \tag{2.30}$$

where $H\{x\}$ is the ramp function

$$H\{\mathbf{x}\} \;=\; x \quad \text{if} \quad x \geq 0\,, \tag{2.31}$$

$$\;=\; 10^{-32} \quad \text{otherwise} \tag{2.32}$$

Quantities at the upstream location $(\mathbf{x} - \overline{\mathbf{u}}^{n}\Delta)$ are evaluated using a trilinear interpolation.

2.1.5 Scale-Dependent Lagrangian Dynamic model

One of the key assumptions in dynamic models is that both grid-filter and the test-filter are in the inertial range so that the model coefficient used in the sub-grid scale stresses (2.17) and sub-test scale stresses (2.18) can be assumed to be the same because of their scale-invariance in the inertial range. This assumption is violated under two-scenarios; in the first scenario, the grid might be fine enough to resolve the dissipation range and in the second scenario, the grid might be so coarse that

either the test-filter or both grid-filter and the test-filter lie in the integral scale. In the former case, Meneveau and Lund [78] show that, based on *a priori* analysis, the model coefficient sharply increases as the dissipation range is approached. They also show that the model coefficient predicted by the dynamic model corresponds to the test-filter width rather than the grid-filter width. The second scenario poses problem in the context of wall-modelled LES, where the grid is not fine enough to resolve even the inertial range in the near wall region. For the second scenario, Porté-Agel *et al.* [99] show that dynamic models are under-dissipative in the near-wall region which results in the over-prediction of wall-normal fluctuations. To overcome this issue, they propose a Scale-Dependent dynamic model where the assumption that the model coefficient is independent of the filter width is relaxed. Bou-Zeid *et al.* [13] modified this model to reduce its computational cost when this model is applied with Lagrangian averaging. The Scale-Dependent dynamic model [13, 99] introduces another test-filter ($\widetilde{\Delta}$) which is four times as wide as the grid-spacing. Using Germano's identity,

$$Q_{ij} - \frac{1}{3}\delta_{ij}Q_{kk} = C_{s4\Delta}^2 N_{ij} \tag{2.33}$$

where Q_{ij} is the modeled subtest stresses at this test-filter width

$$Q_{ij} = \widetilde{\overline{u_i u_j}} - \widetilde{\overline{u}}_i \widetilde{\overline{u}}_j \tag{2.34}$$

$$N_{ij} = \overline{\Delta}^2 \widetilde{\left|\overline{S}\right| \overline{S}}_{ij} - \widetilde{\overline{\Delta}}^2 \widetilde{\left|\overline{S}\right|} \widetilde{\overline{S}}_{ij} \tag{2.35}$$

Note that the dependence of the model coefficient on the test-filter in the Eq. (2.33). Lilly's least square minimization yields

$$C^2_{s4\Delta}(\mathbf{x},t) = \frac{I_{QN}}{I_{NN}} \tag{2.36}$$

where

$$I_{QN} = \int_{-\infty}^{t} Q_{ij}(\mathbf{z}(t'),t') N_{ij}(\mathbf{z}(t'),t') W(t-t') dt' \tag{2.37}$$

$$I_{NN} = \int_{-\infty}^{t} N_{ij}(\mathbf{z}(t'),t') N_{ij}(\mathbf{z}(t'),t') W(t-t') dt' \tag{2.38}$$

where the weighting function is

$$W(t-t') = \frac{e^{-(t-t')/T_{4\Delta}}}{T_{4\Delta}} \tag{2.39}$$

with the parameter $T_{4\Delta}$ defined by

$$T_{4\Delta} = 1.5\Delta (I_{QN} I_{NN})^{-\frac{1}{8}} \tag{2.40}$$

Bou-Zeid *et al.* [13] evaluate I_{QN} and I_{NN} based on the approach used in the Lagrangian dynamic model, *i.e.,* approximation along the pathline.

$$I^{n+1}_{QN}(\mathbf{x}) = H\ \left\{ \varepsilon_{4\Delta}\, Q^n_{ij}(\mathbf{x})\, N^n_{ij}(\mathbf{x}) + (1-\varepsilon_{4\Delta})\, I^n_{QN}(\mathbf{x} - \overline{\mathbf{u}}^n \Delta t) \right\} \tag{2.41}$$

$$I^{n+1}_{NN}(\mathbf{x}) = \varepsilon_{4\Delta}\, N^n_{ij}(\mathbf{x})\, N^n_{ij}(\mathbf{x}) + (1-\varepsilon_{4\Delta})\, I^n_{NN}(\mathbf{x} - \overline{\mathbf{u}}^n \Delta t) \tag{2.42}$$

where

$$\varepsilon_{4\Delta} = \frac{\Delta t / T^n_{4\Delta}}{1 + \Delta t / T^n_{4\Delta}} \tag{2.43}$$

With this approach, the dynamic model is applied at two filter-widths and the corresponding model coefficients ($C^2_{s2\Delta}$ and $C^2_{s4\Delta}$) are obtained. Porté-Agel *et al.* [99] assume that the ratio of the model coefficients is scale invariant, where the ratio is defined as

$$\beta = \frac{C^2_{s4\Delta}}{C^2_{s2\Delta}} \tag{2.44}$$

With the scale invariance assumption for β, we can also write β as $C^2_{s2\Delta}/C^2_{s\Delta}$. First, β is evaluated using Eq. 2.44 and then the following equation is used to calculate the model coefficient at the grid scale.

$$C^2_{s\Delta} = \frac{C^2_{s2\Delta}}{\beta} \tag{2.45}$$

Bou-zeid *et al.* [13] suggest clipping β to 0.125 if it is less than 0.125, to avoid the numerical instabilities that would otherwise arise because of local high value of eddy viscosity.

2.1.6 WMLES based on Spalart-Allmaras model

The Spalart-Allmaras (SA) turbulence model [125] solves a transport equation for an auxiliary variable, $\widetilde{\nu}$. It was originally proposed as a RANS model for external aerodynamic applications by Spalart and Allmaras who calibrated it with canonical flows such as mixing layer, wakes and flat-plate boundary layer. The SA model solves a transport equation for an auxiliary variable, $\widetilde{\nu}$:

$$\frac{D\widetilde{\nu}}{Dt} = c_{b1}\widetilde{S}\widetilde{\nu} - c_{w1}f_w\left[\frac{\widetilde{\nu}}{\widetilde{d}}\right]^2 + \frac{1}{\sigma}\left\{\nabla\cdot[(\nu+\widetilde{\nu})\nabla\widetilde{\nu}] + c_{b2}\left(\nabla\widetilde{\nu}\right)^2\right\}; \tag{2.46}$$

where $\nu_t = \widetilde{\nu} f_{v1}$ and

$$f_{v1} = \frac{\chi^3}{\chi^3 + c_{v1}^3}, \qquad \chi = \frac{\widetilde{\nu}}{\nu}, \qquad \widetilde{S} = |\Omega| + \frac{\widetilde{\nu}}{\kappa^2\widetilde{d}^2}f_{v2}, \qquad f_{v2} = 1 - \frac{\chi}{1+\chi f_{v1}}. \tag{2.47}$$

Here $|\Omega|$ is the magnitude of the vorticity, and the function f_w is given by

$$f_w = g\left[\frac{1+c_{w3}^6}{g^6+c_{w3}^6}\right]^{1/6}, \qquad g = r + c_{w2}(r^6 - r), \qquad r = \frac{\widetilde{\nu}}{\widetilde{S}k^2\widetilde{d}^2}. \tag{2.48}$$

The constants in the model are $c_{b1} = 0.1355$, $\sigma = 2/3$, $c_{b2} = 0.622$, $\kappa = 0.41$, $c_{w1} = c_{b1}/\kappa^2 + (1+c_{b2})/\sigma$, $c_{w2} = 0.3$, $c_{w3} = 2.0$ and $c_{v1} = 7.1$. In the RANS version of the model, the length-scale in the destruction term, $\widetilde{d}$, is equal to the distance from the wall, y_w.

In the Wall-Modeled LES (WMLES) version of the model [90] the length-scale, $\widetilde{d}$, is chosen as the minimum of the RANS and LES length scales:

$$\widetilde{d} = \min(y_w, C_{\mathrm{DES}}\Delta) \tag{2.49}$$

where y_w is the distance from the wall, $C_{\mathrm{DES}} = 0.65$ and $\Delta = \max(\Delta x, \Delta y, \Delta z)$. This model functions in RANS mode in the inner region and switches to LES mode in the outer region. The location where the switch takes place, $y_w = C_{\mathrm{DES}}\Delta$, is denoted here as y_{switch}.

2.1.7 Stochastic forcing for WMLES

In WMLES calculations that use an hybrid RANS/LES approach, a region is present in which the flow transitions from a quasi-steady RANS near-wall flow to the unsteady LES outer flow. For $y > y_{\text{switch}}$ the eddy-viscosity is decreased compared to the RANS value; the resolved stresses are, however, insufficient to maintain the momentum balance, since no turbulent eddies exist in the smooth RANS region. Immediately above the nominal interface ($y > y_{\text{switch}}$), then, the modeled stress is larger than the resolved one, despite the fact that the calculation is supposedly in LES mode, and most of the stress should be supported by the resolved eddies.

Piomelli *et al.* [96] added a stochastic force f_i to the Navier-Stokes equations to generate small-scale fluctuations in the transition region, and facilitate the development of turbulent eddies capable of supporting the Reynolds shear stresses there. The forcing was given by a normally distributed random series with zero mean, with length-scale equal to the filter width, time-scale equal to the time step (under the assumption that the most important of the modeled eddies are the largest ones), and was enveloped using various *ad hoc* functions that constrained f_i to be active only in the transition region. The amplitude of the envelope (and, therefore, the variance of the force) was assigned by trial-and-error to match the logarithmic mean-velocity profile.

In this work we also use stochastic forcing to stimulate the eddy generation in the transition region. To calculate the variance of the force σ^2, however, we use

the dynamic control technique proposed by Keating and Piomelli [60]. This method modulates f_i to make the location where the resolved stress becomes larger than the modeled one coincide with the nominal interface, at least in an average sense.

Keating and Piomelli [60] define a transition region (between y_{switch} and the location y_ν of maximum ν_t) over which they expect the average resolved and modeled shear stresses to be equal, and modulate the stochastic force to achieve this result. The difference between the resolved and modeled Reynolds shear stress integrated over the transition region is first calculated:

$$\epsilon = \int_{y_{\text{switch}}}^{y_\nu} \left(\nu_t \frac{d\langle \overline{u_s} \rangle}{dy} + \langle u_s' v_n' \rangle \right) dy. \tag{2.50}$$

Here, the angle brackets $\langle \cdot \rangle$ denote time- and spanwise-averaged quantities, while the prime denotes the large-scale part of the fluctuation: $f' = \overline{f} - \langle \overline{f} \rangle$. Also, u_s and v_n denote the streamwise and wall-normal components of the velocity. Then a proportional controller is used to calculate the variance of the force:

$$\sigma_{n+1}(x) = \sigma_n(x) + A\epsilon(x + L), \tag{2.51}$$

with $A = 10$. Time and spanwise averaging is required in the evaluation of the resolved and modeled shear stress terms in (2.50). In spatially developing flows the stochastic forcing applied at a location affects the error at a downstream location, due to the mean advection. Hence, a streamwise shift L, of the order of the integral length-scale, is used in the controller following [60] (we use $L = \delta_{ref}$ in this work). The force is enveloped using a top-hat function centered on the location of maximum

turbulent eddy-viscosity, whose width is twice the distance between y_ν and y_{switch}. The reader is referred to Keating and Piomelli [60] for a detailed discussion of the model implementation.

This procedure had to be slightly modified when applied in complex geometries. In regions of convex curvature, the resolved shear stress decreases, whereas the modeled shear stress increases compared to their upstream values. Because of the increase in the difference between the resolved and the modeled shear stress, the amplitude predicted by the controller increases unboundedly, making the calculation unstable. Therefore, we allowed the dynamic controller to be active in the flat region and the concave regions of the flow only.

For the three-dimensional flow studied, the difference between the resolved and the modeled Reynolds shear stress is calculated as follows:

$$\epsilon = \int_{y_{\text{switch}}}^{y_\nu} \left(-\nu_t \sqrt{\left[\left(\frac{d\langle \overline{u_s} \rangle}{dy} \right)^2 + \left(\frac{d\langle \overline{w} \rangle}{dy} \right)^2 \right]} - \sqrt{\left[\left(\langle u_s' v_n' \rangle \right)^2 + \left(\langle w' v_n' \rangle \right)^2 \right]} \right) dy \tag{2.52}$$

Here u_s denotes the projection of the streamwise component of the velocity in $x-y$ plane, v_n denotes the wall-normal and w denotes the spanwise component of the velocity. Note that for two-dimensional flows Eq. (2.52) reduces to (2.50).

2.2 Mathematical model for RANS

Ensemble averaging of the Navier-Stokes equations yields Reynolds-averaged Navier-Stokes equations with the unknown Reynolds stresses. The RANS equa-

tions take the same form as LES equations with the velocity components and the pressure field now representing the mean quantities that do not have any spatial variation along homogeneous direction and have no temporal variation if the flow is statistically stationary. Reynolds stresses are usually closed with the eddy viscosity assumption and the unknown eddy viscosity is computed from models that typically involve solving for a velocity scale and a time scale which are then used to construct the eddy viscosity.

2.2.1 $k - \epsilon$ model

The $k - \epsilon$ model is the most widely used turbulence model in engineering applications. It solves the turbulence kinetic energy, k, and its dissipation rate, ϵ, to model the eddy viscosity. The standard $k - \epsilon$ model used here was proposed by Jones and Launder [58] and the empirical constants used in the model were given by Launder and Sharma [67]. The standard $k - \epsilon$ model predicts an high eddy viscosity in the near wall region, a consequence of using k as the velocity scale in the near wall region instead of v_{rms} which better represents the damping of the turbulence in the near wall region. To overcome this difficulty, one of the following approaches is used in the near-wall region. In the simplest treatment, the near-wall region is entirely bypassed by using wall functions. Another approach is to use damping functions to reduce the eddy viscosity in the near wall region. The third approach which is used here is based on a two layer treatment in which the $k - \epsilon$ equation is used only in

the outer region and a different eddy viscosity model is used in the near-wall region.

The transport equations for the $k-\epsilon$ model are

$$\frac{Dk}{Dt} = \frac{\partial}{\partial x_j}\left[\left(\nu + \frac{\nu_t}{\sigma_k}\right)\frac{\partial k}{\partial x_j}\right] - \overline{u_i' u_j'}\frac{\partial u_i}{\partial x_j} - \epsilon \tag{2.53}$$

$$\frac{D\epsilon}{Dt} = \frac{\partial}{\partial x_j}\left[\left(\nu + \frac{\nu_t}{\sigma_\epsilon}\right)\frac{\partial \epsilon}{\partial x_j}\right] - C_{1\epsilon}\frac{\epsilon}{k}\overline{u_i' u_j'}\frac{\partial u_i}{\partial x_j} - C_{2\epsilon}\frac{\epsilon^2}{k} \tag{2.54}$$

$$\nu_{t,outer} = C_\mu k^2/\epsilon \tag{2.55}$$

The constants in the above equations are $\sigma_k = 1.0$, $\sigma_\epsilon = 1.3$, $C_{1\epsilon} = 1.44$, $C_{2\epsilon} = 1.92$ and $C_\mu = 0.09$.

In the inner-layer, the eddy viscosity is computed using the model proposed by Chen and Patel [24]. It solves the transport equation for k but uses an algebraic formula for ϵ.

$$\epsilon = \frac{k^{\frac{3}{2}}}{\ell_\mu} \tag{2.56}$$

where the length scale, ℓ_μ is computed from

$$\ell_\mu = y c_\ell \left(1 - e^{-\mathrm{Re}_y/A_\mu}\right), \qquad Re_y = \frac{y\sqrt{k}}{\nu} \tag{2.57}$$

where y is the distance to the nearest wall. The eddy viscosity in the near-wall region is computed using

$$\nu_{t,inner} = C_\mu \ell_\mu \sqrt{k} \tag{2.58}$$

The eddy viscosity is obtained by combining the inner-layer eddy viscosity with the outer layer one through a blending function, λ_ϵ, which is equal to unity far from the wall and zero very near the wall.

$$\nu_t = \lambda_\epsilon \nu_{t,outer} + (1 - \lambda_\epsilon)\nu_{t,inner} \tag{2.59}$$

The constants in the length scale formula are $c_\ell = \kappa C_\mu^{-3/4}$ and $A_\mu = 70$.

2.2.2 Shear Stress Transport (SST) model

The Shear Stress Transport (SST) model, proposed by Menter [80], is obtained by blending the $k-\epsilon$ and $k-\omega$ model, with the $k-\omega$ model active in the near-wall region and the $k-\epsilon$ model in the freestream. It was designed to take the advantages of the $k-\omega$ model over the $k-\epsilon$ model in the near-wall region and to avoid the sensitivity of the $k-\omega$ model to the boundary conditions in the freestream. The transport equation for k and ω are given below

$$\frac{Dk}{Dt} = \frac{\partial}{\partial x_j}\left[\left(\nu + \frac{\nu_t}{\sigma_k}\right)\frac{\partial k}{\partial x_j}\right] - \overline{u_i' u_j'}\frac{\partial u_i}{\partial x_j} - \beta^* k\omega \tag{2.60}$$

$$\begin{aligned}\frac{D\omega}{Dt} = \; & \frac{\partial}{\partial x_j}\left[\left(\nu + \frac{\nu_t}{\sigma_\omega}\right)\frac{\partial \omega}{\partial x_j}\right] - \alpha\frac{1}{\nu_t}\overline{u_i' u_j'}\frac{\partial u_i}{\partial x_j} \\ & -\beta\omega^2 + 2\left(1-F_1\right)\sigma_{\omega 2}\frac{1}{\omega}\frac{\partial k}{\partial x_j}\frac{\partial \omega}{\partial x_j}\end{aligned} \tag{2.61}$$

The blending function F_1 used to blend the $k-\epsilon$ and $k-\omega$ model is given by

$$F_1 = \tanh\left(\Phi_1^4\right) \tag{2.62}$$

$$\Phi_1 = \min\left[\max\left(\frac{\sqrt{k}}{0.09\omega y}, \frac{500\mu}{\rho y^2 \omega}\right), \frac{4\rho k}{\sigma_{\omega,2} D_\omega^+ y^2}\right] \tag{2.63}$$

$$D_\omega^+ = \max\left[2\rho\frac{1}{\sigma_{\omega,2}}\frac{1}{\omega}\frac{\partial k}{\partial x_j}\frac{\partial \omega}{\partial x_j}, 10^{-10}\right] \tag{2.64}$$

The blending function F_1 is also used to blend the constants in the $k-\epsilon$ and the $k-\omega$ model to obtain the constants for the SST model as shown below:

$$\sigma_k = \frac{1}{F_1/\sigma_{k1} + (1-F_1)/\sigma_{k2}}, \qquad \sigma_\omega = \frac{1}{F_1/\sigma_{\omega 1} + (1-F_1)/\sigma_{\omega 2}} \tag{2.65}$$

$$\alpha = F_1\alpha_1 + (1 - F_1)\alpha_2, \qquad \beta = F_1\beta_1 + (1 - F_1)\beta_2 \tag{2.66}$$

where α_1 and α_2 are defined as

$$\alpha_1 = \frac{\beta_1}{\beta^*} - \frac{\kappa^2}{\sigma_{\omega 1}\sqrt{\beta^*}}, \qquad \alpha_2 = \frac{\beta_2}{\beta^*} - \frac{\kappa^2}{\sigma_{\omega 2}\sqrt{\beta^*}} \tag{2.67}$$

$$F_2 = \tanh\left(\Phi_2^2\right), \qquad \Phi_2 = \max\left[2\frac{\sqrt{k}}{0.09\omega y}, \frac{500\nu}{y^2\omega}\right] \tag{2.68}$$

where y is the distance to the nearest surface. The eddy viscosity ν_t is obtained from

$$\nu_t = \frac{k}{\omega}\frac{1}{\max\left[\frac{1}{\alpha^*}, \frac{SF_2}{a_1\omega}\right]} \tag{2.69}$$

where S is the magnitude of the strain rate.

The constants in the SST model are $\sigma_{k1} = 1.176$, $\sigma_{\omega 1} = 2.0$, $\sigma_{k2} = 1.0$, $\sigma_{\omega 2} = 1.168$, $a_1 = 0.31$, $\beta_1 = 0.075$, $\beta_2 = 0.0828$ and $\beta^* = 0.09$.

2.2.3 Reynolds Stress Transport model

The Reynolds stress transport model (RSTM) does not employ an eddy viscosity assumption to calculate the Reynolds stresses; instead a transport equation is solved for each of the six components of the Reynolds stresses. Eddy viscosity models assume that the principal axes of the Reynolds stress tensor are always aligned with those of the strain rate tensor. In three-dimensional flows, the angle of the Reynolds shear stress ($\tan^{-1}\langle v'w'\rangle/\langle u'v'\rangle$) often lags the horizontal mean shear angle ($\tan^{-1}\langle \partial W/\partial y\rangle/\langle \partial U/\partial y\rangle$) whereas eddy viscosity models, by design, predict that these two angles are equal. In applications where the turbulence mixing is either

enhanced or suppressed in one direction selectively due to stratification, curvature or rotational effects, eddy viscosity models, which use the same length scale in all directions, provide poor results. In all these applications, RSTM models, which have the capability to better predict the Reynolds stress anisotropy, may provide better results and their use is justified despite the higher computational cost incurred in solving the additional transport equations. The RSTM model used in this work is summarized below. Interested reader can obtain more details from Launder *et al.* [66] and Launder [65].

The transport equations for the Reynolds stresses are

$$\frac{\partial \overline{u_i u_j}}{\partial t} + C_{ij} = D_{T,ij} + D_{M,ij} + P_{ij} + \phi_{ij} - \epsilon_{ij} \tag{2.70}$$

where C_{ij} represents the convection, $D_{T,ij}$ represents the turbulent diffusion, $D_{M,ij}$ represents the molecular diffusion, P_{ij} represents the production, Φ_{ij} represents the pressure-strain and ϵ_{ij} represents the dissipation of the Reynolds stresses. They are defined as

$$C_{ij} = \frac{\partial}{\partial x_k}\left(u_k \overline{u_i' u_j'}\right), \tag{2.71}$$

$$D_{T,ij} = -\frac{\partial}{\partial x_k}\left[\overline{u_i' u_j' u_k'} + \overline{\frac{p}{\rho}\left(\delta_{kj} u_i' + \delta_{ik} u_j'\right)}\right] \tag{2.72}$$

$$D_{M,ij} = \frac{\partial}{\partial x_k}\left(\nu \frac{\partial}{\partial x_k}\overline{\left(u_i' u_j'\right)}\right), \tag{2.73}$$

$$P_{ij} = -\left(\overline{u_i' u_k'}\frac{\partial u_j}{\partial x_k} + \overline{u_j' u_k'}\frac{\partial u_i}{\partial x_k}\right) \tag{2.74}$$

$$\phi_{ij} = \overline{-p\left(\frac{\partial u_i'}{\partial x_j} + \frac{\partial u_j'}{\partial x_i}\right)}, \tag{2.75}$$

$$\epsilon_{ij} = 2\nu \overline{\frac{\partial u_i'}{\partial x_k}\frac{\partial u_j'}{\partial x_k}} \tag{2.76}$$

While the convection, molecular diffusion and the production terms in the above equation can be evaluated from the flow field, the turbulent diffusion, pressure-strain and the dissipation terms need to be modeled.

The pressure-strain term ϕ_{ij} represents the redistribution of energy from one Reynolds stress component to another. It is decomposed into three terms;

$$\phi_{ij} = \phi_{ij,1} + \phi_{ij,2} + \phi_{ij,w} \tag{2.77}$$

where $\phi_{ij,1}$ is the slow pressure-strain term or the return-to-isotropy term, $\phi_{ij,2}$ is the rapid pressure-strain term, and $\phi_{ij,w}$ is the wall-reflection term.

The slow and rapid pressure-strain terms, $\phi_{ij,1}$ and $\phi_{ij,2}$, are modeled as

$$\phi_{ij,1} = -C_1 \frac{\epsilon}{k}\left[\overline{u_i' u_j'} - \frac{2}{3}\delta_{ij}k\right] \tag{2.78}$$

$$\phi_{ij,2} = -C_2\left[(P_{ij} + F_{ij} - C_{ij}) - \frac{2}{3}\delta_{ij}\left(P - C\right)\right], \tag{2.79}$$

with $P = P_{kk}/2$ and $C = C_{kk}/2$.

The wall-reflection term, $\phi_{ij,w}$ damps the normal stress perpendicular to the wall, while enhancing the stresses parallel to the wall. This term is modeled as

$$\begin{aligned}\phi_{ij,w} = {} & C_1^d \frac{\epsilon}{k}\left[\overline{u_k' u_m'} n_k n_m \delta_{ij} - \tfrac{3}{2}\overline{u_i' u_k'} n_j n_k - \tfrac{3}{2}\overline{u_j' u_k'} n_i n_k\right] \frac{k^{\frac{3}{2}}}{C_l \epsilon d} \\ + {} & C_2^d \frac{\epsilon}{k}\left[\phi_{km,2} n_k n_m \delta_{ij} - \tfrac{3}{2}\phi_{ik,2} n_j n_k - \tfrac{3}{2}\phi_{jk,2} n_i n_k\right] \frac{k^{\frac{3}{2}}}{C_l \epsilon d}\end{aligned} \tag{2.80}$$

where n_k is the kth component of the unit normal to the wall, d is the normal distance to the wall, and $C_\ell = C_\mu^{3/4}/\kappa$, where $C_\mu = 0.09$ and $\kappa = 0.4187$.

The constants in the above equations are evaluated using

$$C_1 = 1 + 2.58A\sqrt{A_2}\left(1 - \exp\left[-\left(0.0067Re_t\right)^2\right]\right), \qquad C_2 = 0.75\sqrt{A} \tag{2.81}$$

$$C_1^d = -\frac{2}{3}C_1 + 1.67 \qquad C_2^d = \max\left[\frac{\frac{2}{3}C_2 - \frac{1}{6}}{C_2}, 0\right] \tag{2.82}$$

with the turbulent Reynolds number defined as $Re_t = (k^2/\nu\epsilon)$. The parameter A and tensor invariants, A_2 and A_3, are defined as

$$A = \left[1 - \frac{9}{8}\left(A_2 - A_3\right)\right], \qquad A_2 = a_{ik}a_{ki}, \qquad A_3 = a_{ik}a_{kj}a_{ji} \tag{2.83}$$

where a_{ij} is the Reynolds-stress anisotropy tensor, defined as

$$a_{ij} = -\left(\frac{-\overline{u_i'u_j'} + \frac{2}{3}k\delta_{ij}}{k}\right) \tag{2.84}$$

The turbulent diffusion term $D_{T,ij}$ is modeled using the gradient-diffusion model of Daly and Harlow [28] and it takes the following form

$$D_{T,ij} = \frac{\partial}{\partial x_k}\left(\nu_t \frac{\partial \overline{u_i'u_j'}}{\partial x_k}\right) \tag{2.85}$$

In this equation, the eddy-viscosity, ν_t, is obtained by solving the ϵ equation.

$$\frac{D\epsilon}{Dt} = \frac{\partial}{\partial x_j}\left[\left(\nu + \frac{\nu_t}{\sigma_\epsilon}\right)\frac{\partial \epsilon}{\partial x_j}\right] + C_{\epsilon 1}\frac{1}{2}P_{ii}\frac{\epsilon}{k} - C_{\epsilon 2}\frac{\epsilon^2}{k} \tag{2.86}$$

$$\nu_t = C_\mu \frac{k^2}{\epsilon}, \qquad k = \frac{1}{2}\overline{u_i u_i} \tag{2.87}$$

where the constants in the above two equation are $\sigma_\epsilon = 1$, $C_{\epsilon 1} = 1.44$, $C_{\epsilon 2} = 1.92$ and $C_\mu = 0.09$. The scalar dissipation ϵ computed from the above equation is used to model the dissipation tensor by assuming it is isotropic.

$$\epsilon_{ij} = \frac{2}{3}\delta_{ij}\epsilon \tag{2.88}$$

2.3 Numerical technique for LES

Large-eddy simulation involves the discretization of the governing differential equations [Eq. (2.3) and (2.4)] to algebraic equations on discrete points in the domain of interest that are then numerically solved. Large-eddy simulation requires even the smallest resolved scale of the motion be solved accurately which necessitates the use of accurate discretization scheme. Accuracy of a LES simulation is affected by the truncation, aliasing and modeling errors. The truncation error is due to the computation of derivatives of a continuous function with the data from discrete points and a limitation of any numerical scheme. While spectral methods are able to represent the derivatives accurately up to the cutoff wave number (a measure of the smallest resolvable length scale by the discrete approximation), the accuracy of derivatives calculated using finite difference approximation deteriorates near the cutoff wavenumber (See the modified wavenumber analysis in Moin [81]). Although this feature makes the spectral method attractive for turbulent flow computations, they are seldom used in complex geometries because of the difficulty in their implementation. Finite-difference or finite volume approximations, because of the ease in the implementation, are typically employed in complex geometries. The nonlinear terms in the Navier-Stokes equation generate higher wavenumber than the actual cutoff wavenumber in the discretization and the energy in the wavenumbers higher than the cutoff wavenumber is falsely represented in resolved wavenumbers that are below the cutoff wavenumber. The error thus introduced by the higher

wavenumbers is known as 'aliasing error'. (See Canuto *et al.* [20] for a detailed discussion). The modeling error is due to the limitations of the subgrid model and this can be reduced by careful choosing of the most accurate subgrid model available for the problem in hand.

Various authors have done careful analysis of different sources of numerical errors in LES. Ghosal [45] performed *a priori* analysis with a randomly generated flow field that had von Karman spectrum to estimate the magnitude of truncation and aliasing errors. His *a priori* analysis showed that even with high-order finite difference schemes, truncation error is always larger than the subgrid scale stresses a potentially serious problem since this questions the usefulness of including the subgrid scale stresses. He also showed that the aliasing error is larger for spectral schemes compared to low order finite difference schemes; a fact consistent with the modified wavenumber analysis which shows the finite difference schemes damp the high wavenumber content thereby reducing the aliasing error. He suggests using low order finite difference scheme with filters whose width is larger than the grid spacing. Although his analysis yielded useful information, *a priori* analysis cannot account for the dynamic interaction between the various sources of errors and might imply more stringent requirements than actually necessary. Kravchenko and Moin [64] performed channel flow simulation using various forms of the non-linear term with low and high order finite difference and spectral schemes. They showed both analytically and also *posteriori* that of all the four forms of the non-linear

term namely the divergence, the advective, the skew-symmetric and the rotational form, the skew-symmetric form has the lowest aliasing error, rotational form has the largest aliasing error and the advective and the divergence forms have error between that of these two forms. They also verified *a posteriori* Ghosal's result that spectral scheme has higher aliasing error compared to the high order finite difference scheme followed by the low order finite order schemes. Chow and Moin [25] performed an *a priori* analysis similar to the one performed by Ghosal but with a more realistic turbulent flow field obtained from a stably stratified homogeneous flow simulation. Their analysis of truncation error showed the same trend as Ghosal's analysis. However, with the realistic flow field used, they found that aliasing error dominates the SGS stresses only in the high wavenumber region unlike Ghosal's analysis which predicted that the aliasing error is always larger than SGS stresses.

Ghosal [45], and Chow and Moin [25] *a priori* analysis suggests that to keep the truncation error magnitude lower than the SGS stresses it is necessary to use a explict filter whose width is wider than the grid spacing. The downside in using a wider filter is the loss of resolution. For example, the effective resolution achieved in a simulation with a filter that is twice as wide as the grid spacing in each direction is equivalent to a simulation with half the number of grid points in each direction. In other words, a simulation with the explicit filtering approach increases the cost of the simulation by an order of magnitude. Lund [73] performed *posteriori* analysis to investigate any gains in accuracy with the explicit filtering. His results from channel

flow did not show any appreciable differences in the predicted flow field between the calculations with and without explict filtering as the mesh was refined. Hence no explicit filtering was performed in this work.

A second order finite volume discretization is used in this work following Silva Lopes and Palma [109]. In finite volume discretization for complex geometries, the use of staggered arrangement, where the velocity components are placed on the face center, requires storage of 3 variables for cell volumes and 27 variables for the face normal vector. The non-staggered layout, where all the variables are stored at the cell center, requires the storage of 1 variable for the cell volume and 9 variables for the face normal vector. The non-staggered approach was used in the current work because of its significantly lower memory usage. The numerical formulation is based on a finite volume method on a non-orthogonal curvilinear grid. A drawback of the non-staggered approach is the decoupling of the solution on alternate grid points and the resultant appearance of 'even-odd' oscillations in the flow field [42]. This oscillation can be reduced by using the method of Rhie and Chow [102]. Morinishi *et al.* [85] show that the error in the conservation of kinetic energy scales as $O(\Delta t|\Delta x^2)$ in this approach.

In finite volume methodology, the domain of interest is divided in to many small control volumes and in each of these control volumes, the integral form of the governing equations are discretized. One of the common features of the finite volume method is the transformation of terms in divergence form to terms that involve fluxes

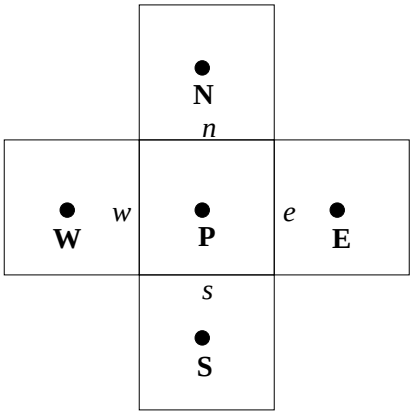

Figure 2.1: Control volume layout

across the surfaces of the control volume using Gauss' divergence theorem. Some of the key details used in the formulation of the numerical code are summarized below.

The continuity equation is integrated over the control volume Ω,

$$\int_{\Omega} \frac{\partial u_i}{\partial x_i} d\Omega = 0 \tag{2.89}$$

Using Gauss' divergence theorem, the above volume integral is transformed to a surface integral.

$$\int_S \mathbf{v} \cdot \mathbf{n} \, dS = \sum_l \int_{S_l} \mathbf{v} \cdot \mathbf{n} \, dS = \sum \dot{m}_l, \qquad l = e, w, n, s, t, b \tag{2.90}$$

In the above equation, $\mathbf{v}$ refers the velocity vector, $\mathbf{n}$ refers the unit normal vector to surface S. This code assumes the computational grid is structured which implies that every three dimensional control volume has six faces. Each of the six faces are represented by the subscript e, w, n, s, t and b (for east, west, north, south, top and bottom). $\dot{m}_l$ is the mass flux across each face. Control volume layout in a xy-plane is shown in the figure 2.1. The Navier-Stokes equation can be written in

the following form so that σ_{ij} contains the viscous stresses and any subgrid scale or Reynolds stresses that would be included in a LES or RANS formulation.

$$\frac{\partial u_i}{\partial t} + \frac{\partial u_i u_j}{\partial x_j} = -\frac{\partial p}{\partial x_i} + \frac{\partial \sigma_{ij}}{\partial x_j} \tag{2.91}$$

The above equation is integrated over the control volume and the divergence terms are transformed to terms that invole surface fluxes,

$$\frac{\partial}{\partial t}\int_\Omega u_i \, d\Omega + \int_S u_i \mathbf{v}\cdot\mathbf{n} \, dS = -\int_S p \, \mathbf{i_i}\cdot\mathbf{n} \, dS + \int_S \sigma_{ij}\mathbf{i_j}\cdot\mathbf{n} \, dS \tag{2.92}$$

where $\mathbf{i_j}$ is the unit vector along direction x_j. The convective terms are discretized as

$$\int_S u_i \mathbf{v}\cdot\mathbf{n} \, dS = \sum_l \int_{S_l} u_i \mathbf{v}\cdot\mathbf{n} \, dS = \sum_l F^c_{i,l}, \qquad l = e, w, n, s, t, b \tag{2.93}$$

The convective fluxes across all six faces are summed in the above equation. The convective flux across the east surface is given by

$$F^c_{i,e} = \int_{S_e} u_i \mathbf{v}\cdot\mathbf{n} \, dS \approx \dot{m}_e u_{i,e} \tag{2.94}$$

where the velocity at the face of the control volume ($u_{i,e}$) is obtained by linear interpolation of the velocities at cell centers P and E. When the line connecting cell center P and E pass through the face center e, the interpolation is second order accurate. Figure 2.2 illustrates the effect of grid distortion on the order of the accuracy of the linear interpolation. In the figure shown, the grid distortion reduces the order of accuracy of the interpolation to less than two as the interpolated value is second order accurate at e' but the face center is at e.

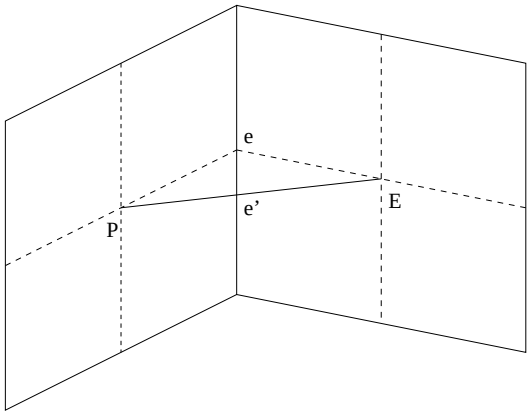

Figure 2.2: Interpolation of cell center values to face center

The diffusive term is discretized as

$$\int_S \sigma_{ij}\mathbf{i_j}\cdot\mathbf{n}\;dS = \sum_l \int_{S_l} \sigma_{ij}\mathbf{i_j}\cdot\mathbf{n}\;dS = \sum F^d_{i,l}, \qquad l = e,w,n,s,t,b \tag{2.95}$$

The diffusive flux across the east face in the u-momentum equation, $F^d_{1,e}$ is defined as

$$F^d_{1,e} = \int_{S_e} \sigma_{1j}\mathbf{i_j}\cdot\mathbf{n}\;dS \approx \left(\sigma_{1j}\right)_e \mathbf{i_j}\cdot\mathbf{S_e} \tag{2.96}$$

where $\mathbf{S_e}$ is the surface area vector of the east face. When the diffusive fluxes are evaluated directly using σ_{ij} on the face, oscillation occur in the flow field [42]. This issue is related to the 'even-odd' oscillations that occur in the pressure field in a non-staggered arrangement and is due to the fact that the derivative are evaluated using data that are $2\Delta x$ apart. A deferred correction approach is used to damp the oscillations [42]. With this approach, the diffusive flux on the east face for u-momentum equation is given by

$$F^d_{1,e} = \underbrace{\nu_e \frac{\mathbf{S_e}\cdot\mathbf{S_e}}{\mathbf{S_e}\cdot\mathbf{\Delta r}}\left(u_e - u_p\right)}_{I} - \underbrace{\nu_e \frac{\mathbf{S_e}\cdot\mathbf{S_e}}{\mathbf{S_e}\cdot\mathbf{\Delta r}}\frac{\partial u}{\partial x_k}\Delta r_k}_{II} + \underbrace{\left(\sigma_{1j}\right)_e \mathbf{i_j}\cdot\mathbf{S_e}}_{III} \tag{2.97}$$

where $\Delta\mathbf{r}$ is the vector joing the cell center P to the neighboring cell center E on the east side. ν_e is the sum of kinematic and subgrid scale viscosities. If the current cell center P, the neighboring cell center at E and the face center on e, lie on the same line, Term I in Eq. 2.97 is equal to the actual diffusion evaluated using velocities that are Δx apart. Derivatives in the cell centers P and E are interpolated to face center e, to evaluate term II in the Eq. 2.97. If 'even-odd' oscillation start to appear in the flow field, the difference of term I and term II will damp the oscillations. Term III is evaluated from its definition.

$$(\sigma_{1j})_e S_e^j = (\sigma_{11})_e S_e^x + (\sigma_{12})_e S_e^y + (\sigma_{13})_e S_e^z \tag{2.98}$$

$$= 2\nu_e \left(\frac{\partial u}{\partial x}\right)_e S_e^x + \nu_e \left(\frac{\partial u}{\partial y} + \frac{\partial v}{\partial x}\right)_e S_e^y + \nu_e \left(\frac{\partial u}{\partial z} + \frac{\partial w}{\partial x}\right)_e S_e^z \tag{2.99}$$

A second-order semi-implicit fractional-step [62] procedure is used for the temporal discretization. The Crank-Nicolson scheme is used for the temporal discretization of wall-normal diffusive terms, and the Adams-Bashforth scheme is used for the temporal discretization of all the other terms. The discretization of the Navier-Stokes equation is given by

$$\frac{u_i^* - u_i^n}{\Delta t} = -\frac{3}{2}\sum_{S_l} \dot{m}_l^n u_{i,l}^n + \frac{1}{2}\sum_{S_l} \dot{m}_l^{n-1} u_{i,l}^{n-1} - \sum_{S_l} p^n S_l^i + F_{diff,i}^n + F_{diff,i}^* \tag{2.100}$$

where the superscripts $n-1$ and n denote the values at previous and current time level and $*$ denotes the predicted values at the next time level. $F_{diff,i}$ denotes the denotes the diffusion term given by the Eq. 2.95. All the diffusive fluxes on east, west, top and bottom faces are evaluated explicitly. Term I (Eq. 2.97) of the wall-

normal (north and south faces) diffusive fluxes is evaluated implicitly and terms II and III on north and south faces are evaluated explicitly.

$$F^*_{diff,i} = \frac{1}{2}\nu_n \frac{S^j_n S^j_n}{S^m_n \Delta r^m_{pn}} \left(u^*_{i,n} - u^*_{i,p}\right) + \frac{1}{2}\nu_s \frac{S^j_s S^j_s}{S^m_s \Delta r^m_{ps}} \left(u^*_{i,p} - u^*_{i,s}\right) \tag{2.101}$$

where the subscripts n and s refers the values on north and south faces respectively. Δr^m_{ps} is the vector joining the cell center P to the neighboring cell center S on the south side and Δr^m_{pn} is the vector joining the cell center P to the neighboring cell N on the north side. The convective fluxes are calculated using the method of Rhie and Chow [102]. For example, the convective flux on the east face is obtained by the following equation.

$$\dot{m}^{*n+1}_e = \sum_i \overline{\left(u^{*n+1}_i\right)}_e S^i_e + \Delta t \frac{S^i_e S^i_e}{S^m_e \Delta r^m_{pe}} \left(p_e - p_p - \frac{\partial p}{\partial x_k} \Delta r^k_{pe}\right) \tag{2.102}$$

Discrete mass conservation in the cell is not satisfied by the above fluxes, evaluated with the predicted velocity, which does not satisfy the continuity equation. In the next step, the following equation is solved for pressure correction, $\Delta p^{n+1} = p^{n+1} - p^n$, that would ensure the fluxes satisfy the continuity equation.

$$\sum \Delta t S^i_l \frac{\delta \Delta p^{n+1}}{\delta x_i} = \sum \dot{m}^{*n+1}_l, \qquad l = e, w, n, s, t, b \tag{2.103}$$

The velocities at the cell center and fluxes are updated after obtaining the pressure correction.

$$u^{n+1}_i = u^{*n+1}_i - \Delta t \frac{\delta \Delta p^{n+1}}{\delta x_i} \tag{2.104}$$

$$\sum \dot{m}^{n+1}_e = \sum \dot{m}^{*n+1}_e - \Delta t \sum_i S^i_e \left(\frac{\delta \Delta p^{n+1}}{\delta x_i}\right)_e \tag{2.105}$$

All the problems studied in this work uses periodic boundary condition in the z direction. This enabled us to use Fourier transforms in z direction to reduce the three-dimensional Poisson equation into a series of two-dimensional Helmholtz equations in wavenumber space, which are then solved iteratively using the Biconjugate Gradient Stabilized (BCGSTAB) method. The code is parallelized using the MPI message-passing library and the domain-decomposition technique.

2.3.1 Boundary condition

At the walls, the no-slip boundary condition is enforced. In the finite volume formulation, this implies that all the convective fluxes are zero through the wall. When the boundary faces are not aligned along the Cartesian coordinate plane, the calculation of diffusive fluxes is tricky. The total diffusive flux on the boundary face is calculated from the derivative of the tangential component of the velocity. The components of the total diffusive fluxes along the Cartesian coordinate directions, obtained by projecting the total diffusive flux along the unit surface normal vector of the boundary faces, are then used as boundary fluxes in the respective momentum equations.

At boundaries where free-slip condition is used, the normal component of the velocity is set to zero and the normal gradients of the velocity components parallel to the boundary are zero. The normal gradient of the normal component of the velocity contributes to the normal stress at the boundary and is non-zero. The

normal stress is projected along the various Cartesian components using the surface normal vector of the face. All the convective fluxes through the boundary face are zero. At the outlet, the convective condition $\partial\overline{u}_i/\partial t + U_b\,\partial\overline{u}_i/\partial x = 0$ was used [91].

2.4 Numerical technique for RANS

The RANS version of the Spalart-Allmaras (SA-RANS) is obtained by using the distance from the wall as the length scale in the destruction term (*i.e.*, $\widetilde{d} = y_w$). The finite-volume code was used to obtain the SA-RANS solution, while the commercial software FLUENT$^{\text{TM}}$ (version 6.2.16) was used to obtain solution with other RANS models. In FLUENT$^{\text{TM}}$, the governing equations are discretized by a finite volume approach; the convective terms are discretized by a QUICK scheme and the governing equations are solved by a segregated approach. The pressure field is obtained using the SIMPLE algorithm which enforces the mass conservation. FLUENT$^{\text{TM}}$ solves the linear system that arises from the discretization of the momentum and transport equation by using a point implicit (Gauss-Seidel) linear equation solver in conjunction with an algebraic multigrid method.

The SA-RANS solution obtained with FLUENT$^{\text{TM}}$ was found to agree exactly with the SA-RANS solution of the finite volume code, indicating that any error due to difference in the numerical approach between FLUENT$^{\text{TM}}$ and our finite-volume code has negligible effect on the prediction of the flow field. Hence, FLUENT$^{\text{TM}}$ was used to perform calculations based on other RANS models such as the $k-\epsilon$

model, the Shear Stress Transport (SST) model [80] and a Reynolds-stress transport model.

For the RANS calculations in FLUENT^{TM}, the pressure-outlet condition is used at the outflow, which extrapolates the flow properties from the interior of the domain. The FLUENT^{TM} solution was obtained by iterating until the residuals in the continuity, momentum and the transport equations for the variables used in the modeling of the Reynolds stresses, was less than 10^{-6}. Here, the residual for the continuity equations is defined as the sum of the absolute value of the mass imbalance in all the cells at any iteration divided by the sum of the absolute value of the mass imbalance in all the cells at the fifth iteration. For the momentum and the other transport equations, the residual, R^{ϕ}, is defined as

$$R^{\phi} = \frac{\sum_{\text{cells } P} |\sum_{\text{nb}} a_{\text{nb}}\phi_{nb} + b - a_P\phi_P|}{\sum_{\text{cells } P} |a_P\phi_P|} \tag{2.106}$$

where the terms in the above equation appear in the discretized equation for a variable ϕ at a cell P as shown below. Here, the subscript nb refers the neighboring cells.

$$a_P\phi_P = \sum a_{nb}\phi_{nb} + b \tag{2.107}$$

Chapter 3

Flow past a contoured ramp

This chapter presents results from numerical simulations of a flow with mild separation. The flow configuration consists of a developing turbulent boundary layer on a flat plate region, followed by a smoothly contoured ramp where the turbulent boundary layer separates and then reattaches on another flat region behind the ramp. LES and RANS computations have been carried at a momentum Reynolds number of 13,200 at the computational inlet section; the numerical results are compared to the experimental results of Song and Eaton [124, 122].

3.1 Introduction

Separated flows occur in many engineering devices such as airfoils, turbine blades, combustion chamber, road vehicles etc. Separation might be undesirable in application such as airfoil where it leads to loss of efficiency while it might be desirable in applications such as combustion chambers in which enhanced mixing of fuel and air is needed. Understanding of separated flows is crucial to improve the design of these devices. Progress made in the understanding of separated flows are summarized in review articles by Bradshaw and Wong [17], Eaton and Johnston [40], Simpson [111] and Simpson [112].

Based on the nature of separation, separation can be either geometry-induced separation or adverse-pressure-gradient induced. In geometry-induced separation the location of the separation point is fixed at the step change in the geometry, whereas in the pressure gradient induced separation, the separation point location varies in both time and space and the mean separation point is determined by the magnitude of the adverse pressure gradient. Alving and Fernholz [3] further distinguish between strong and mild separation: in strong separation, the bubble height is comparable to the pre-separation boundary layer thickness, whereas in mild separation the bubble height is smaller than the pre-separation boundary layer thickness.

As the boundary layer is subjected to adverse pressure gradient, it thickens and the flow decelerates until the separation point, where there is a reversal of flow in the near wall region. Once the applied adverse pressure gradient is removed, the flow reattaches. A separated free shear layer, which resembles the mixing layer and bounds the recirculation region, is subjected to curvature and pressure gradient effects. The Reynolds stresses increase in the adverse pressure gradient region until they reach a maximum in the recirculation region. The location of the peak of the Reynolds stresses, which is in the inner region in zero-pressure-gradient region, moves away from the wall as the flow approaches separation and the Reynolds stress peaks align with the inflection point of the mean velocity profile in the separation region [123]. After the reattachment, the turbulence in the free shear layer diffuses

outwards and slowly decays along the streamwise direction. A turbulent boundary layer starts to grow from the near wall region and slowly penetrates the free shear layer.

Simpson and coworkers [113, 114, 108] provide detailed mean and Reynolds stress statistics for a two-dimensional turbulent boundary-layer flow subjected to flow acceleration and deceleration that separates, a set up that mimics airfoil type flow. They show that separation occurs very close to the location where the adverse pressure gradient decreases rapidly. They also observe that the turbulent fluctuating velocities are as high as the mean velocity in the separation region, and the correlation between the streamwise and the wall-normal velocities are reduced in the separation region. The smoke visualization study indicates that the back flow in the separation region is supplied by the large-scale structures as they pass through the separation region. Analyzing the turbulence energy budget, they isolate turbulent energy diffusion as the mechanism that supplies energy in the separation region rather than the turbulence production which is negligible there.

Chandrsuda and Bradshaw [22] studied experimentally a backward facing step flow at a Reynolds number of 10^5 based on step height. They observed that the semi-logarithmic profile of the mean velocity in the recovery region following the reattachment has a dip below the standard log-law which was also seen by Bradshaw and Wong [17]. They attribute this difference from the standard log-profile to the larger length-scale in the re-attaching free shear compared to the length-scale in the

zero pressure gradient flow. This larger length-scale results in a smaller velocity for a given shear stress and this results in the dip below the logarithmic law. They also measure three triple correlations (namely $\overline{u^2v}, \overline{v^3}$ and $\overline{uv^2}$) that play a role in the transport of the turbulence energy across the wall-normal direction. They show that all three triple-correlation profiles before the reattachment have an anti-symmetrical behavior similar to the one observed in the plane mixing layer. Subsequent to the reattachment, the peak of the triple correlation decays along the streamwise direction and the anti-symmetric profile slowly changes to the bell-shaped profile normally seen in the boundary layer flows.

Castro and Haque [21] studied the separated shear layer in a configuration that has a flat plate normal to airflow with a splitter plate behind the normal flat plate. They provide experimental measurements of mean velocity profile and Reynolds stresses for a flow at a Reynolds number of 2×10^4 based on the plate height. They observe that the turbulence level in the separated shear layer is considerably higher than the plane mixing layer and the shear layer growth rate is initially higher than the linear plane mixing layer growth rate and reduces gradually as the reattachment is approached. Even though the qualitative features in the separated shear and the plane mixing layer are the same, the flow development is different.

Le *et al.* [68] performed direct numerical simulation of backward facing step flow at a Reynolds number of 5100 based on step height. The temporal trace of the spanwise averaged reattachment location showed a saw-tooth behavior. They

attribute this behavior to the low frequency motion or the "flapping" of the separated shear layer observed by Eaton and Johnston [40] and Driver *et al.* [36, 37]. They conjecture that, as the shear layer moves downstream from the step, it rolls up to form a large-scale structure; the growth of the large-scale structure leads to the movement of the reattachment location downstream at a constant speed given by the positive slope of the saw-tooth profile. When the shear layer detaches from the step, the reattachment point moves suddenly upstream causing the drop in the reattachment location seen in the saw-tooth profile. This process is repeated periodically. They show that in the recirculation region, turbulent transport removes energy from the shear layer and supplies it to regions near wall; the peak dissipation is approximately 60% of the peak production in the shear layer; the production term becomes a consuming term in the near wall region which they attribute to the negative gradient of the mean reverse flow.

Na and Moin [88] performed direct numerical simulation of a separated turbulent boundary layer flow. The momentum Reynolds number of the incoming flow is 300 and they apply suction and blowing at the upper boundary to create an adverse-to-favorable pressure gradient which results in a closed separation bubble. They also observe the saw-tooth behavior of the spanwise averaged reattachment point. While the instantaneous reattachment point shows very little variation along the spanwise direction, the instantaneous separation point shows a rather large variation along the separation point. They attribute this to streaks present in the upstream region,

where the high speed streak delays the separation but a low speed streak causes an earlier separation.

3.2 Problem formulation

The flow configuration (see the sketch in figure 3.1) consists of a flat plate followed by a smoothly contoured ramp and another flat plate region. Experiments on this geometry were conducted by Song and Eaton [124]. One of the main challenges of this geometry is the fact that the separation point is not fixed by the geometry but determined by the pressure gradient. The accurate prediction of the separation and re-attachment points is, therefore, an important feature of any numerical model of this flow.

In the numerical calculations, all the lengths are normalized by the ramp length, $L_R = 70$ mm. The flat plate section preceding the ramp is $2L_R$ long; the radius of curvature of the ramp is $1.814L_R$, its height is $0.3L_R$. In the numerical calculations, the flat plate region following the ramp has a length of $6L_R$ followed by a buffer zone for the outflow boundary. An upper wall is present, $1.8714L_R$ above the top of the ramp, far enough that the two boundary layers are separated by a potential core whose height is equal to three boundary layer thickness at the inlet of the computational domain.

As the turbulent boundary layer goes over the ramp, the flow expands, creating an adverse pressure gradient that causes the flow to separate on the ramp.

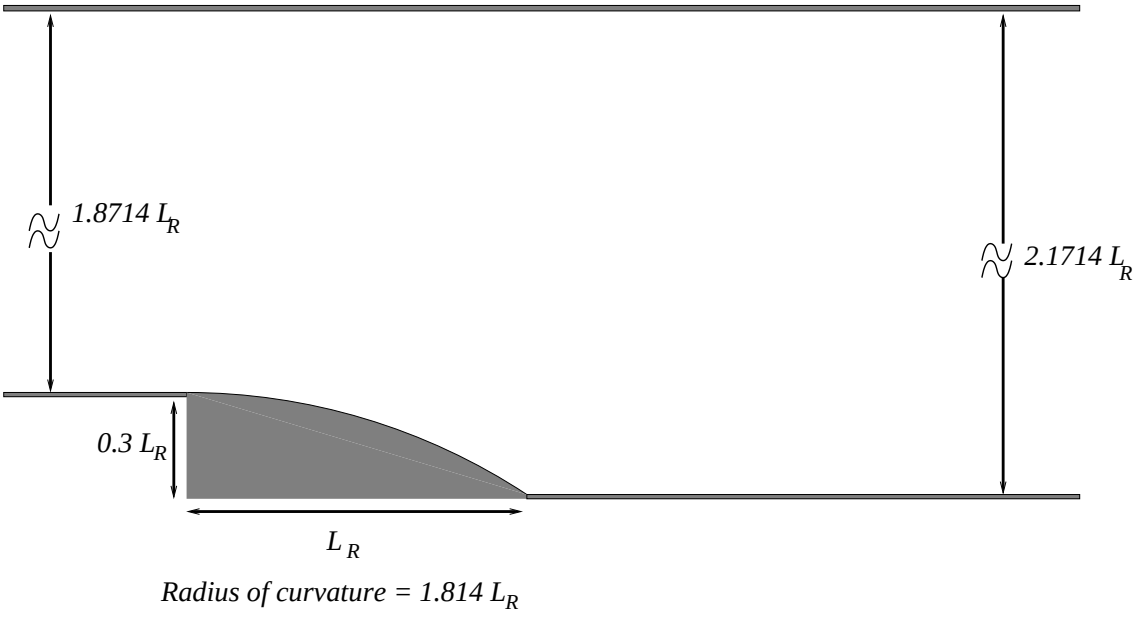

Figure 3.1: Flow configuration for the contoured ramp calculation.

The flow subsequently re-attaches on the flat plate region. Experimental data are available at various streamwise locations: $2L_R$ ($x = -2$) upstream of the ramp, at the point where the ramp begins ($x = 0$), at the separation point ($x = 0.76$), at the trailing edge of the ramp ($x = 1$), at the re-attachment point ($x = 1.39$) and at two locations in the recovery region ($x = 4$ and 7). Velocities are normalized by the free-stream velocity at the reference location $x = -2$, $U_{ref} = 20.3$ m/s. The momentum Reynolds number (Re_θ) at the reference location is 13,200, and the boundary layer thickness, δ_{ref}, is 0.38. The spanwise width of the computational domain is chosen to be $3\delta_{ref}$.

RANS simulations were performed using the SA model ($\widetilde{d} = y_w$), the $k - \epsilon$ model and the SST model. LES simulations were performed using various wall-

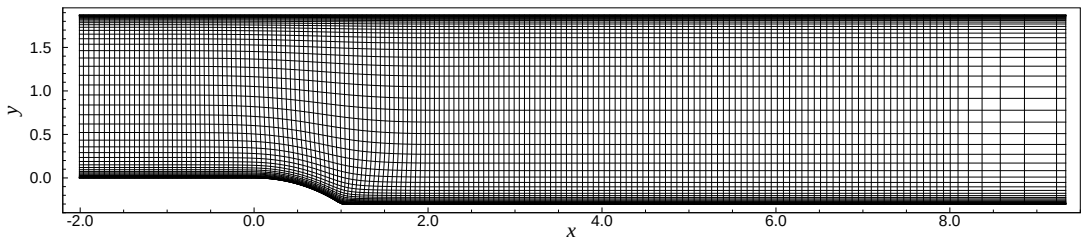

Figure 3.2: Grid used for the contoured ramp calculation. Every other point is shown.

models. The log-law boundary condition was tested with a Lagrangian dynamic subgrid scale model. Secondly, WMLES using the DES version of the SA model was tested with and without the application of the stochastic forcing; calculation for this case were performed on two grids to estimate the grid convergence of the predicted flow field.

In the RANS simulation, a grid with 367×120 nodes (in the streamwise and wall-normal directions, respectively) was used (see figure 3.2). Further refinement of the grid for the RANS calculations did not result in any change in the predicted flow field. The coarse WMLES simulation used the same grid as the RANS simulations but with 36 nodes in the spanwise direction. The grid was uniform in the spanwise direction and stretched in the streamwise and wall-normal directions. In the streamwise direction the grid was stretched only near the outlet to create a buffer region to avoid upstream propagation of disturbances. There were 12 points per δ_{ref} in the spanwise and streamwise directions (except near the outflow). In the wall-normal direction the first point was located at $y^+ = 1$ and the grid was stretched so that

near the boundary-layer edge there were 12 points per δ_{ref}, resulting in cubic grid cells in the outer region. The fine-mesh calculation performed for the WMLES case had 503×210×54 nodes in the streamwise, wall-normal and spanwise directions respectively, resulting in 18 points per δ_{ref} in the spanwise and streamwise directions. LES calculation using the log-law boundary condition requires the first point in the wall-normal to be in the outer region (where log-law is valid). This calculation used a grid with 367×60×36 nodes in the streamwise, wall-normal and spanwise directions respectively. The grid cells were approximately cubic everywhere except near the outlet. At the inlet, the first point in the wall-normal direction was at $y^+ = 250$.

For the LES and the WMLES, the inflow variables were assigned by reading a series of data planes obtained from auxiliary calculations of flat-plate boundary layers performed using the same methodology as the corresponding calculations of the ramp and the bump. The auxiliary calculation used the rescaling/recycling approach of Lund *et al.* [75] at the inlet. The inflow time-series was long enough (more than 10 flow-through times) that, after all transients, a sufficient statistical sample could be accumulated. The convergence of the results was estimated by comparing the statistics obtained using the two halves of the sample; they did not differ by more than 3%.

The results obtained with various RANS and LES simulations are summarized in the following two sections. In the first section, the results from all the RANS calculations and the LES calculation with log-law boundary condition are presented.

Case	Resolution	Separation point (% error)	Re-attachment point (% error)
Expt.	N/A	0.76	1.39
SA-RANS	367 × 120	0.79 (4.8%)	1.24 (-23.8%)
k-ϵ	367 × 120	0.79 (4.8%)	1.16 (-36.5%)
SST	367 × 120	0.69 (-11.1%)	1.36 (-4.7%)
Lagrangian with log-law	367×60×36	N/A	N/A

Table 3.1: Parameters in the ramp simulations

In the second section, the results from the four WMLES calculations are presented.

3.3 RANS and LES results

Figure 3.3 shows the flow streamlines superposed on contours of the Reynolds shear stress $\langle u'v' \rangle$. The separation and re-attachment points predicted by the various simulations shown in Figure 3.3 are also summarized in Table 3.3. RANS calculations with the Spalart-Allmaras model and the $k - \epsilon$ model predict a late separation and an early reattachment whereas the calculation with the SST model predicts an early separation. The LES calculation using the log-law boundary condition is unable to predict a separation; since the reversible flow region is thinner than the first grid height. With this approach, therefore, separation is a subgrid

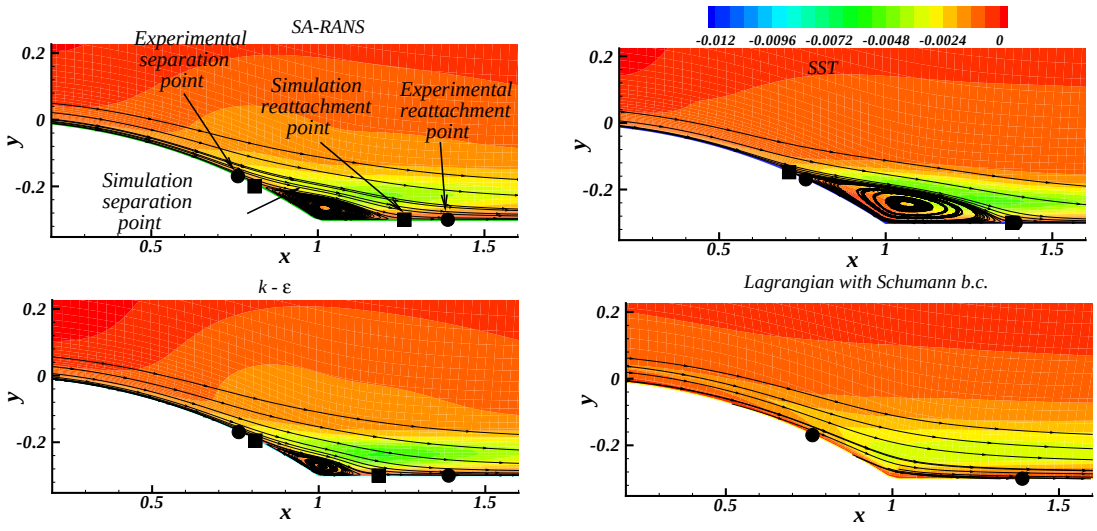

Figure 3.3: Mean Streamlines and contours of total Reynolds shear stress ($\langle u'v' \rangle$)

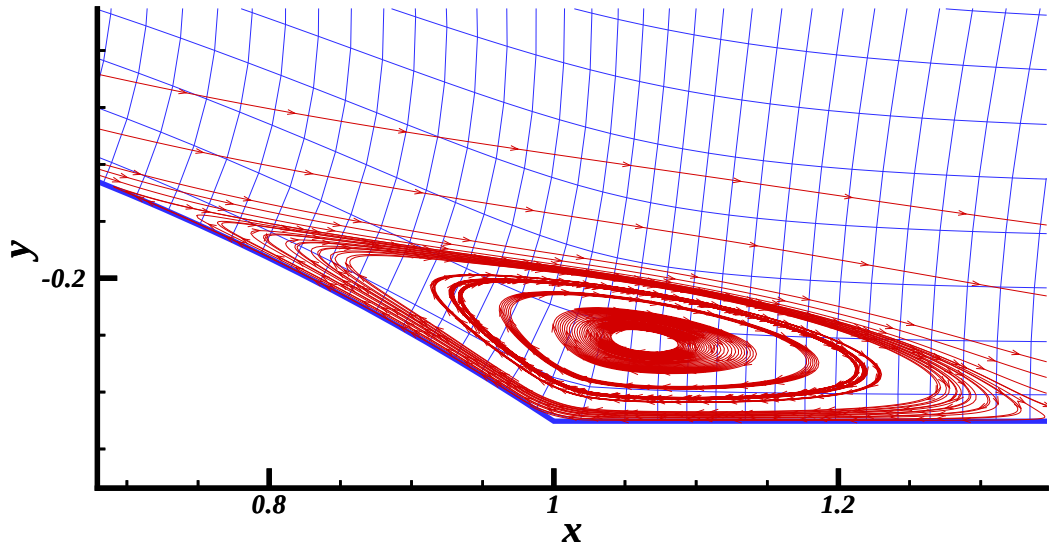

Figure 3.4: Mean Streamlines from SST model superposed on the grid used by LES calculation with log-law boundary condition

phenonmenon. Figure 3.4 infact shows the streamlines predicted by the SST model superposed on the grid used by the LES calculation with the log-law boundary condition. The reverse flow region lies within the first two points of the LES grid everywhere. This extremely short and mild separation cannot be predicted by the coarse wall-normal grid used in the LES calculation with log-law boundary condition. Although it might appear that improving the resolution of the LES grid in the wall-normal direction might result in better prediction, the assumption behind using log-law boundary condition no longer will hold if the wall-normal grid is refined excessively. It seems that LES calculations using log-law boundary condition are inherently incapable of predicting a mild separation such as the one observed in this geometry.

In the experiments, the separation and re-attachment points were determined from the sign of the velocity at a distance of 60 μm from the wall. This distance corresponds to $8.6 \times 10^{-4} L_R$, which, in the present RANS calculations, occurs 6–7 grid points away from the wall. For consistency with the experiments, the separation and re-attachment points reported in the Table 3.3 are obtained using the experimental criterion, and not the location where the shear stress changes sign. All the RANS models predict the location of the separation point within 12% of the experimental value (see Table 3.3), but one can observe significant differences in the shape of the recirculation bubble and location of re-attachment. The $k - \epsilon$ and the SA RANS calculations predict an early reattachment whereas the SST model

prediction is closer to the experimental reattachment point. Overall the bubble size and the shape predicted by the SST model agrees better with the experiments.

In figure 3.5 the skin friction and pressure coefficients, defined as

$$C_f = \frac{\tau_w}{\rho U_\infty^2/2}; \qquad C_p = \frac{p - p_{ref}}{\rho U_{ref}^2/2}, \tag{3.1}$$

(where U_∞ is the velocity at the edge of the boundary layer at the current location, and p_{ref} is the wall pressure at $x = -1.81$) are compared to the experimental data.

In the flat-plate region ahead of the ramp, all the calculations predict the skin-friction coefficient reasonably well. RANS calculations based on the SST model and the SA model predict a slow recovery after separation. RANS calculation based on the $k-\epsilon$ model predicts the recovery accurately, but this is due to its prediction of a weak recirculation bubble; and is a case of opposite errors canceling each other. Due to the same reason, the LES calculation with the log-law boundary condition predicts a faster recovery after the deceleration in the adverse pressure gradient region. All models predict the wall-pressure coefficient reasonably well. In the separation region, the wall-pressure coefficient prediction by the SST model, however, is in better agreement with the experiments due to its more accurate prediction of the shape and size of the recirculation bubble.

Figure 3.6 compares numerical and experimental data at five locations: in the equilibrium region, near separation, in the middle of the separation region, near re-attachment and in the recovery region. One can observe significant differences in the mean horizontal velocity prediction in the separated-flow region: the SA-RANS

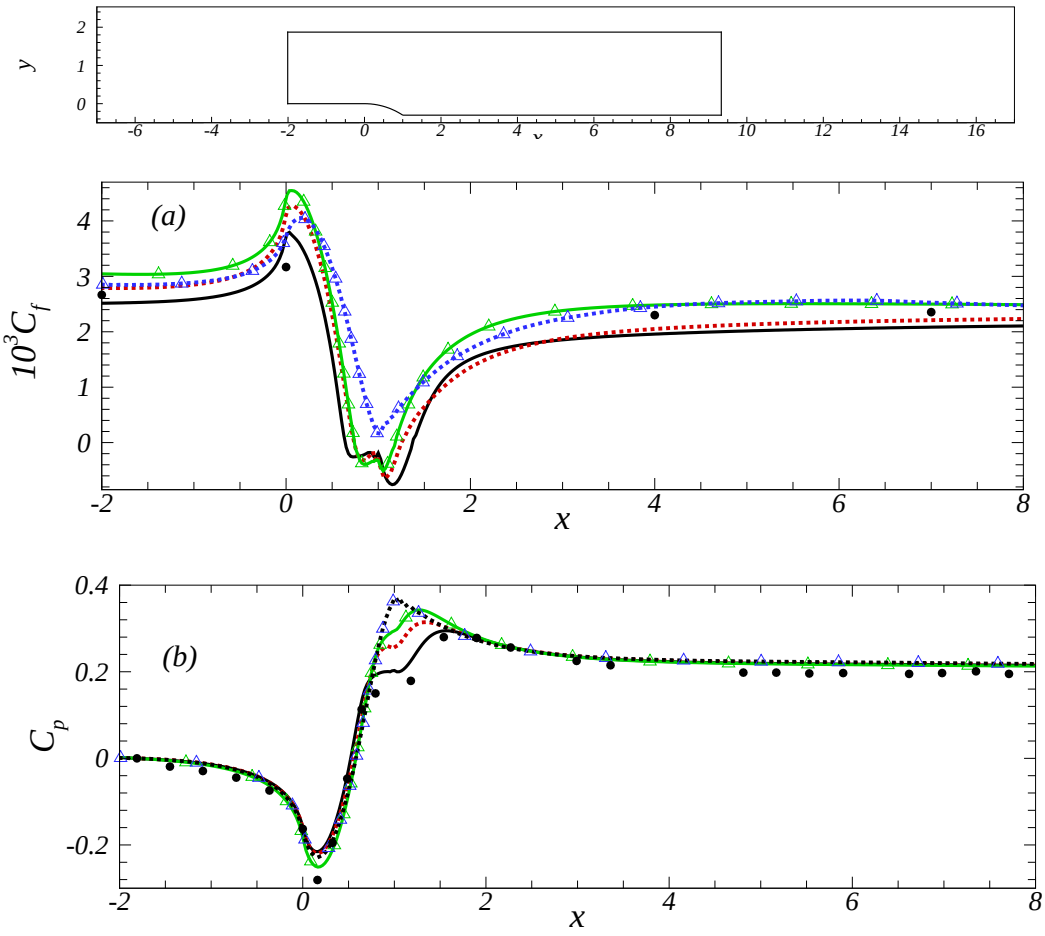

Figure 3.5: Profiles of (a) Skin friction coefficient and (b) Pressure coefficient. —— SST RANS; - - - SA-RANS model; —△— k-ϵ RANS; ---△--- Lagrangian with log-law; • Experiments.

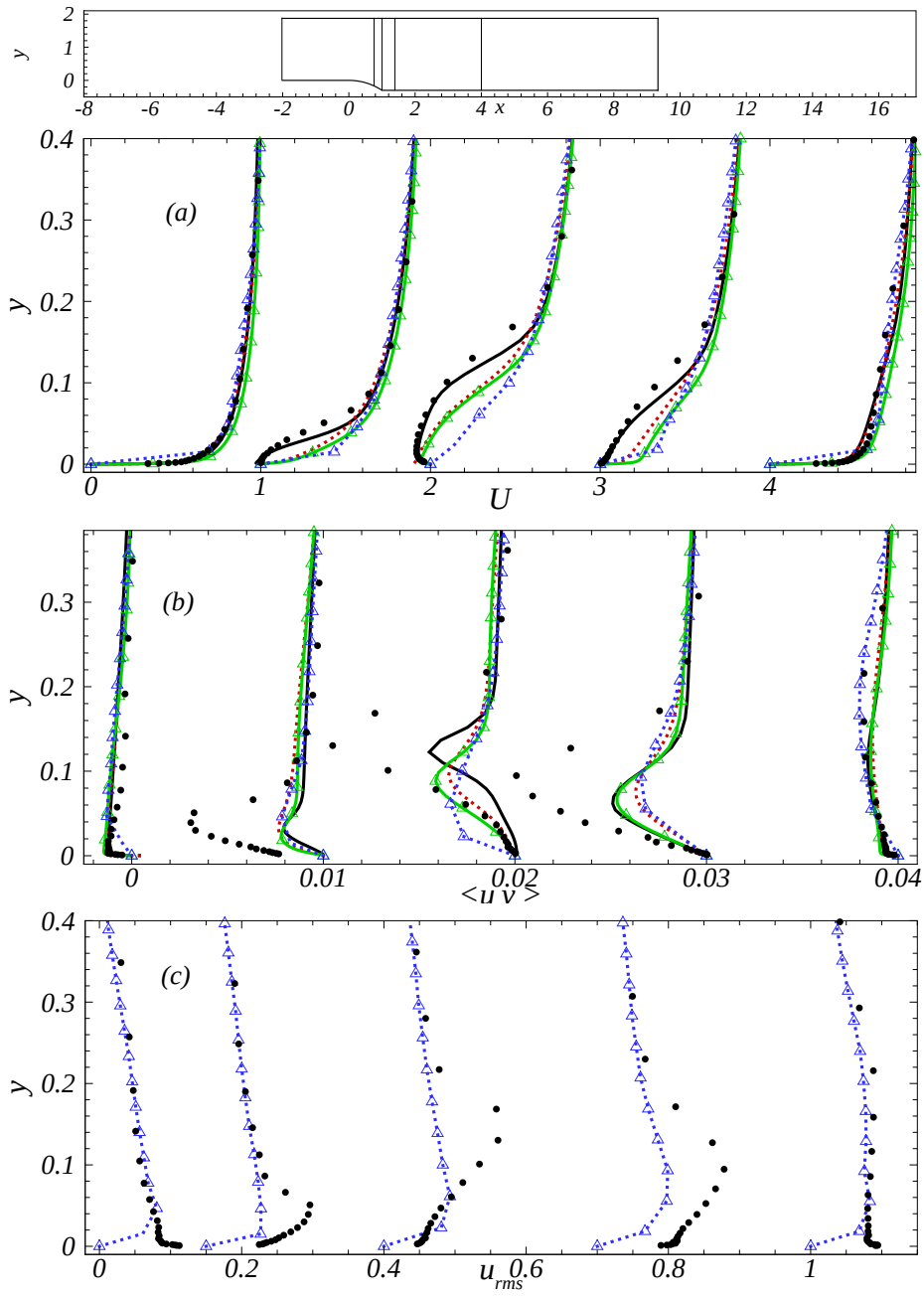

Figure 3.6: Profiles of (a) mean horizontal velocity, (b) total (resolved + modeled) Reynolds shear stress and (c) rms of horizontal velocity fluctuations. ——— SST RANS; - - - SA-RANS model; ——△—— k-ϵ RANS; ···△··· Lagrangian with log-law; • Experiments.

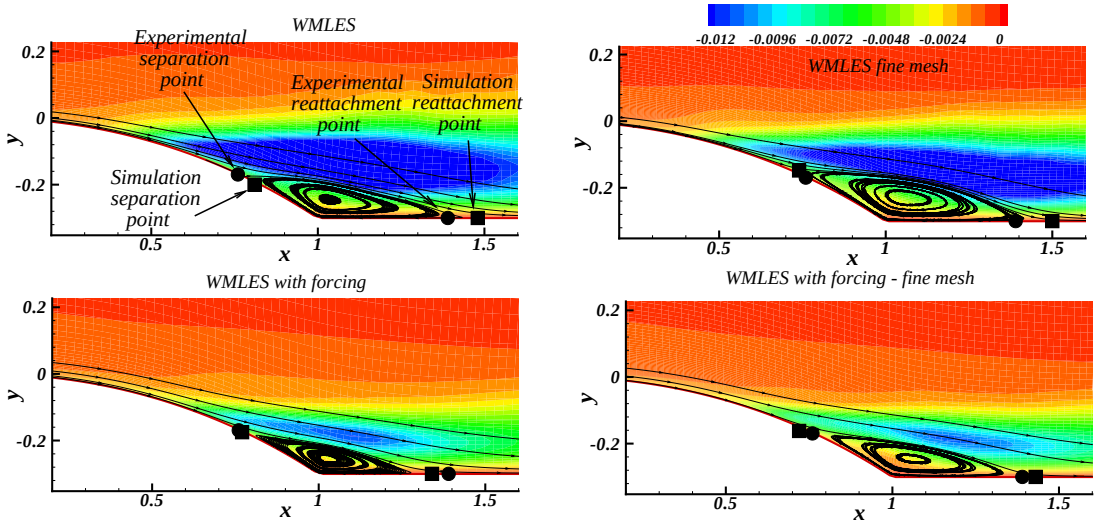

Figure 3.7: Mean Streamlines and contours of total Reynolds shear stress ($\langle u'v' \rangle$)

model and the $k - \epsilon$ model predict the smallest extent of the recirculation bubble, and the weakest back-flow; the SST model predicts the mean horizontal velocity accurately in the near-wall region but not the mean flow deceleration away from the wall. The LES calculation with the log-law boundary does not predict a back-flow at all. All the RANS calculation under-predict the Reynolds shear stress in the separation region; the SST model predicts the location of peak Reynolds shear stress accurately whereas the other RANS models predict the peak location closer to the wall. The LES calculation with the log-law boundary condition predicts the streamwise Reynolds stress elevation trend in the adverse pressure gradient region correctly but not the actual magnitude of the increase in streamwise Reynolds stress.

Case	Resolution	Separation point (% error)	Re-attachment point (% error)
Expt.	N/A	0.76	1.39
WMLES	$367 \times 120 \times 36$	0.80 (6.3%)	1.46 (11.1%)
WMLES (fine mesh)	$503 \times 210 \times 54$	0.72 (-6.3%)	1.48 (14.2%)
WMLES with stochastic forcing coarse mesh	$367 \times 120 \times 36$	0.75 (-1.6%)	1.32 (-11.1%)
WMLES with stochastic forcing fine mesh	$503 \times 210 \times 54$	0.7 (-9.5%)	1.41 (3.2%)

Table 3.2: Parameters in the ramp simulations

3.4 WMLES results

Streamlines in the separation region for the four WMLES calculation are shown in figure 3.7 along with the contours of the Reynolds shear stress $\langle u'v' \rangle$. Table 3.2 shows the predicted separation and re-attachment point location and the error in their prediction. The separation and re-attachment points are obtained by the same method as the experiments for a consistent comparison. All the calculations predict the location of the separation point within 10% of the experimental value and the re-attachment within 15% of the experimental value.

In Figure 3.8, the skin friction and the wall- pressure coefficients, defined in Eq. 3.1, are shown. In the flat-plate region ahead of the ramp, the WMLES without the stochastic forcing under-predict the skin-friction coefficient by 12-18%; this result is consistent with previous studies [90, 6, 96], in which the under-prediction of C_f is found to be due to the insufficient momentum transport in the RANS/LES transition region. After the separation, the C_f is in good agreement with the experiments for both the WMLES without the stochastic forcing. The fact that, in the recovery region, the WMLES without the stochastic forcing does not show the low C_f typically observed with this approach is due to the generation of turbulent eddies in the separated shear layer, which alleviates the RANS/LES transition. This issue will be further discussed later. The C_f in the upstream flat-plate region predicted by the WMLES with stochastic forcing shows excellent agreement with the experiments; the application of the stochastic forcing has aided in the generation of

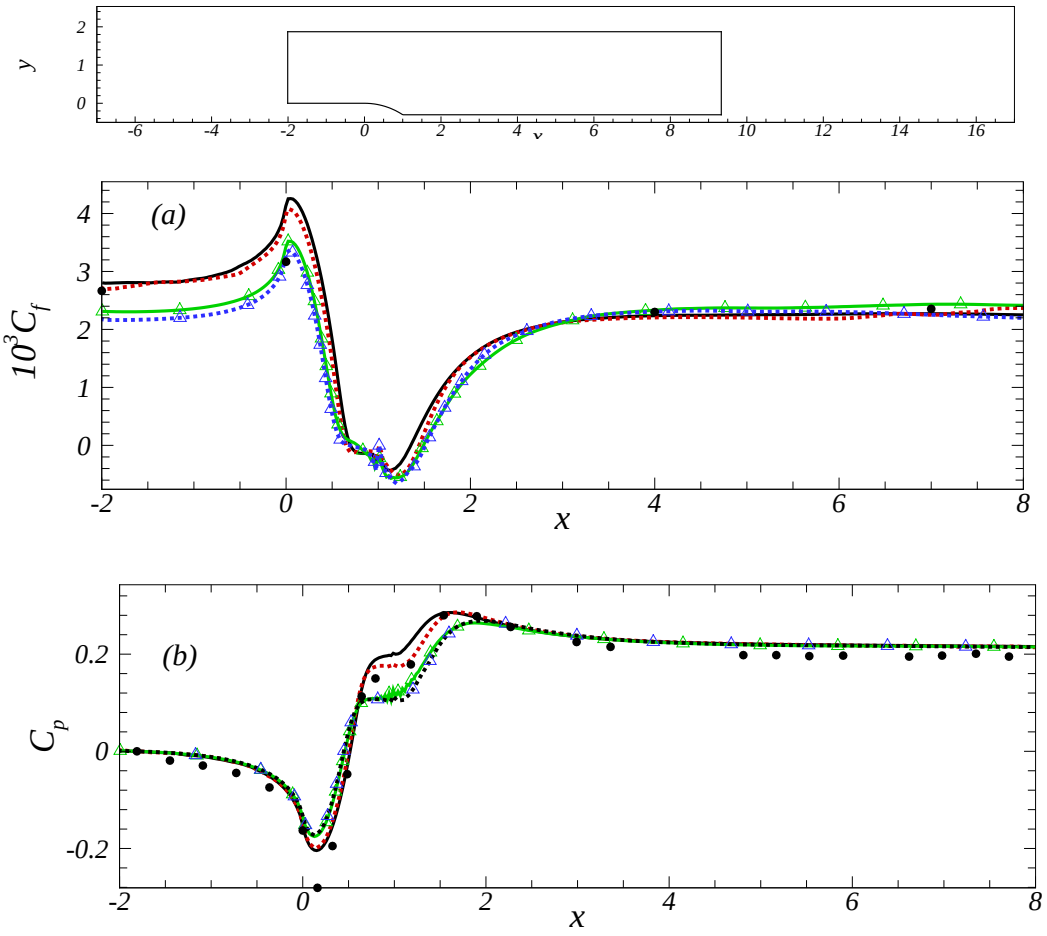

Figure 3.8: Profiles of (a) Skin friction coefficient and (b) Pressure coefficient. —— WMLES with stochastic forcing, coarse mesh; - - - WMLES with stochastic forcing, fine mesh; —△— WMLES without stochastic forcing, coarse mesh; ···△··· WMLES without stochastic forcing, fine mesh; • Experiments.

eddies in RANS/LES transition resulting in the better prediction of C_f [60]. All the calculations predict the wall-pressure coefficient accurately in the attached and the recovery region. The addition of the stochastic forcing has also resulted in improved agreement of wall-pressure coefficient in the separation region with the measured values in the experiment. Note, especially the remarkable agreement shown by the fine mesh WMLES calculation with stochastic forcing which indicates that it predicts the height of the bubble accurately.

The mean velocity profiles in wall coordinates at three locations are shown in figure 3.9. At the inlet, the WMLES without the stochastic forcing show the characteristic shift in the logarithmic law; the addition of the stochastic forcing has removed this shift. The WMLES without the stochastic forcing does not show the shift in the log-law in the return-to-equilibrium region; as mentioned above, this is a consequence of the fact that eddies generated in the separation region are convected downstream, and support resolved stress in the RANS/LES transition region. Notice that, while all the RANS calculations discussed in the previous section, predict the equilibrium boundary layer more accurately than the WMLES without the stochastic forcing, the opposite is true in the recovery region. This indicates that, if some mechanism is present to generate eddies in the RANS/LES transition, the better representation of the flow physics in the eddy-resolving calculation results in more accurate flow prediction. The WMLES with the stochastic forcing shows good agreement with the experimental values in the recovery region.

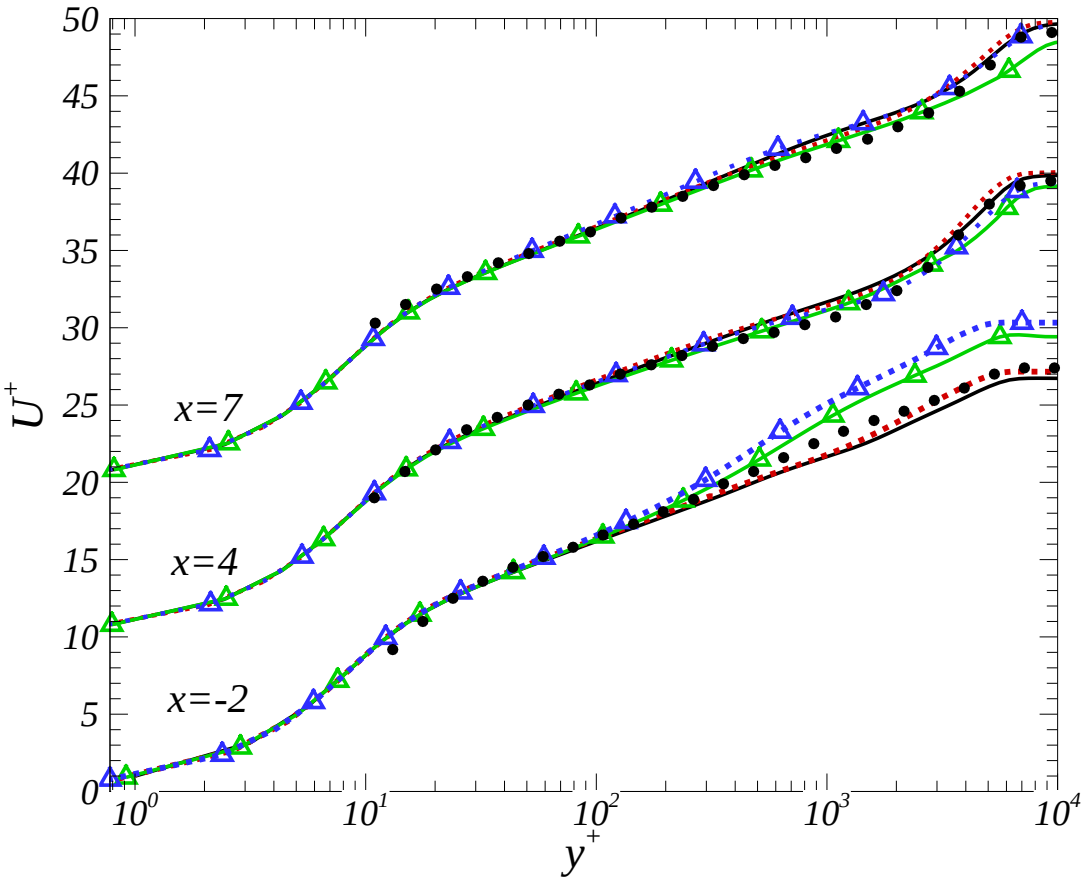

Figure 3.9: Mean velocity profile in wall-coordinates. —— WMLES with stochastic forcing, coarse mesh; - - - WMLES with stochastic forcing, fine mesh; —△— WMLES without stochastic forcing, coarse mesh; - -△- - WMLES without stochastic forcing, fine mesh; • Experiments.

Figure 3.10 compares numerical and experimental data at five locations: in the equilibrium region, near separation, in the middle of the separation region, near re-attachment and in the recovery region. The error in the mean velocity prediction by the WMLES with the stochastic forcing is less than the error without the stochastic forcing. Also the WMLES without the stochastic forcing over-predicts the Reynolds shear stress by as much as 100% in the separation region whereas the WMLES with the stochastic forcing shows a much better agreement with the experimental data.

Comparing the results of WMLES obtained with coarse and fine mesh, one observes less than 4% difference in the results in the equilibrium regions, and some differences (10% or less) in the separation region. This region is very sensitive to the upstream conditions, and small errors in the location of the separation point lead to changes in the shape of the recirculation bubble and in the location of the separated shear layer (seen in figure 3.7), with consequent shifts in the peak of the turbulent kinetic energy (which could be observed in figure 3.10). Although a fully grid independent result has not been obtained, the differences between the two meshes are sufficiently small to indicate that the grids used are sufficiently refined.

Two-point correlation for all the four WMLES calculations are compared to the experimental values. The streamwise two-point correlation is defined as

$$R_{uu,x} = \frac{\overline{u'(x)u'(x_0)}}{\sqrt{\overline{u'^2(x)}}\sqrt{\overline{u'^2(x_0)}}}, \qquad R_{vv,x} = \frac{\overline{v'(x)v'(x_0)}}{\sqrt{\overline{v'^2(x)}}\sqrt{\overline{v'^2(x_0)}}} \tag{3.2}$$

where u' and v' denote the fluctuating velocities and x_0 is the two-point correlation

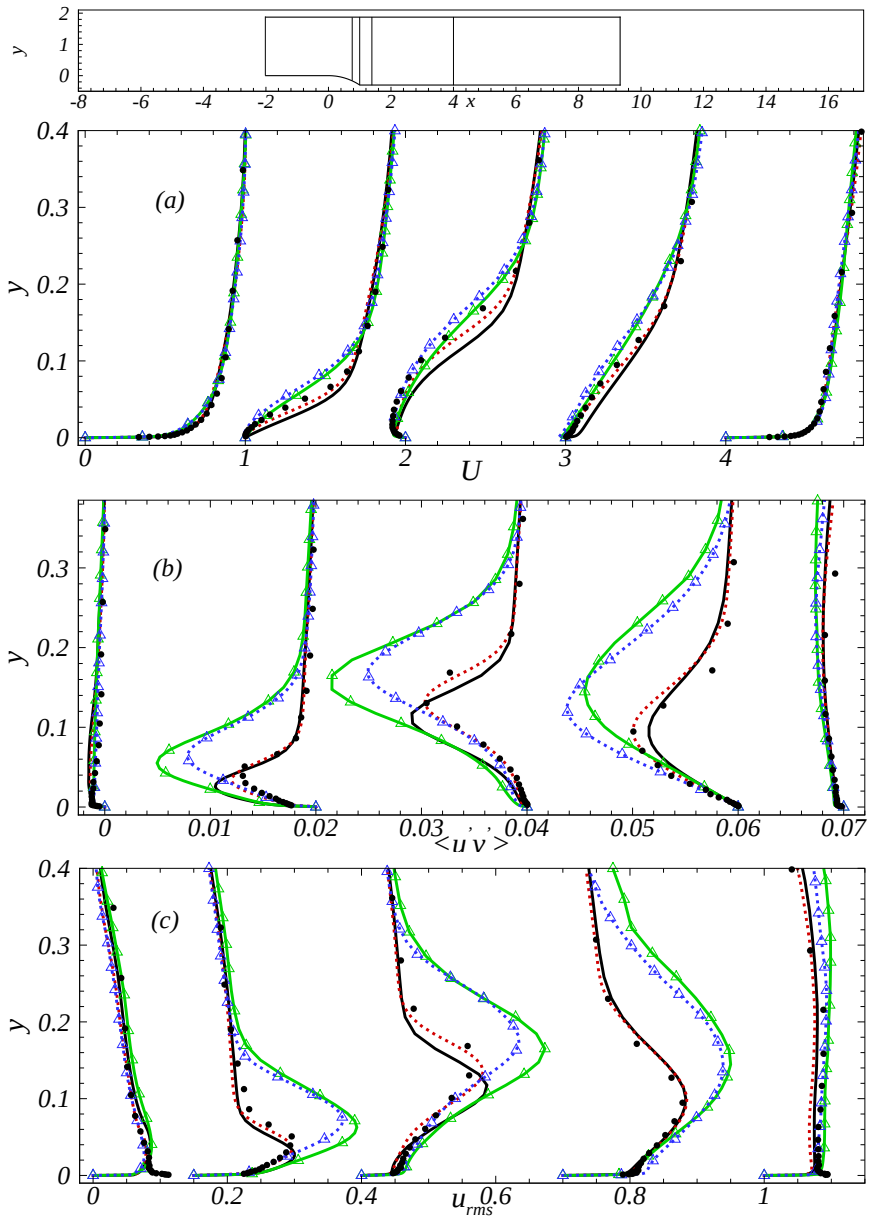

Figure 3.10: Profiles of (a) mean horizontal velocity, (b) total (resolved + modeled) Reynolds shear stress and (c) rms of horizontal velocity fluctuations. —— WMLES with stochastic forcing, coarse mesh; – – – WMLES with stochastic forcing, fine mesh; —△— WMLES without stochastic forcing, coarse mesh; ---△--- WMLES without stochastic forcing, fine mesh; • Experiments.

origin. Streamwise two-point correlations at three locations $x_0 = 1, 1.39$ and 4 are shown in figure 3.11. Correlations at $x_0 = 4$ are evaluated at a fixed height of 0.5δ whereas those at $x_0 = 1$ and 1.39 are evaluated along the mean streamline passing through the respective two-point correlation origin, which is at a height of 0.5δ. From the figure 3.11, one can see that calculations with the fine mesh predict a smaller streamwise length-scale than the calculations with coarse mesh and the addition of the stochastic forcing further reduces the streamwise length-scale. The streamwise length-scale of the u' fluctuations are predicted better than the streamwise length-scale of the v' fluctuations which is generally over-predicted. Note that in the separation region at $x = 1$, a much larger streamwise length-scale is predicted by the calculation without forcing which results in stronger eddies and over-prediction of the Reynolds stresses.

The wall-normal two-point correlation is defined as

$$R_{uu,y} = \frac{\overline{u'(y)u'(y_0)}}{\sqrt{\overline{u'^2(y)}}\sqrt{\overline{u'^2(y_0)}}}, \qquad R_{vv,y} = \frac{\overline{v'(y)v'(y_0)}}{\sqrt{\overline{v'^2(y)}}\sqrt{\overline{v'^2(y_0)}}} \tag{3.3}$$

where y_0 is the origin of the two-point correlation. Two-point correlation at $x = 1$ is evaluated at 0.22δ, $x = 1.39$ is evaluated at 0.2δ and at $x = 4$ and $x = 7$ are evaluated at 0.5δ. For the WMLES without the stochastic forcing, in the separation region, unlike the stream-wise length-scale of the u' fluctuations, the wall-normal length-scale of the u' fluctuations are predicted reasonably well suggesting that the streamwise fluctuations are coherent along the streamwise direction only. All the calculations over-predict the wall-normal length scale of the v' fluctuations.

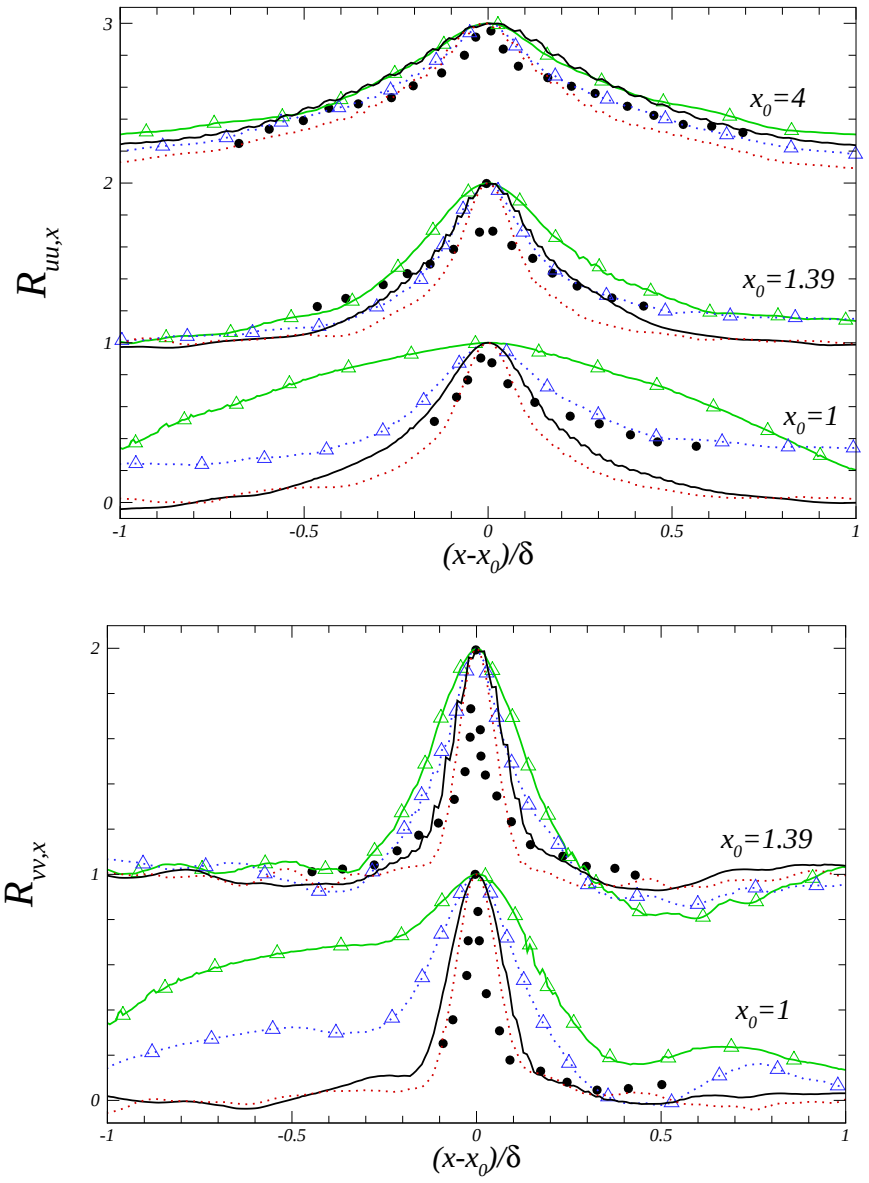

Figure 3.11: Profiles of (a) Streamwise two-point correlation of u' fluctuations (b) Streamwise two-point correlation of v' fluctuations. —— WMLES with stochastic forcing, coarse mesh; - - - WMLES with stochastic forcing, fine mesh; —△— WMLES without stochastic forcing, coarse mesh; ···△··· WMLES without stochastic forcing, fine mesh; • Experiments.

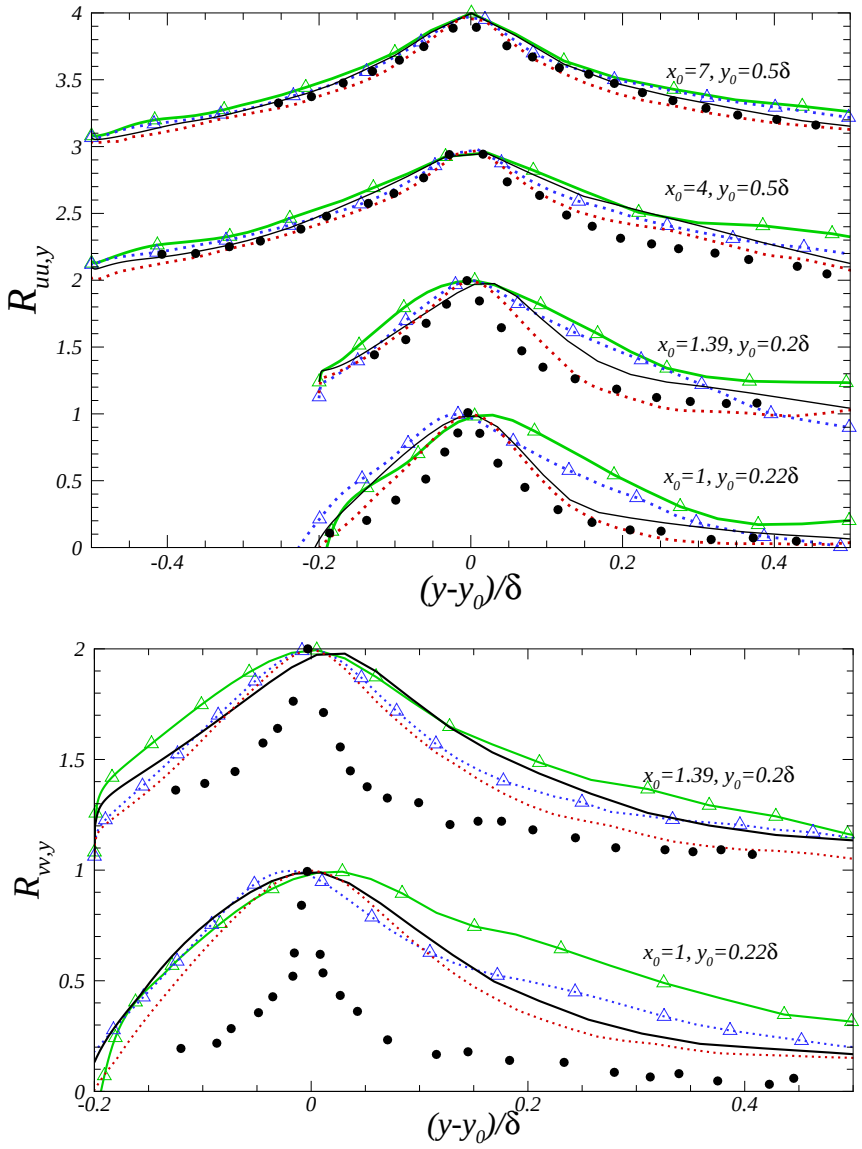

Figure 3.12: Profiles of (a) Wall-normal two-point correlation of u' fluctuations (b) Wall-normal two-point correlation of v' fluctuations. —— WMLES with stochastic forcing, coarse mesh; - - - WMLES with stochastic forcing, fine mesh; —— WMLES without stochastic forcing, coarse mesh; - - - WMLES without stochastic forcing, fine mesh; • Experiments.

In the WMLES without the stochastic forcing, the streaks present in the transition region between the RANS and the LES region are artificially long. These "super-streaks" can be observed in the flat plate region and tend to give higher levels of streamwise fluctuations (an issue also discussed in [6, 96, 95]). These high levels of turbulence are further amplified in the unstable shear layer. Hence, the wall-modeled LES calculations without the stochastic forcing predict high levels of $\langle u'v' \rangle$ (figure 3.10) in the recirculation region. With the addition of the stochastic forcing, these streaks are broken up and this results in better prediction of Reynolds stress in the downstream separation region.

Figure 3.13 shows iso-surfaces of the second invariant of the velocity-gradient tensor,

$$Q = -\frac{1}{2}\left(\frac{\partial \overline{u}_i}{\partial x_j}\frac{\partial \overline{u}_j}{\partial x_i}\right) = -\frac{1}{2}\left(\overline{S}_{ij}\overline{S}_{ij} - \overline{\Omega}_{ij}\overline{\Omega}_{ji}\right), \tag{3.4}$$

(where Ω_{ij} is the large-scale rotation-rate tensor) for the two WMLES without the stochastic forcing. Regions where $Q > 0$ identify coherent vortical motions [38]. Notice the presence of few turbulent eddies in the near-wall region upstream of the ramp, which is due to the significant extent of the transition region between RANS and LES [6, 96]. Figure 3.13 also shows the contours of the streamwise velocity fluctuation in a plane parallel to the wall which show the super-streaks in the upstream attached boundary layer region.

After the separation, the shear-layer instability leads to the formation of turbulent eddies. The resolved eddies generated in the unstable shear layer break up

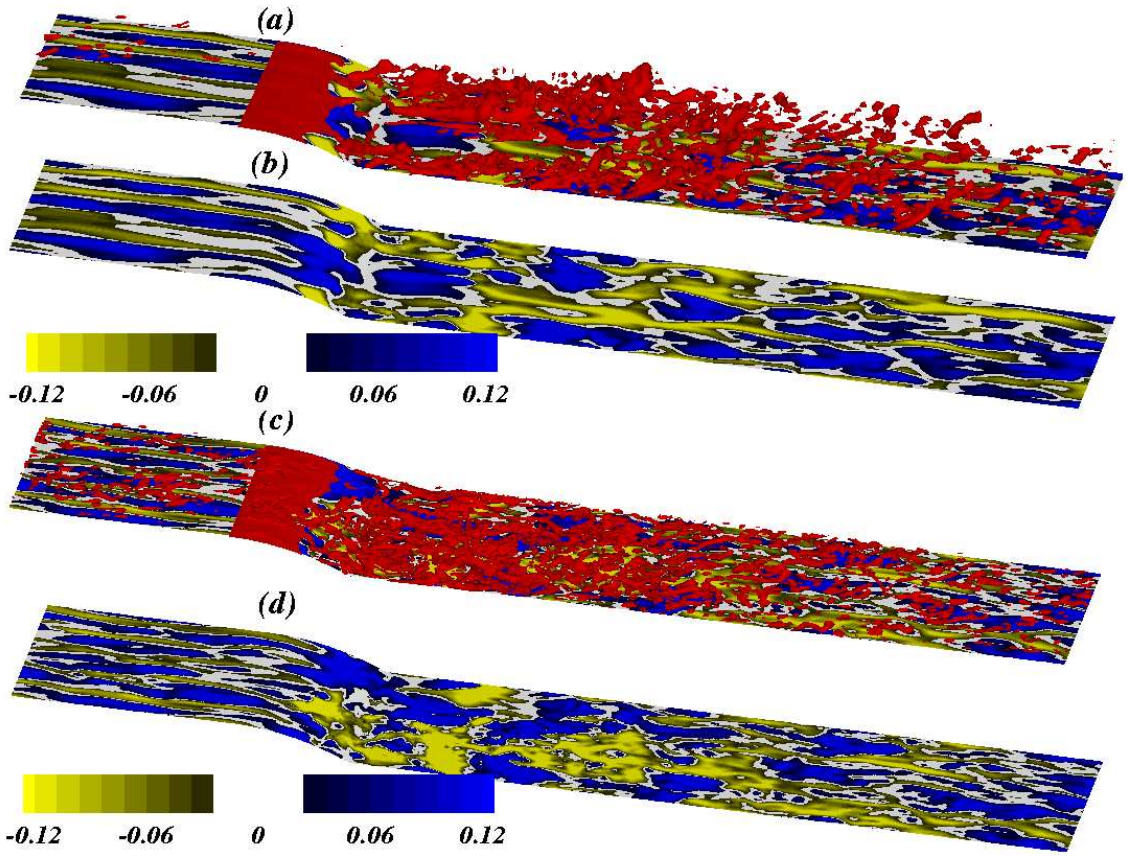

Figure 3.13: Iso-surfaces of $Q = 3$ [*(a)* and *(c)*] and and streamwise velocity-fluctuation contours in a plane parallel to the wall at $y_w = 0.017$ ($y_w/\delta_{ref} = 0.04$) [*(b)* and *(d)*]. *(a)* and *(b)* Coarse WMLES. *(c)* and *(d)* Fine WMLES.

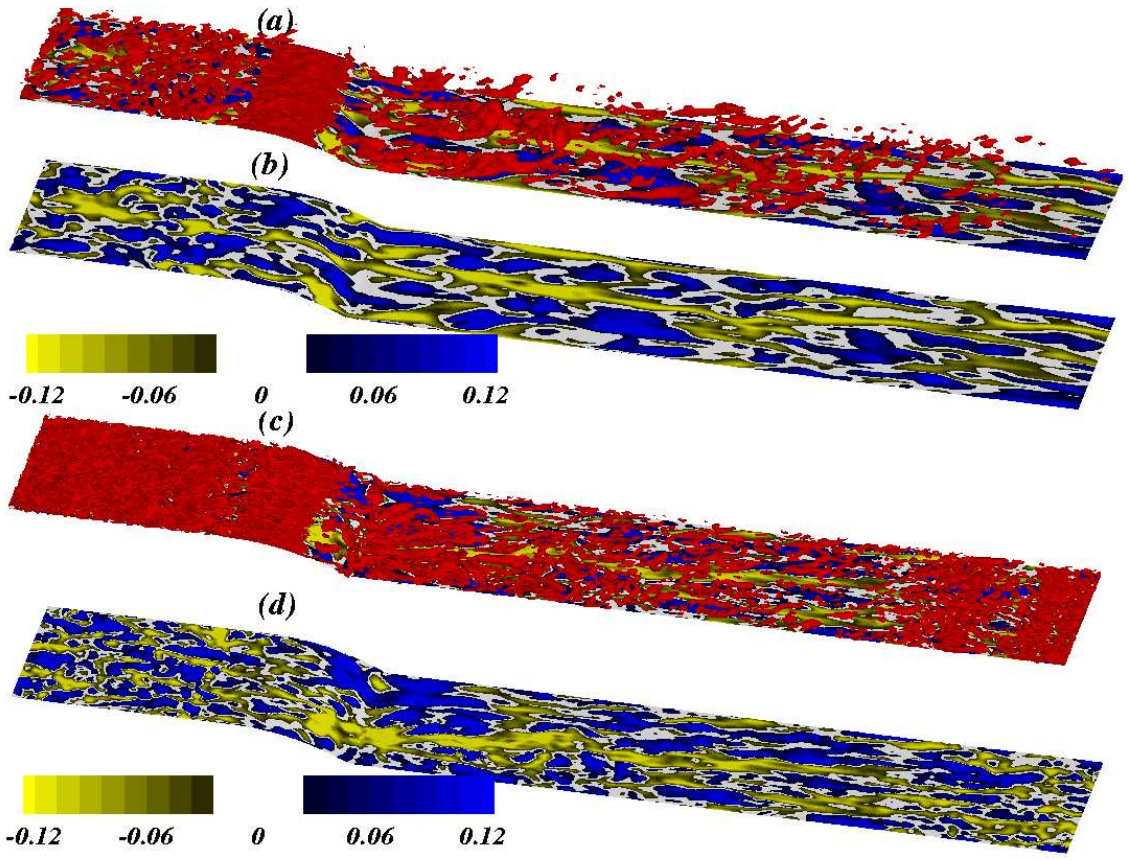

Figure 3.14: Iso-surfaces of $Q = 3$ [*(a)* and *(c)*] and and streamwise velocity-fluctuation contours in a plane parallel to the wall at $y_w = 0.017$ ($y_w/\delta_{ref} = 0.04$) [*(b)* and *(d)*]. *(a)* and *(b)* Coarse WMLES with stochastic forcing. *(c)* and *(d)* Fine WMLES with stochastic forcing.

the super-streaks in the recovery region; they convect downstream and decrease the extent of the RANS/LES transition in the recovery region by supplying the required resolved shear stress there. This results in better prediction of the recovery by the WMLES. Notice the larger eddies in the separation and recovery region for the coarse WMLES compared to the fine calculation. This leads to slightly higher levels of Reynolds stresses in the coarse WMLES case.

Figure 3.14 shows iso-surfaces of the Q and the streamwise velocity fluctuation contours on a plane parallel to the wall for the WMLES with stochastic forcing. As discussed before, the super-streaks in the upstream attached boundary layer region are broken up with the addition of the stochastic forcing and this region has more eddy content compared to the WMLES without stochastic forcing.

Figure 3.15 shows the contours of spanwise instantaneous vorticity in a xy-plane for the fine mesh case. The dashed line in the figure shows the nominal RANS/LES interface location. In the case without the stochastic forcing, resolved eddies appear in the upstream attached boundary layer only after a significant distance from the RANS/LES interface, while the calculation with the stochastic forcing has resolved eddies very close to it; they are responsible for the break-up of the super-streaks, and the better prediction of the skin-friction coefficient. After the flow separates, the inflectional instability provides a strong mechanism to generate eddies everywhere, including in the RANS/LES interface region, as reflected in the similarities between the calculations with and without the stochastic forcing. The

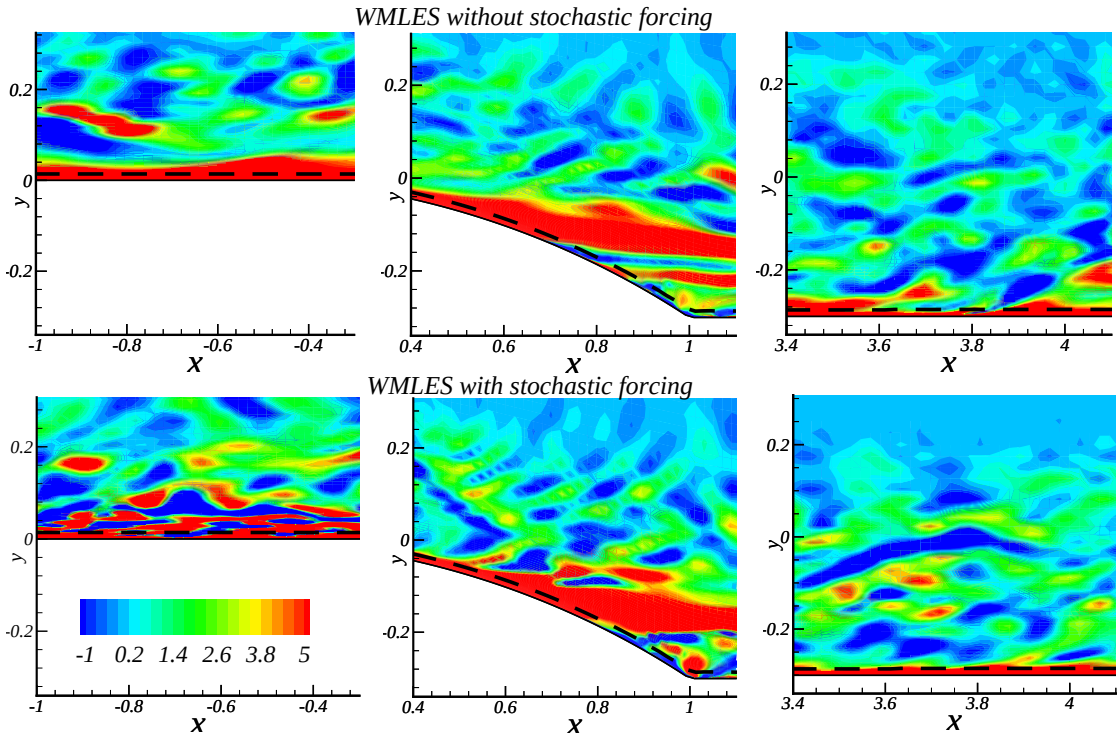

Figure 3.15: Contours of instantaneous spanwise vorticity in xy-planes for the fine mesh. The dashed line represents the nominal interface between RANS and LES regions.

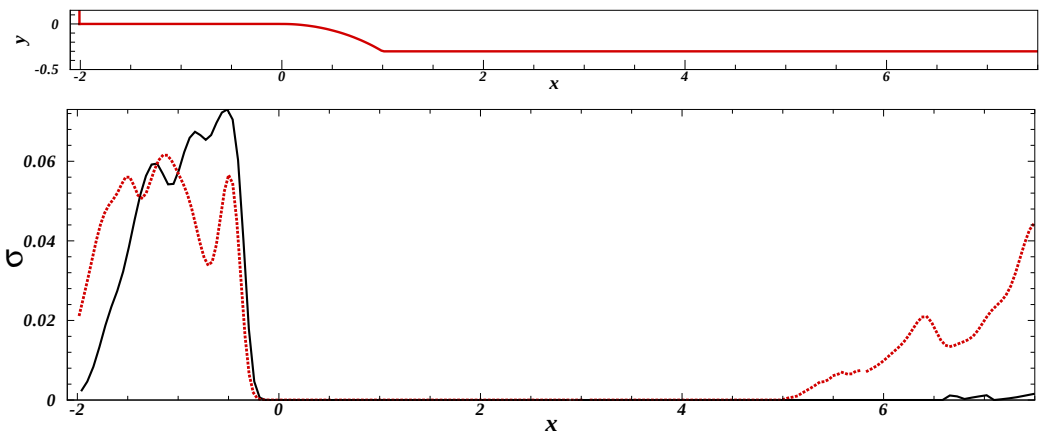

Figure 3.16: RMS of the stochastic forcing —— WMLES with stochastic forcing, coarse mesh; - - - WMLES with stochastic forcing, fine mesh;

.

generation of the resolved eddies in the shear layer is responsible for the accurate prediction of the skin-friction coefficient in the recovery region by both methods; there, the turbulent eddies appear very similar.

The amplitude of the stochastic forcing for the fine and coarse-mesh calculations is shown in figure 3.16. Note that the oscillations in the forcing amplitude are due to insufficient statistical convergence of the data, which is sampled less frequently than the velocity data. Significant forcing is applied only in the attached boundary layer region ahead of the ramp. Because of the convex curvature of the ramp, forcing is set to zero over the ramp. Although the dynamic controller was active downstream of the ramp, it does not apply stochastic forcing immediately downstream of the ramp as the eddies generated in the separated region resolve

most of the Reynolds stress. Only far downstream, where the eddies generated in the separation region have weakened or been dissipated by viscous effects, the forcing becomes important again.

3.5 Summary

RANS calculations with various models, a LES calculation based on the log-law boundary condition and Wall-Modeled LES (WMLES) have been carried out on the contoured ramp. Since the inner layer was not resolved in the WMLES, significant computational savings have been achieved compared to a resolved LES. For the contoured ramp problem, a wall-resolved LES calculation (with $\Delta x^+ = 50$, $\Delta z^+ = 25$ and $y = \delta_{ref}/18$ at the boundary layer edge) would have required $3676\times 210 \times 696$ points. With WMLES, this calculation has been carried out with 1% of the grid nodes that would be used in a wall-resolved calculation.

The LES calculation based on the log-law boundary condition has to use a large spacing in the wall-normal direction, typically 5-10% of the boundary layer thickness. In a mild separation region, the height of the bubble is comparable to this distance which implies that the grid cannot resolve the separation region and this would result in poor prediction of the flow field in the recovery region. For flows with mild separation, the LES based on the log-law boundary condition should not be used.

The SA-RANS and the $k-\epsilon$ model predict a much shorter separation bubble

and a very weak back-flow. The SST model predicts the separation better than the other RANS models. The WMLES predict the recirculation region and the back-flow strength better than all the RANS models. The SA-RANS model and the SST model predict a much slower recovery than the experiments. The accurate prediction of the recovery by the $k-\epsilon$ model is due to its wrong prediction of a very weak back-flow. In the separation region, all the RANS calculations under-predict the Reynolds shear stress. The WMLES without the stochastic forcing over-predicts the Reynolds stresses in the separation region because of the artificially strong coherent streamwise motions in the attached boundary layer region. After separation, the instability of the detached shear layer results in the rapid generation of eddies (the energy content in the shear layer is excessive in this case). The convection of the resolved eddies results in a significant alleviation of the RANS/LES transition process in the recovery region; this results in a good prediction of the recovery. The addition of the stochastic forcing results in the removal of the shift in the log-law and accurate prediction of the skin-friction coefficient in the equilibrium region; it breaks up the streamwise coherent structures and results in better agreement of the predicted Reynolds stresses. The predicted mean velocity in the separation region are also in better agreement with experimental values.

Chapter 4

Flow past a two-dimensional bump

This chapter presents results from numerical simulations of flow past a two-dimensional bump. The bump geometry consists of two short concave regions connected fore and aft to a longer convex region. The flow experiences pressure gradients of both sign. Results from numerical simulations, performed at a momentum Reynolds number of 12170, are compared to the measured values from experiments of DeGraaff [33].

4.1 Introduction

When a turbulent boundary layer is subjected to pressure gradient and/or curvature, the scaling laws applicable in the zero-pressure gradient equilibrium region are no longer valid. In the next few sections, the effect of various perturbations of this type on the mean flow and the structure of the turbulence are discussed.

4.1.1 Curvature effects on turbulent boundary layer

Mean streamline curvature imposes a strain rate component, $\partial V/\partial x$, in addition to the strain rate $\partial U/\partial y$ present in wall-bounded flows, and has a profound influence on mean flow field and turbulent intensities. Heuristic arguments can be

used to predict the effect of concave and convex curvature on the turbulence [120]. In flows with streamline curvature, the centrifugal force is balanced by the normal pressure gradient. For flows over a convex surface, a particle that tends to move outward would be pushed back by the larger normal pressure gradient in the outer region (which balances the larger centrifugal force exerted by the particles having higher momentum); a particle that tends to move inward would be pushed outwards by its larger centrifugal force. Thus centrifugal force, then, acts to stabilize the fluctuations and reduces turbulence intensities on a convex surface. On a concave surface, the centrifugal force, due to the same mechanism, tends to amplify fluctuations and increases turbulence intensities. The skin-friction coefficient also increases on a concave surface, whereas it decreases on a convex surface. The curvature effect on turbulence is more significant in the outer region of the boundary layer where $\partial V/\partial x$ becomes comparable to $\partial U/\partial y$. One of the key parameters that determines the influence of the curvature on turbulence is δ/R, where δ is the boundary layer thickness and R is the radius of curvature; its influence on turbulence is found to be mild when it is around 0.01 and strong when it is larger than 0.05. Patel and Sotiropoulos [92] present a review of both experimental and modeling work on the curvature effects in turbulent boundary layers.

So and Mellor [119, 120, 121] present the first detailed turbulence measurements on flows over convex and concave surfaces. The parameter δ/R was around 0.08 in their experiment of flow over a convex surface. Their measurements show

that the mean velocity satisfies the law of the wall for a shorter distance than in a flat profile and it lies above the law of the wall in the outer region; the Reynolds shear stress decays to zero above $y/\delta = 0.5$, and the turbulence production is suppressed in the outer region. On the concave wall, they found that turbulence intensities increased substantially; they also found that the mean flow is three-dimensional (*i.e.,* the streamwise velocity had spanwise variation and the Reynolds shear stresses $< u'w' >$ and $< v'w' >$ were non-zero). Based on this observed spanwise variation, they postulate the existence of Taylor-Görtler vortices (a system of longitudinal vortices whose axis is aligned in the streamwise direction).

Ramaprian and Shivaprasad [100] studied the effect of mild concave and convex curvature ($\delta/R = 0.01$) on the structure of turbulent boundary layer. Their experiments show that the transport of turbulent kinetic energy from the wall to the outer region is suppressed on a convex region whereas it is enhanced on a concave area. This causes the observed increase of the extent of the log region over the concave surface and its decrease over the convex region. The spectral distribution of turbulent energy and Reynolds shear stress is shifted towards the high wavenumber in convex region which they attribute to the decrease in the strength of large eddies on a convex surface. On the concave surface, the spectral distributions of turbulent energy show that the large eddies are strengthened.

Smits *et al.* [118] studied the response of a turbulent boundary layer to strong but short regions of concave and convex surface curvature on two sides of a turning

pipe and the subsequent relaxation. The δ/R parameter was around 0.1 for the concave and 0.2 for the convex curvature and the flow experienced curvature effects for 12δ on the concave side and 6δ on the convex side. On the convex side, they observed a monotonic increase in turbulence in the relaxation region following its decay in the convex bend. In the relaxation region following the concave surface the turbulence intensity, which had increased on the concave bend, decreased initially to a value below the value at the entry in the relaxation region, and then recovered; the spanwise variations in the flow field, introduced by longitudinal vortices on the concave bend, decayed slowly in the relaxation region.

Muck *et al.* [87] and Hoffmann *et al.* [52] studied the response of the turbulent boundary layer on convex and concave surface with mild curvature ($\delta/R = 0.01 - 0.02$). They showed that the turbulent boundary layer responds to the application of convex curvature rapidly by merely attenuating the pre-existing turbulence. On the other hand, the turbulent boundary layer responds rather slowly to the application of concave curvature, and is marked by significant changes in turbulence structure and the generation of longitudinal vortices.

Gillis and Johnston [46] performed experiments on a convex wall with strong curvature ($\delta/R = 0.05$ and 0.1) and presented results in the convex region and the recovery regions. They show that the Reynolds shear stress normalized by the local wall-stress in the convex region, for the two cases they studied and also the strong curvature case of So and Mellor [120], collapses when plotted against n/R. They

conjecture that large-eddies from the upstream boundary layer are destroyed in the convex region when the curvature parameter is strong (*i.e.*, $\delta/R > 0.04$) and this causes the shear-stress values to asymptote to a profile independent of the initial condition.

Barlow and Johnston [10] performed experiments on a concave surface to verify the existence of longitudinal vortices and to study the turbulence structure on a concave wall. Their flow visualization showed that stable longitudinal vortices over a significant streamwise extent existed only when the upstream boundary layer had spanwise non-uniformities; otherwise, the large-scale structures with streamwise vorticity wander, merge, separate, appear and disappear without producing any significant spanwise variation in the mean flow field.

Moser and Moin [86] performed DNS of a flow in a curved channel to study numerically the effects of convex and concave curvature on turbulence. The Reynolds number based on averaged friction velocity on the convex and concave walls is 168, and the curvature parameter based on the radius at the centerline and the channel-half width is 0.0127. Their numerical simulation also showed many of the behaviors previously measured in the experiments: on the convex side, the mean velocity profile lies above the log-law whereas on the concave side it lies below it; approximately half of the differences in wall-shear stress and the Reynolds shear stress between the concave and convex surface is due to Taylor-Görtler vortices; the budget of the Reynolds shear stress normalized by the local wall coordinates shows a large differ-

ence between the concave and the convex side: the velocity-pressure-gradient term is 20% greater on the concave side, and the turbulent diffusion is 40% higher on the concave side.

Lund and Moin [74] performed LES of a spatially evolving boundary layer on a concave surface at a momentum Reynolds number of 1300. The significant finding from their study is that Taylor-Görtler vortices appear on the concave surface only if the inflow has strong streamwise coherence, otherwise, a weaker secondary flow pattern appears. This is in accordance with the experiments of Barlow and Johnston [10]. Their numerical results agrees better with the experimentally measured values when Taylor-Görtler vortices are created using the inflow with strong streamwise coherence.

4.1.2 Pressure gradient effects on turbulent boundary layer

The pressure gradient effects on the boundary layer are immediately felt in the inner layer since the pressure gradient is balanced by the viscous force there; this is unlike curvature, which affects the outer region first. Adverse pressure gradient application may lead to flow separation, while a strong favorable pressure gradient may lead to relaminarization or reverse transition of turbulent flows. The following non-dimensional parameters are used to quantify the pressure gradient magnitude

$$K = \frac{\nu}{U_\infty^2}\frac{dU_\infty}{dx} \tag{4.1}$$

$$\Delta_p = \frac{\nu}{u_\tau^3}\frac{dP}{dx} \tag{4.2}$$

Patel [93] shows that, in the presence of adverse pressure gradient, the extent of the log-law region is decreased and the value of the wake component of the mean velocity increases. At high values of adverse pressure gradient there is no region where the log-law is satisfied. In the presence of favorable pressure gradient, experiments by Patel [93] and Patel *et al.* [94] show that the wake component of the mean velocity decreases initially, and the mean velocity profile lies below the log-law; a strong favorable pressure gradient causes the slope of mean velocity profile to decrease and moves it above the log-law by increasing the intercept.

Dengel and Fernholz [34] investigated the response of the turbulent boundary layer to a strong adverse pressure gradient that causes incipient separation *i.e.,* minimum skin-friction coefficient reaches zero. Their measurements show that the maximum value of the Reynolds stresses increases with downstream distance and also their peak location moves away from the wall. Aubertine and Eaton [5] performed experiments to study the response of turbulent boundary layer to mild adverse pressure gradient and show different behavior in the streamwise variation of Reynolds stress. The streamwise Reynolds stress does not increase significantly and its peak location also does not move, but it develops a plateau behavior in the outer layer with elevated stress values; the wall-normal Reynolds stress increases slightly in the adverse pressure gradient.

Fernholz and Warnack [41] performed experiments to study the response of turbulent boundary layer to favorable pressure gradient whose maximum K value

are 2×10^{-6} and 1.53×10^{-6}. They show that in the near wall region the streamwise Reynolds stress increases in the streamwise direction; but the streamwise Reynolds stress normalized with the local friction velocity, however, initially decays due to faster increase in the skin-friction and then increases to a value larger than the upstream zero-pressure-gradient peak; later, it decreases and stabilizes to the upstream zero-pressure-gradient value. The streamwise Reynolds stress decreases in the region between $0.2 < y/\delta < 0.6$ and stays constant above $y/\delta > 0.6$. The Reynolds shear stress also shows similar behavior. The Reynolds shear stress increases in the near wall region but remains constant for $y > 0.55$. When normalized by the local friction velocity, however, the Reynolds shear stress decreases rapidly initially and slowly returns to its upstream value.

4.1.3 Multiple perturbation effects on turbulent boundary layer

Even if the response of turbulent boundary layer to individual perturbations is known, the effects of simultaneous or sequential applications of multiple perturbations cannot be constructed as the sum of their individual effects, due to non-linear character of the Navier-Stokes equation. Smits and Wood [117] present a review of the effects of multiple perturbations on the boundary layer.

Tsuji and Morikawa [132] performed one of the first experiments that showed the asymmetric response of turbulent boundary layers to a sequential application of alternating signs of pressure gradient (adverse, favorable, adverse and favorable).

Flow properties do not return to the upstream zero pressure gradient values after the application of first adverse and favorable pressure gradient, indicating the asymmetric response. In the second adverse pressure region following the first adverse and favorable pressure gradient, an 'internal boundary layer' develops which they attribute to the sudden change in the shear stress gradient at the wall. The internal boundary layer is a newly developing boundary layer within the previous boundary layer. The boundary between the internal boundary layer and the previous boundary layer can be discerned from the location of local minimum point or the 'knee point' in the Reynolds shear stress profile. The growth rate of the internal boundary layer can be determined from the outward movement of the knee point with the downstream distance.

Baskaran *et al.* [11, 12] performed experiments on a curved hill to study the boundary layer response to curvature and pressure gradient changes. Their experimental configuration is similar to the two-dimensional bump studied in this chapter but the mean flow separates on the back of the hill in their case whereas there is no mean flow separation in the two-dimensional bump studied here. The curved hill has a short concave region at the leading edge and a prolonged convex region following the concave region. They performed two sets of experiments. In the first case, they had a flat plate region preceding the leading edge of this geometry; a developing boundary from the flat plate region encounters the leading edge of the geometry, and this configuration resembles the flow past a curved hill that occurs in atmospheric

applications. In the second case, they attached two convex regions (of the same curvature as the one used in the curved hill experiment) to create a symmetrical wing. The flow is subjected to an adverse pressure gradient near the leading edge of the curved hill and then to favorable one on the front half and then to an adverse one on the lee side. In the curved hill experiment, they observe an internal layer development in the convex region following the concave region. The internal boundary layer development can be seen from the outward movement of the knee point in the Reynolds shear stress profile with downstream distance. Reynolds stresses increase below the knee point with downstream distance, whereas, due to prolonged convex streamline curvature, they decrease above the knee point with downstream distance. Their comparison of the internal boundary layer on the curved hill with the boundary layer on the wing configuration shows that the integral length scale and the growth rate of both boundary layers are similar, and the mean velocity profile and the Reynolds stresses within both boundary layers also show the same streamwise development. They conjecture that the internal layer grows as an independent boundary layer beneath the turbulent free-shear layer and attribute its development to the change in curvature at the junction between the concave and convex region of the curved hill. They define the following quantity which they call as wall curvature perturbation parameter.

$$\Delta k^* = (\frac{1}{R_1} - \frac{1}{R_2})\frac{\nu}{u_\tau} \tag{4.3}$$

By analyzing data from previous experiments, they conjecture that the wall-curvature

perturbation parameter has to be larger than 3.37×10^{-5} for the generation of internal boundary layer.

Bandyopadhyay and Ahmed [9] studied the response of the turbulent boundary layer on two opposite walls of an S shaped channel. Wall A had a flat-concave-convex-flat curvature changes with adverse, favorable and adverse pressure gradients near the curvature change locations and zero pressure gradient everywhere else. Wall B had a flat-convex-concave-flat curvature changes with favorable, adverse and favorable pressure gradients near the curvature change locations and zero pressure gradient everywhere else. The asymmetric response of the boundary layer can be seen from the lower net drag on the wall A (by 12%) than that on the wall B. Silva Lopes *et al.* [110] studied this flow numerically at a lower Reynolds number.

4.2 Problem formulation

The objective of the work in this chapter is to test the performance of WMLES and other RANS models for flows that experience pressure gradient effects and curvature effects. The two-dimensional bump (see the sketch in figure 4.1) used in this study is formed by three tangential circular arcs. The bump has a short concave region near the leading edge which is followed by a longer convex region and then by a short concave region near the trailing edge. Experiments on this geometry were conducted by Webster *et al.* [137] and DeGraaff [33] and the results for the Reynolds number simulated in the present study are reported in [33].

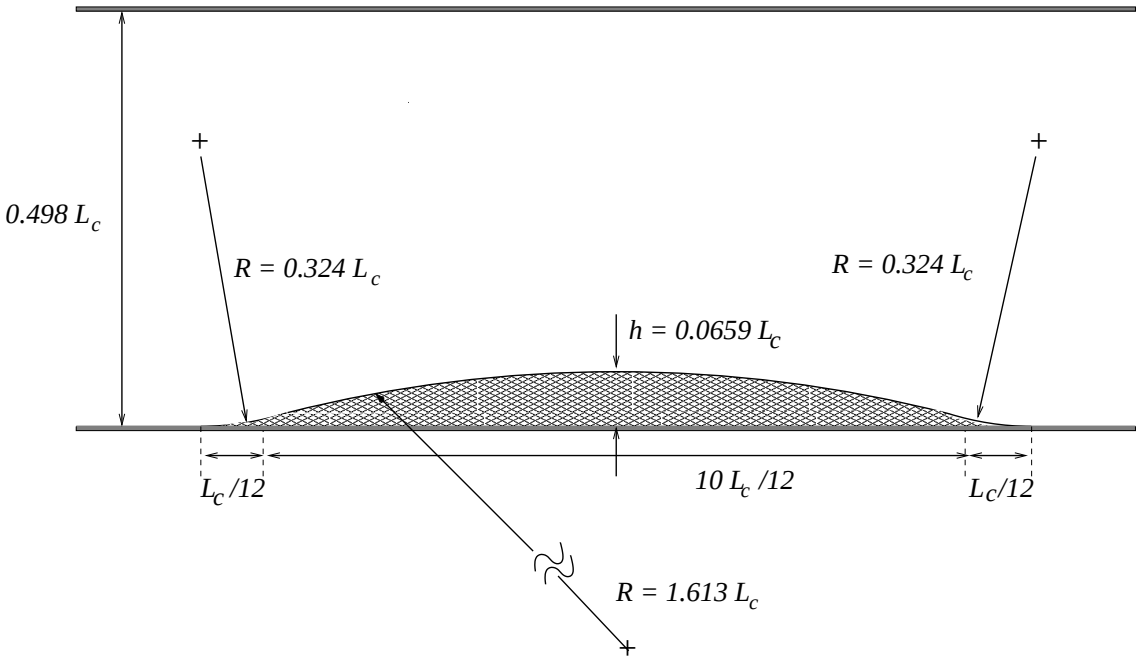

Figure 4.1: Flow configuration for the two-dimensional bump calculation

The momentum Reynolds number Re_θ at the reference location, which is located one-half chord length upstream of the leading edge of the bump, is 12170. In the simulation, all the lengths are non-dimensionalized by the chord length ($L_c = 305$ mm) of the bump. The inlet of the simulation domain is located at the reference location and the streamline curvature effect is not felt by the boundary layer at the inlet. The boundary layer thickness at the inlet is $0.09718L_c$. The top wall is located $0.498L_c$ above the bottom wall at the inlet and the two boundary layers at the top and bottom wall are separated by a potential core whose height is approximately two boundary layer thickness. The maximum height of the bump is $0.0659L_c$ and the boundary layer thickness at the inlet is 1.5 times larger than the maximum height of the bump. The curvature parameter for the concave region is 0.3 and for the convex

region is 0.06. The simulation domain extends two chord lengths downstream of the trailing edge and then by a buffer region for the outflow.

As the turbulent boundary layer approaches the concave region of the bump, it experiences an adverse pressure gradient because of the concave streamline curvature, followed by a favorable one over the first half of the bump. Beyond the summit of the bump, the flow expands and experiences an adverse pressure gradient, which is not strong enough to cause mean-flow separation, although, the flow separates intermittently [139]. On the concave region near the trailing edge of the bump, the concave curvature effect causes a favorable pressure gradient. The flow recovers downstream of the trailing edge of the bump.

RANS calculations were performed with the SA model, the $k-\epsilon$ model, the SST model, and the Reynolds stress transport model. Large-eddy simulation was performed with Lagrangian dynamic model and log-law boundary condition. WMLES simulations were performed with and without the application of stochastic forcing. Results of the $k-\epsilon$ model were very similar to those obtained with the SA-RANS model, and will not be shown here.

The WMLES simulation domain was $3\delta_{ref}$ long in the spanwise direction and used a grid with $538\times150\times36$ nodes in the streamwise, wall-normal and spanwise directions, respectively (see figure 4.2). The grid was uniform in the spanwise direction and stretched in the streamwise and wall-normal directions. There were 12 points per δ_{ref} in the spanwise and streamwise directions (except near the out-

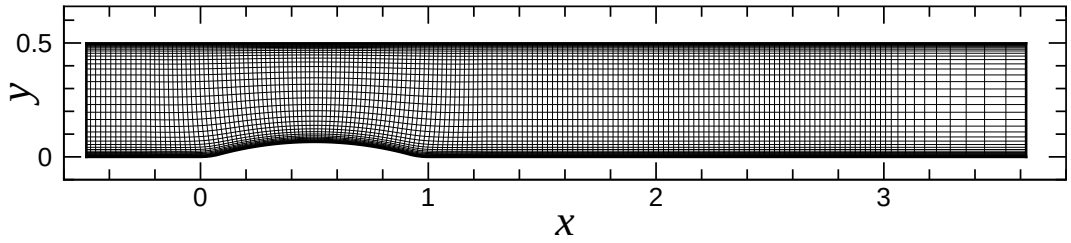

Figure 4.2: Grid used for the two-dimensional bump calculation. Every third point is shown.

flow). In the wall-normal direction the first point was located at $y^+ = 1$ and the grid was stretched so that near the boundary-layer edge there were 12 points per δ_{ref}, resulting in cubic grid cells in the outer region. The LES calculation with log-law boundary condition was performed on the same domain but with a grid that had 538×72×36 nodes in the streamwise, wall-normal and spanwise directions respectively. The RANS calculation used WMLES grid but with only 1 point in the spanwise direction. Results from the RANS simulations and LES with log-law are discussed first in the next section and WMLES results are discussed in the following section.

4.3 RANS and LES results

Figure 4.3 shows the skin friction and pressure coefficients, which are defined as

$$C_f = \frac{\tau_w}{\rho U_\infty^2/2}; \qquad C_p = \frac{p - p_{ref}}{\rho U_{ref}^2/2}, \tag{4.4}$$

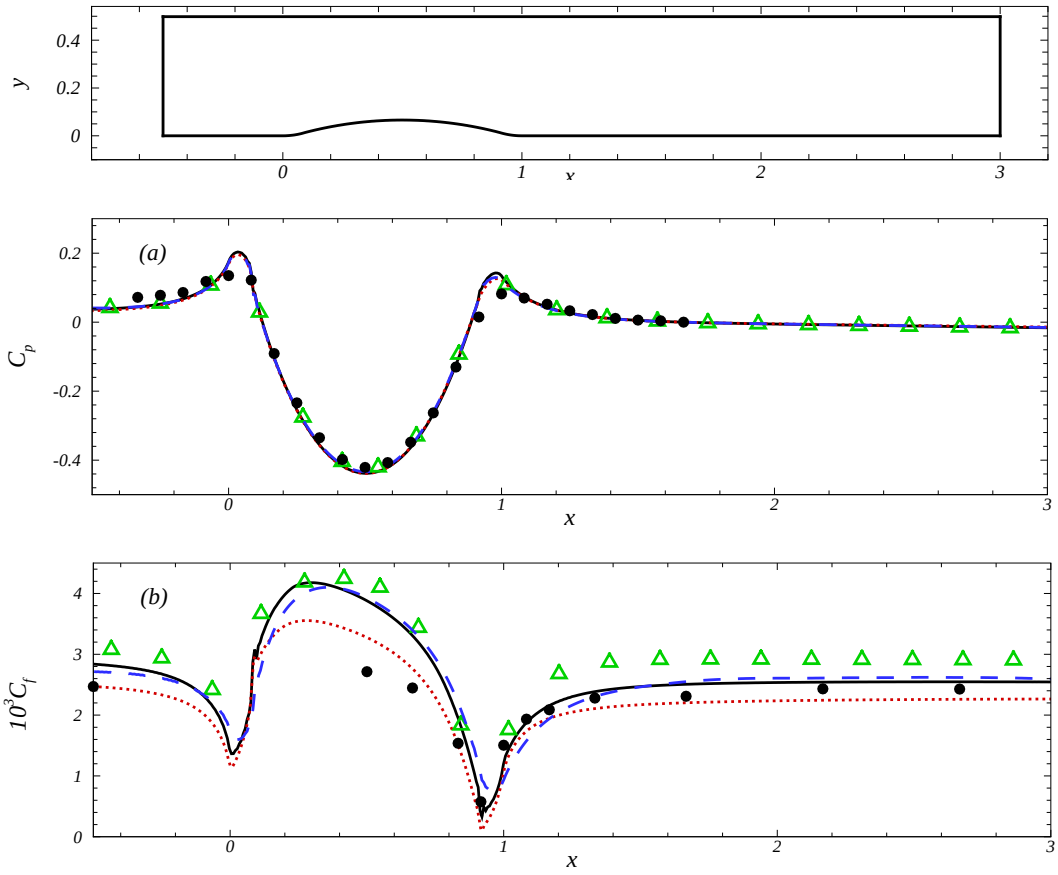

Figure 4.3: Profiles of (a) pressure coefficient and (b) skin-friction coefficient. ——— SA-RANS; ------ SST model; △ Reynolds stress transport model; – – – Log law; • Experiments.

where U_∞ is the velocity at the edge of the boundary layer at the current location, p_{ref} is the wall pressure at $x = 1.667$ and U_{ref} is the velocity at the edge of the boundary layer at $x = 1.667$. The wall-pressure coefficient was measured in the experiments for a lower Reynolds number case with $Re_\theta = 3120$ at the reference section. Also in the experiments, the skin-friction was measured for $Re_\theta = 3120$. For the high Reynolds number case, DeGraaff [33] estimated the wall shear-stress by assuming that the ratio of skin friction at any position to the skin friction at the reference position is independent of Reynolds number, an assumption whose validity is unknown. Also at the reference location, he estimated the skin friction by a logarithmic law fit.

In the flat-plate region ahead of the bump, the SST model predicts the skin-friction coefficient accurately whereas all the other calculation over-predict it. All the calculations show the expected deceleration of the flow ahead of the bump due to the mild adverse pressure gradient. In the adverse pressure gradient region after the summit of the bump, all the calculations predict the deceleration reasonably well. In the recovery region, the skin-friction coefficient predicted by all the models return to their upstream values.

Figures 4.4 and 4.5 show the mean horizontal velocity profiles at select locations. In these figures, the mean horizontal velocity is normalized by the local free stream velocity. Experimental data is available downstream of the summit of the bump and at the reference location. At the leading edge of the bump, because of

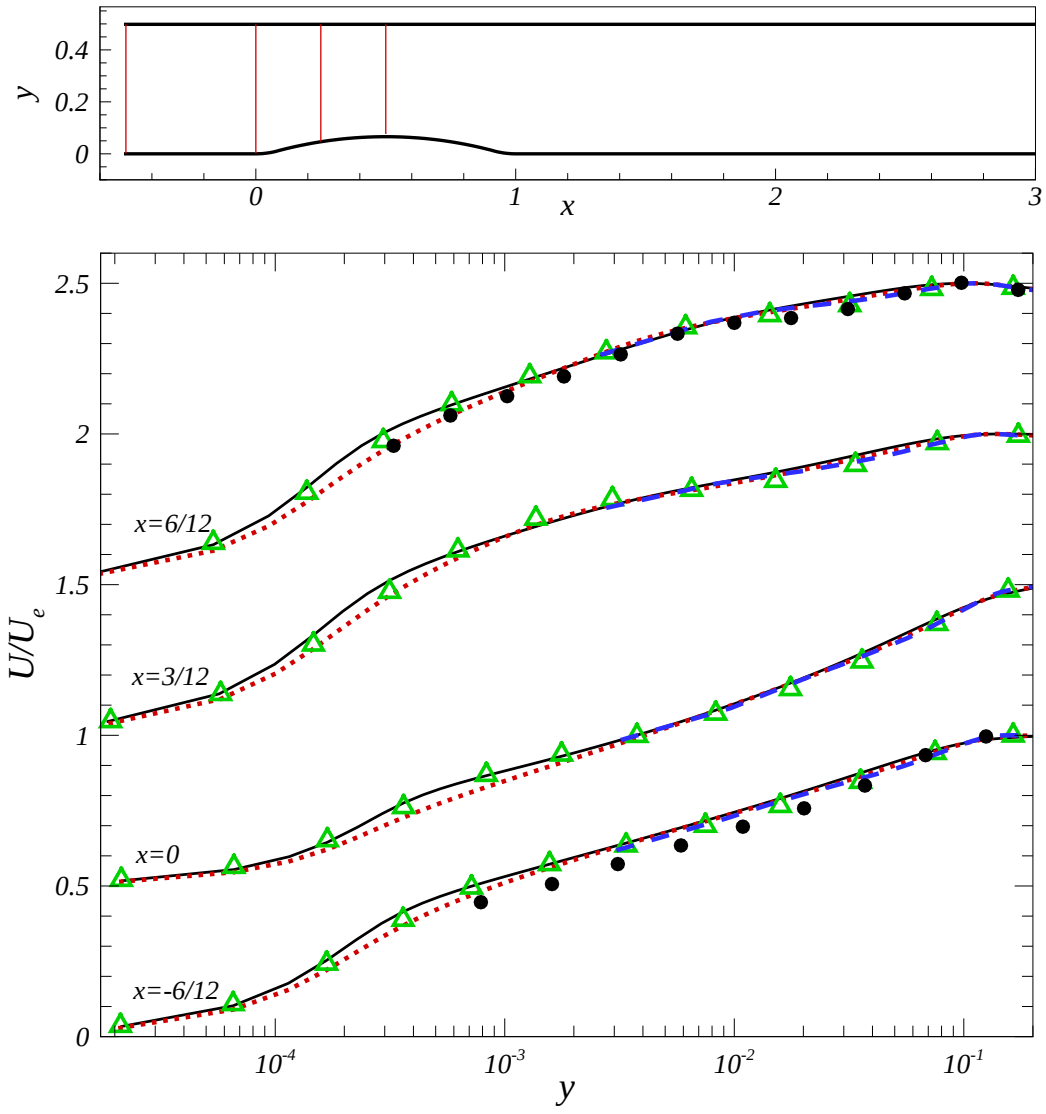

Figure 4.4: Mean horizontal velocity profile. ——— SA-RANS; ····· SST model; △ Reynolds stress transport model; – – – Log law; • Experiments.

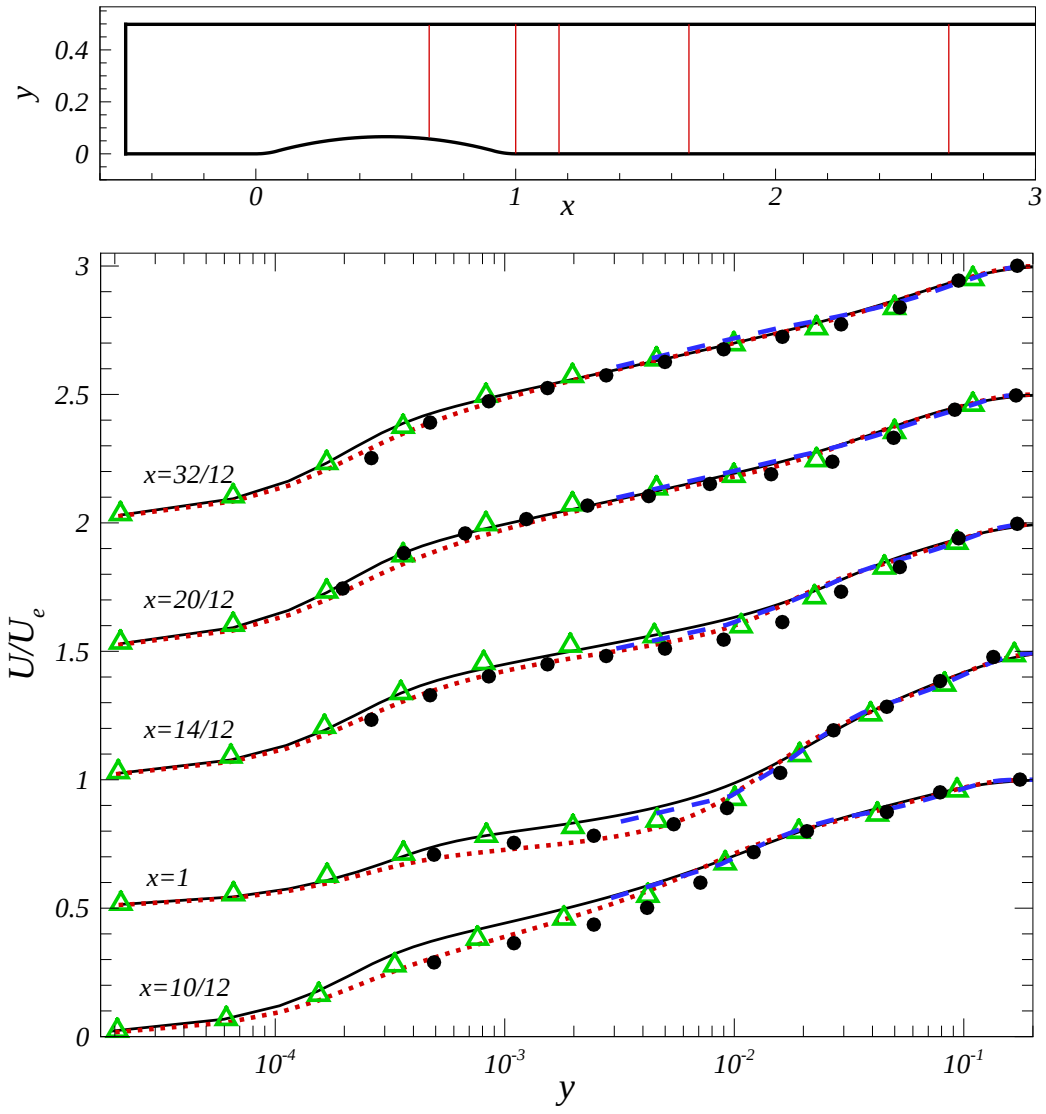

Figure 4.5: Mean horizontal velocity profile. ——— SA-RANS; ····· SST model; △ Reynolds stress transport model; – – – Log law; • Experiments.

the adverse pressure gradient caused by the concave streamline curvature, the flow slows down in the near wall region. The favorable pressure gradient present till the summit of the bump, created due to the constriction of the geometry, accelerates the flow. At the summit of the bump, all the calculations predict the mean horizontal velocity accurately. In the adverse pressure gradient region after the summit of the bump, the SST model predicts the deceleration of the flow reasonably well whereas the SA-RANS and the Reynolds stress transport model over-predict the velocity in the near wall region. In the recovery region, all the calculations predict the return to equilibrium of the mean horizontal velocity accurately.

Figures 4.6 and 4.7 show the Reynolds shear stress at selected locations. The Reynolds shear stress is expected to increase near the leading edge of the bump due to the adverse pressure gradient and also in the concave region of the bump due to curvature effects. All the models show this trend at $x = 0$. An internal layer is triggered at $x = 1/12$ due to curvature discontinuity and its growth should be visible from the outward movement of the knee point in the Reynolds shear stress. At $x = 3/12$, the SST model and the SA-RANS model predict the knee point whereas the Reynolds stress transport model and the LES with log-law boundary condition do not predict it. The fact that Reynolds stress transport model does not predict the knee point is surprising since better accuracy is expected with this model in flows with curvature effects. Since the LES with log-law boundary condition does not resolve the near wall region, it cannot predict the internal-layer growth from

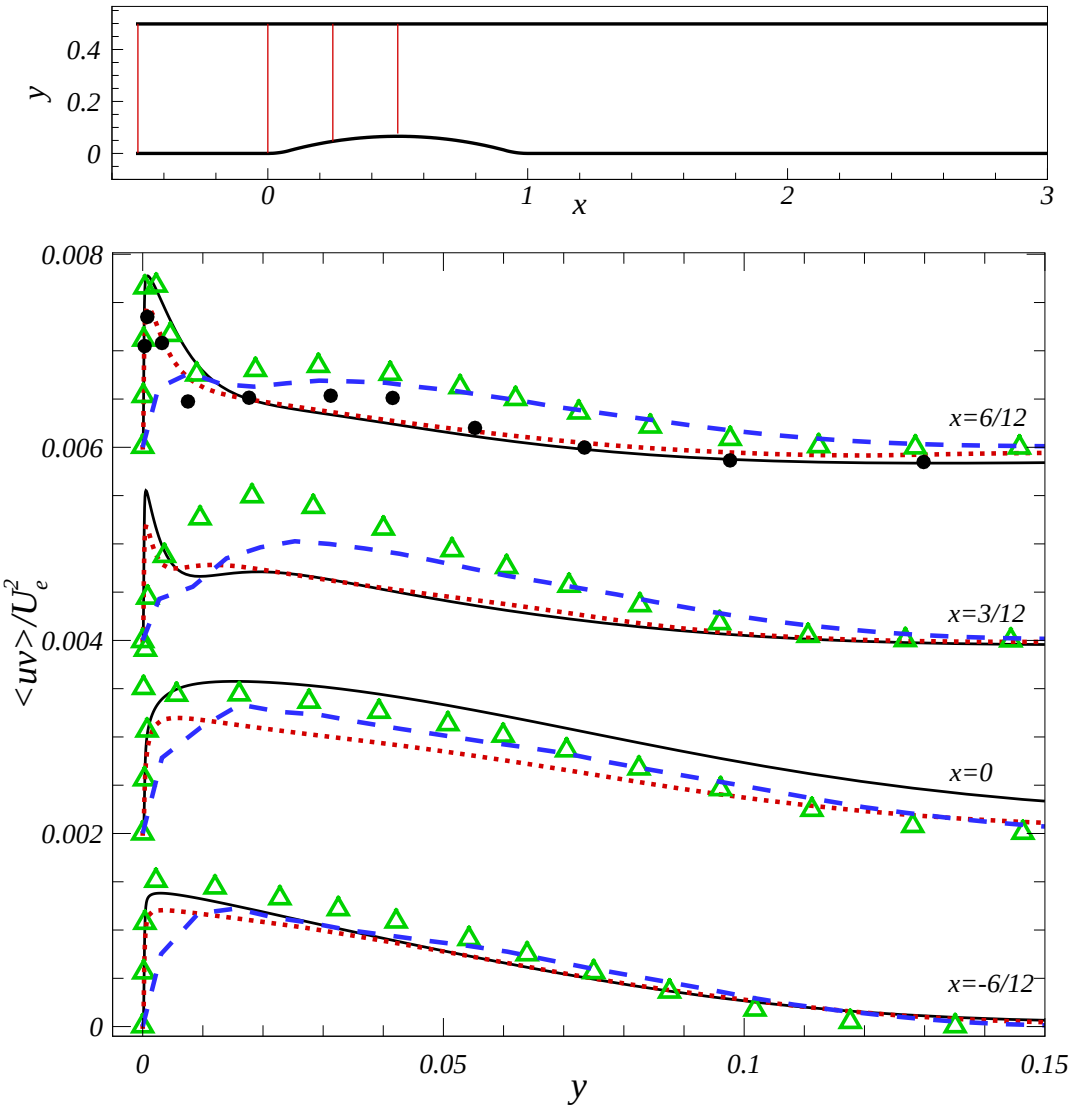

Figure 4.6: Total (resolved + modeled) Reynolds shear stress profile. —— SA-RANS; ····· SST model; △ Reynolds stress transport model; – – – Log law; • Experiments.

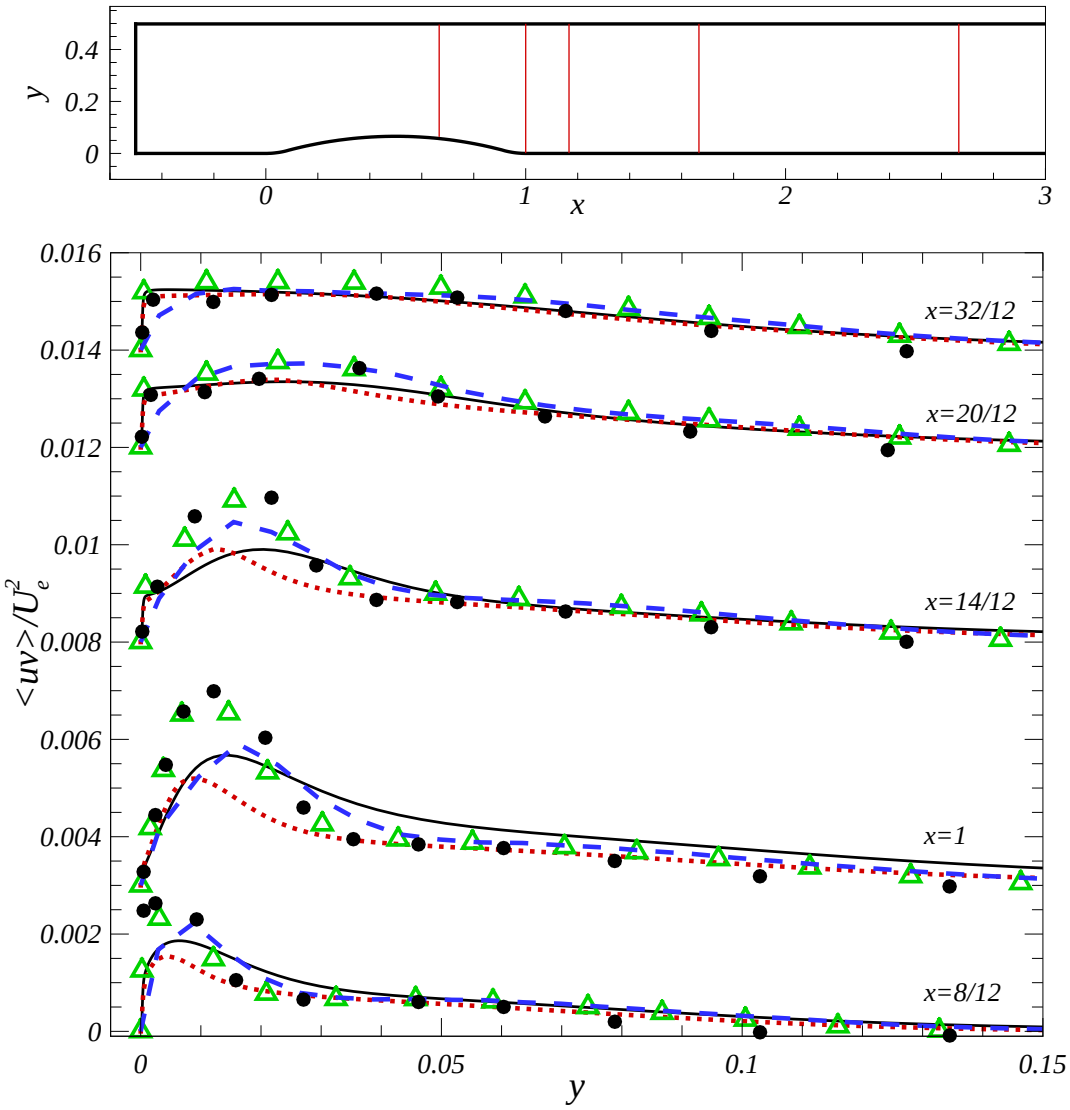

Figure 4.7: Total (resolved + modeled) Reynolds shear stress profile. —— SA-RANS; ····· SST model; △ Reynolds stress transport model; – – – Log law; • Experiments.

the wall. In the outer region, Reynolds shear stress decreases in the first half of the bump due to convex curvature and favorable pressure gradient effects. At the summit of the bump, all the RANS models predict the increase in the peak of the Reynolds shear stress due to the outward growth of the internal layer; the SST model predicts the peak value accurately whereas the Reynolds stress transport model and the SA-RANS model over-predict it. After the summit of the bump, the Reynolds shear stress is expected to increase due to the adverse pressure gradient effects. The Reynolds stress transport model predicts it accurately whereas the SA-RANS and the SST model under-predict the Reynolds shear stress peak by as much as 30%. In the recovery region, the prediction of the Reynolds shear stress by the Reynolds stress transport is excellent. At the trailing edge, the SST model and the SA-RANS model under-predict the Reynolds shear stress by 40%; their prediction improves in the recovery region.

Figures 4.8 and 4.9 show the rms of u-velocity fluctuations at selected locations. The SA-RANS model and the SST model, being one equation and two equation model, do not solve for the individual Reynolds stress components and cannot predict this quantity. Prediction by the Reynolds stress transport model and the LES with log-law boundary condition are in reasonable agreement with the experimental values everywhere.

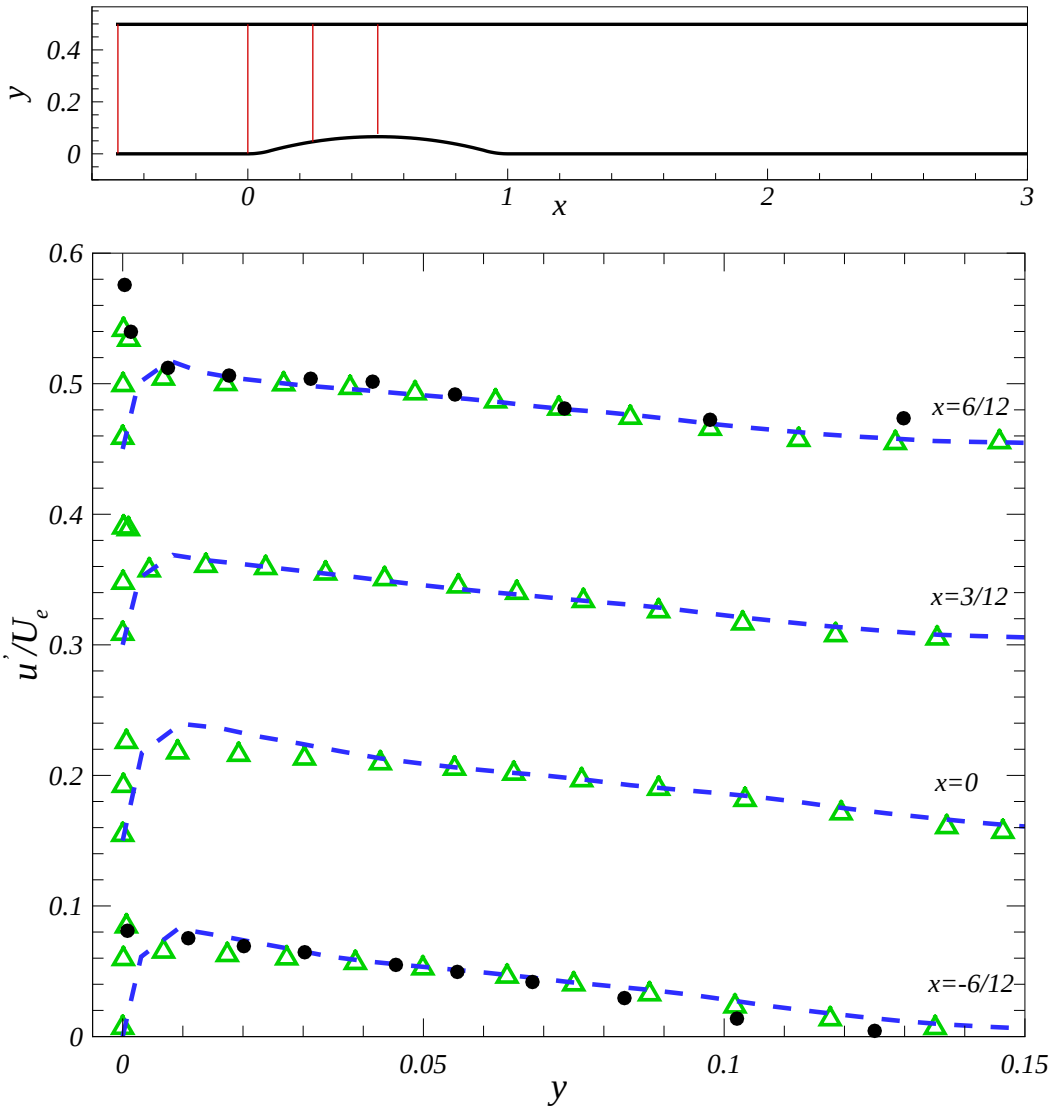

Figure 4.8: RMS of u velocity fluctuations. △ Reynolds stress transport model; — — Log law; • Experiments.

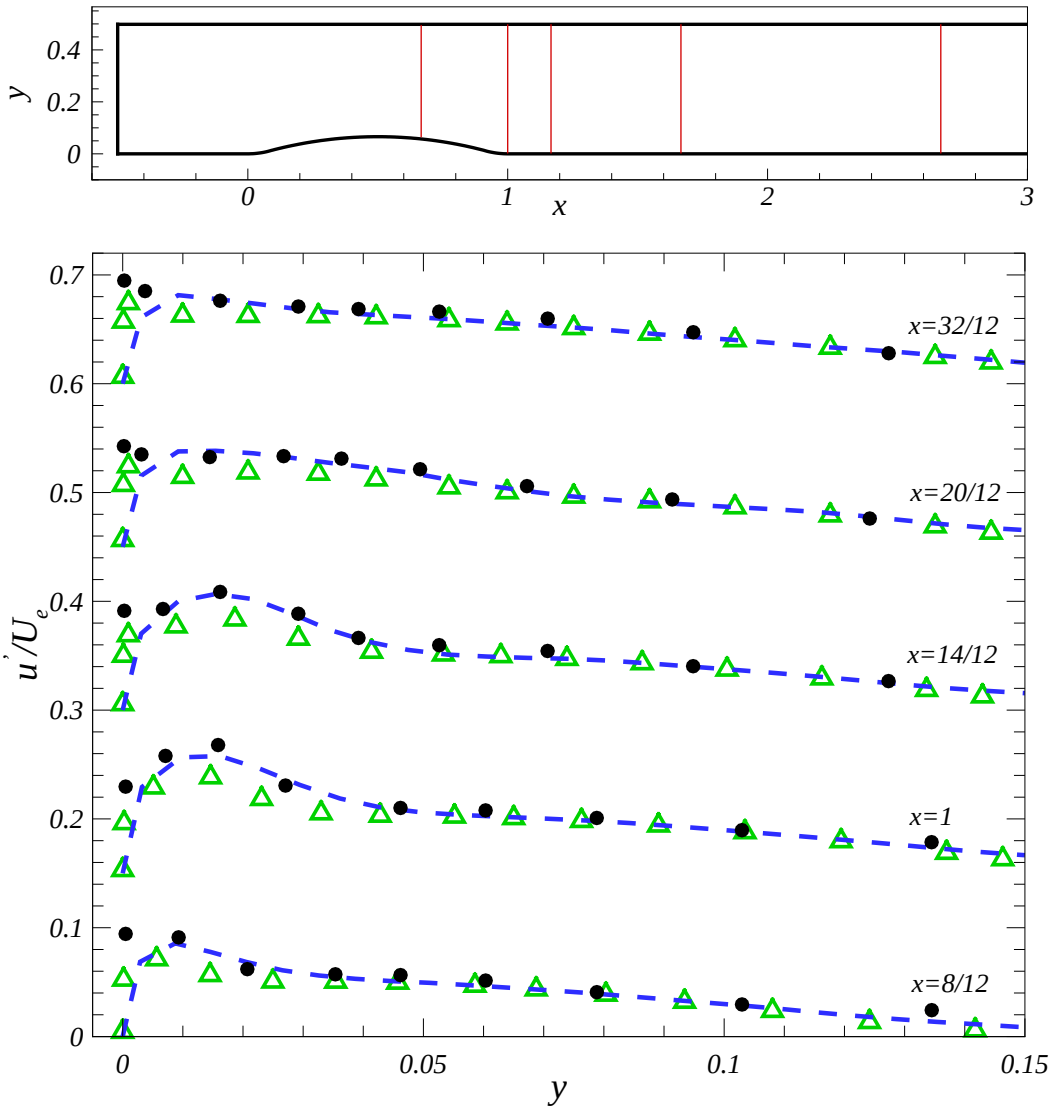

Figure 4.9: RMS of u velocity fluctuations. △ Reynolds stress transport model; — — Log law; • Experiments.

4.4 WMLES results

In this section, results from two WMLES simulations (with and without the stochastic forcing) are compared to measured values from the experiment. In the flat-plate region ahead of the bump, the WMLES without the stochastic forcing under-predicts the skin-friction by 10% ; the addition of the stochastic forcing increases the value of the predicted of the skin-friction. Near the leading edge, all the calculations show the expected deceleration due to the mild adverse pressure gradient. In the first half of the bump, the skin-friction increase due to the favorable pressure gradient. All the calculations predict the skin-friction reasonably well in the adverse pressure gradient region and the recovery region.

Figures 4.11 and 4.12 show the mean horizontal velocity profiles at select locations. Mean velocity prediction by both the WMLES show excellent agreement with the measured values from experiments everywhere. LES with the log-law boundary condition does not predict the deceleration of the mean velocity in the near wall region accurately; in the recovery region, its prediction is improved. Figures 4.13 and 4.14 show the Reynolds shear stress at select locations. At the summit of the bump, both WMLES calculations predict the Reynolds shear stress accurately. In the adverse pressure gradient region after the summit of the bump, the WMLES without the stochastic forcing over-predicts the Reynolds shear stress but the addition of the stochastic forcing results in lower Reynolds shear stress and better agreement with the experiments. In the recovery region, the WMLES without the

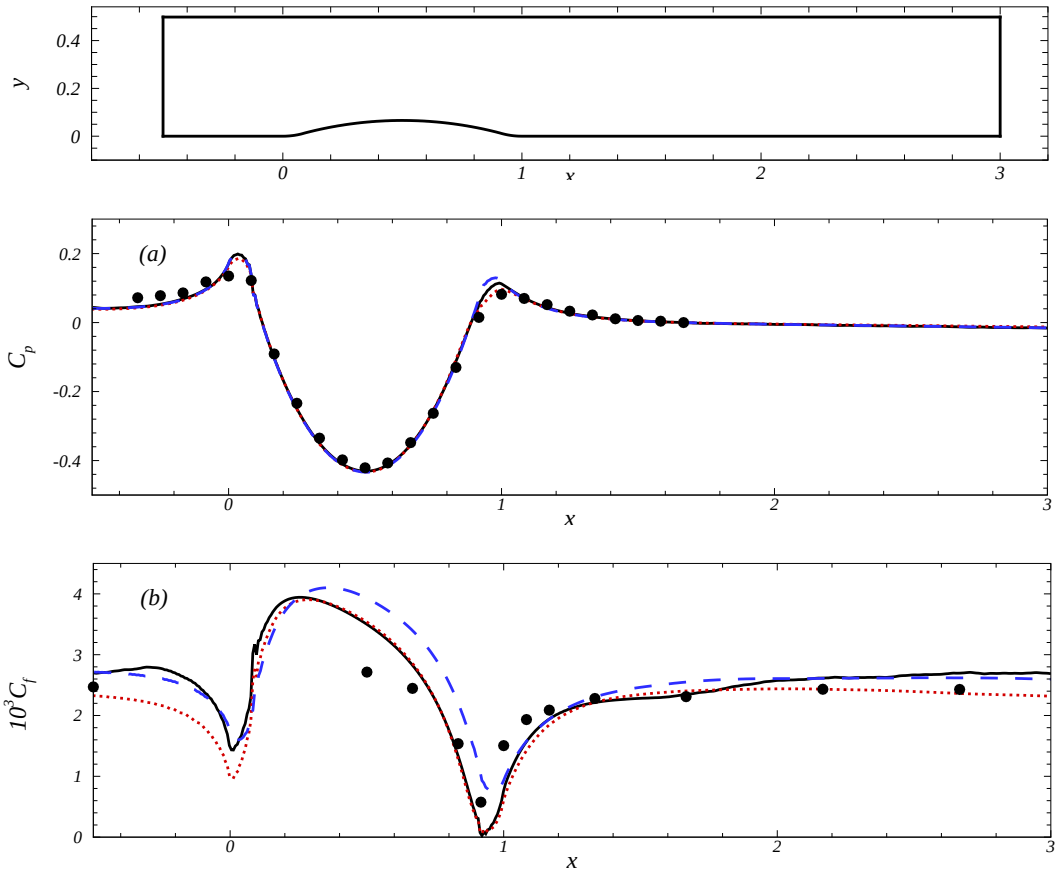

Figure 4.10: Profiles of (a) pressure coefficient and (b) skin-friction coefficient. Log law; WMLES; WMLES with stochastic forcing; • Experiments.

stochastic forcing over-predicts the Reynolds shear stress possibly due to slow decay of eddies generated in the upstream adverse pressure gradient region. Figure 4.15 and 4.16 show the rms of the fluctuations of u-component of the velocity at select locations. It shows the same trend as the Reynolds shear stress; the WMLES without stochastic forcing over-predicts the rms of the fluctuations by as much as 40% in the recovery region; the addition of the stochastic forcing has resulted in better agreement with the experimental values.

In contrast to the ramp problem, the WMLES without the stochastic forcing gives reasonable prediction of the flow field. This can be attributed to eddies generated in the concave region and will be explained further. Figure 4.17 shows the iso-surfaces of $Q = 18$ and the contours of horizontal velocity fluctuations in a plane parallel to the wall for the WMLES without the stochastic forcing. As expected, there is very little eddy content in the upstream boundary layer. As the flow goes over the concave region, the instabilities due to the concave curvature generates eddies near the leading edge. These eddies support the resolved shear stress in the RANS/LES transition region and this results in improved prediction of the mean horizontal velocity in the downstream convex region. Similar to the trend seen in the ramp, the adverse pressure gradient and possibly the intermittent separation that occurs after the summit of the bump cause the eddies to become larger and energetic. The eddies present in the recovery region are much more energetic compared to the eddies present in the upstream boundary layer and they cause the

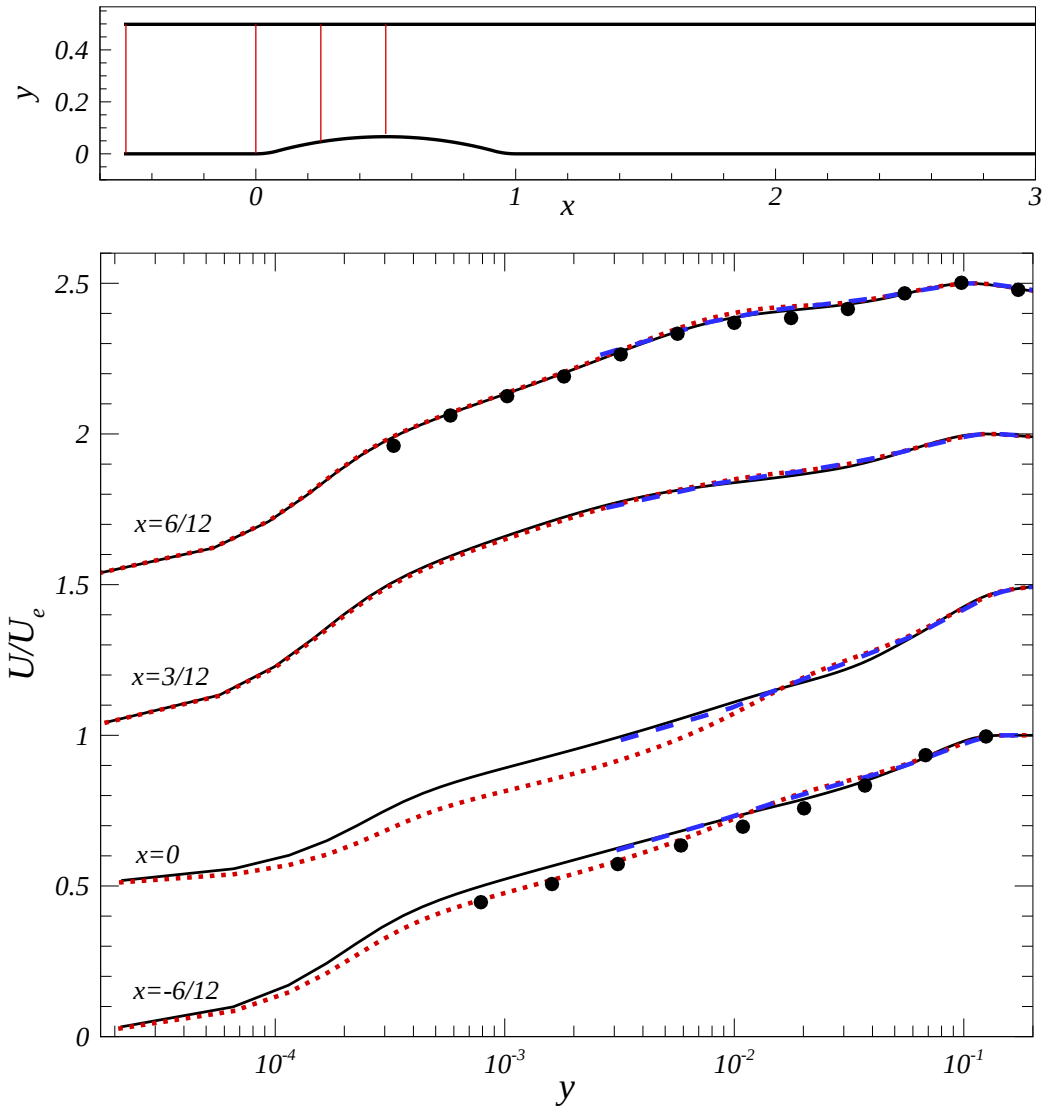

Figure 4.11: Mean horizontal velocity profile. Log law; WMLES; WMLES with stochastic forcing; • Experiments.

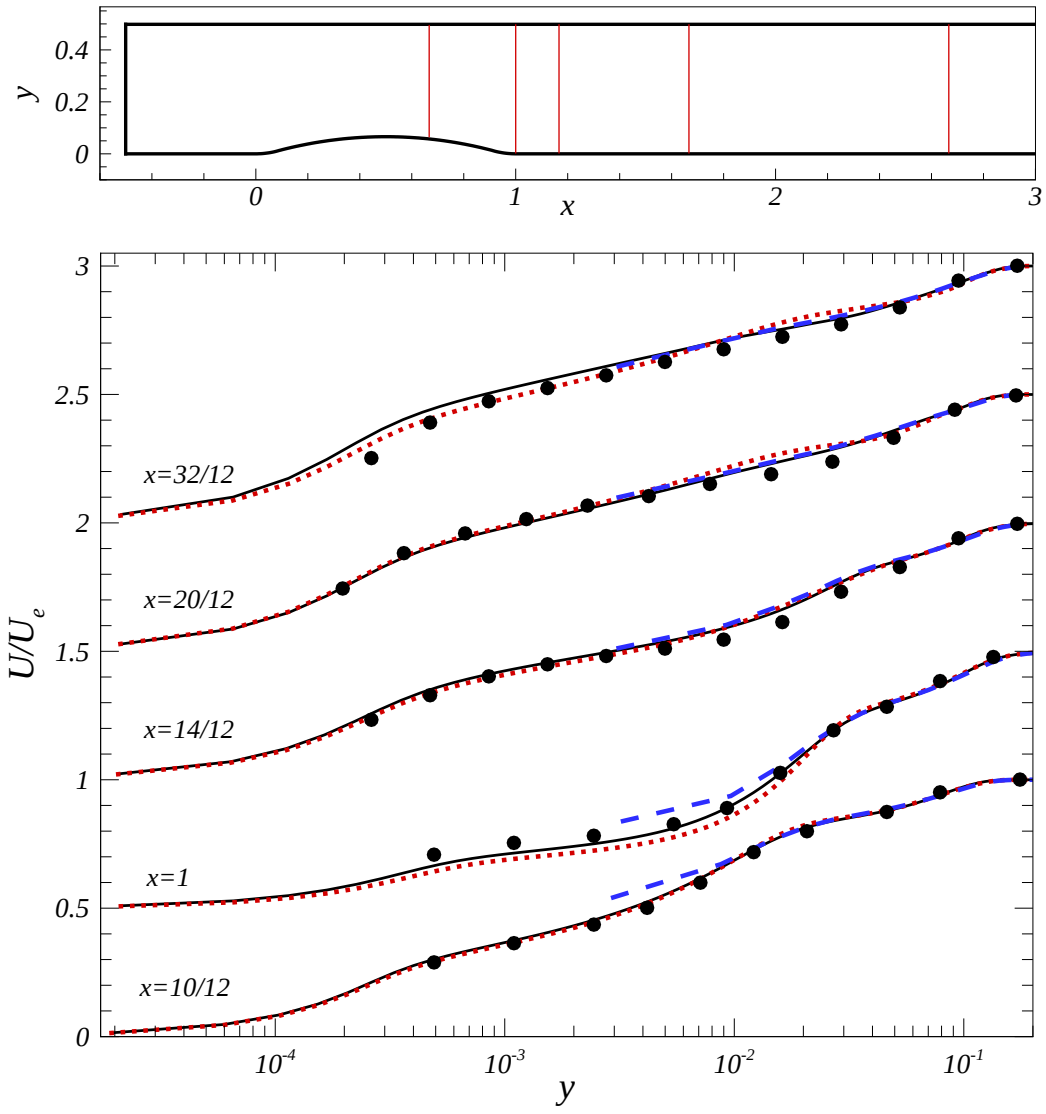

Figure 4.12: Mean horizontal velocity profile. Log law; WMLES; WMLES with stochastic forcing; • Experiments.

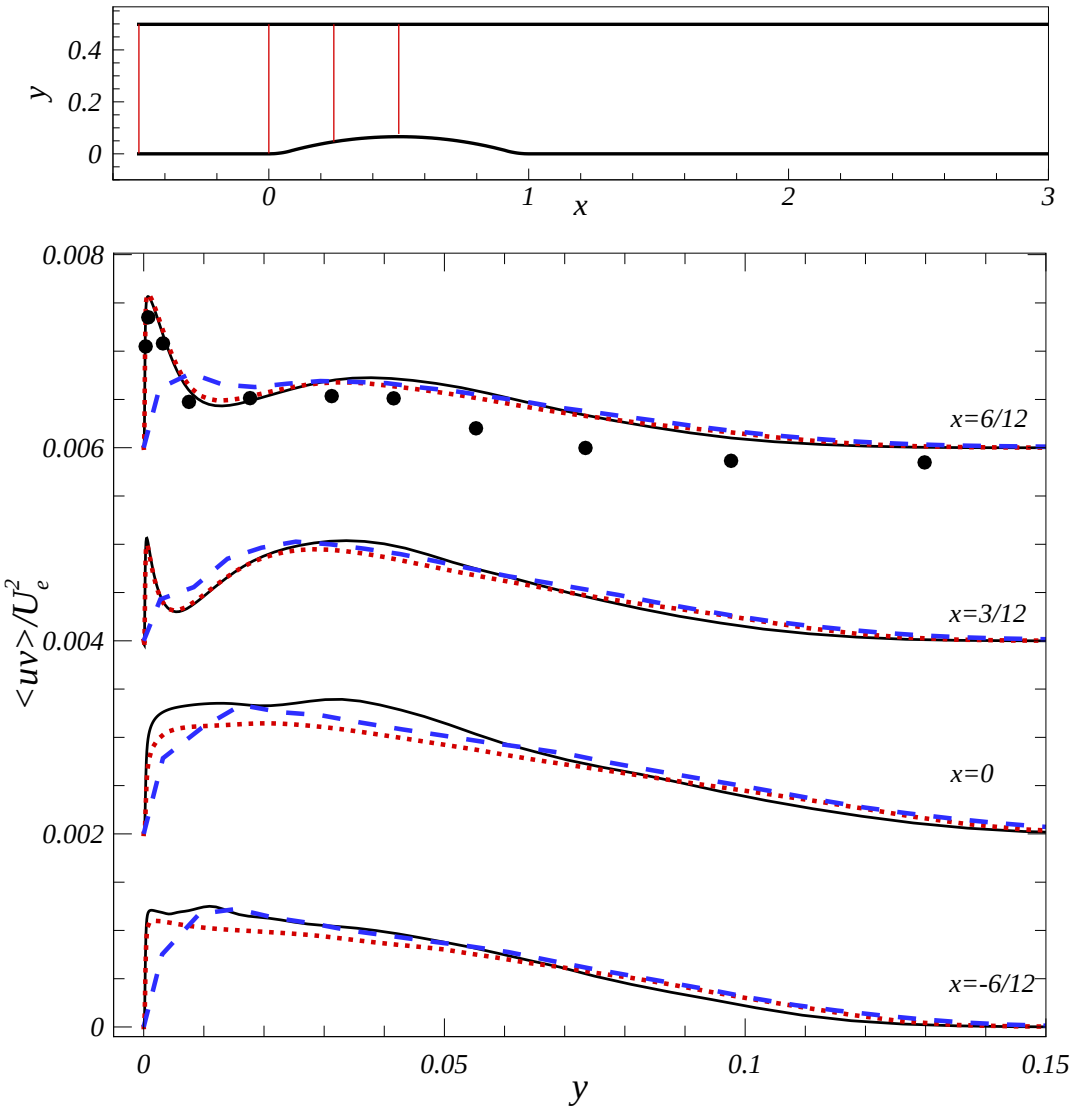

Figure 4.13: Total (resolved + modeled) Reynolds shear stress profile. Log law; WMLES; WMLES with stochastic forcing; • Experiments.

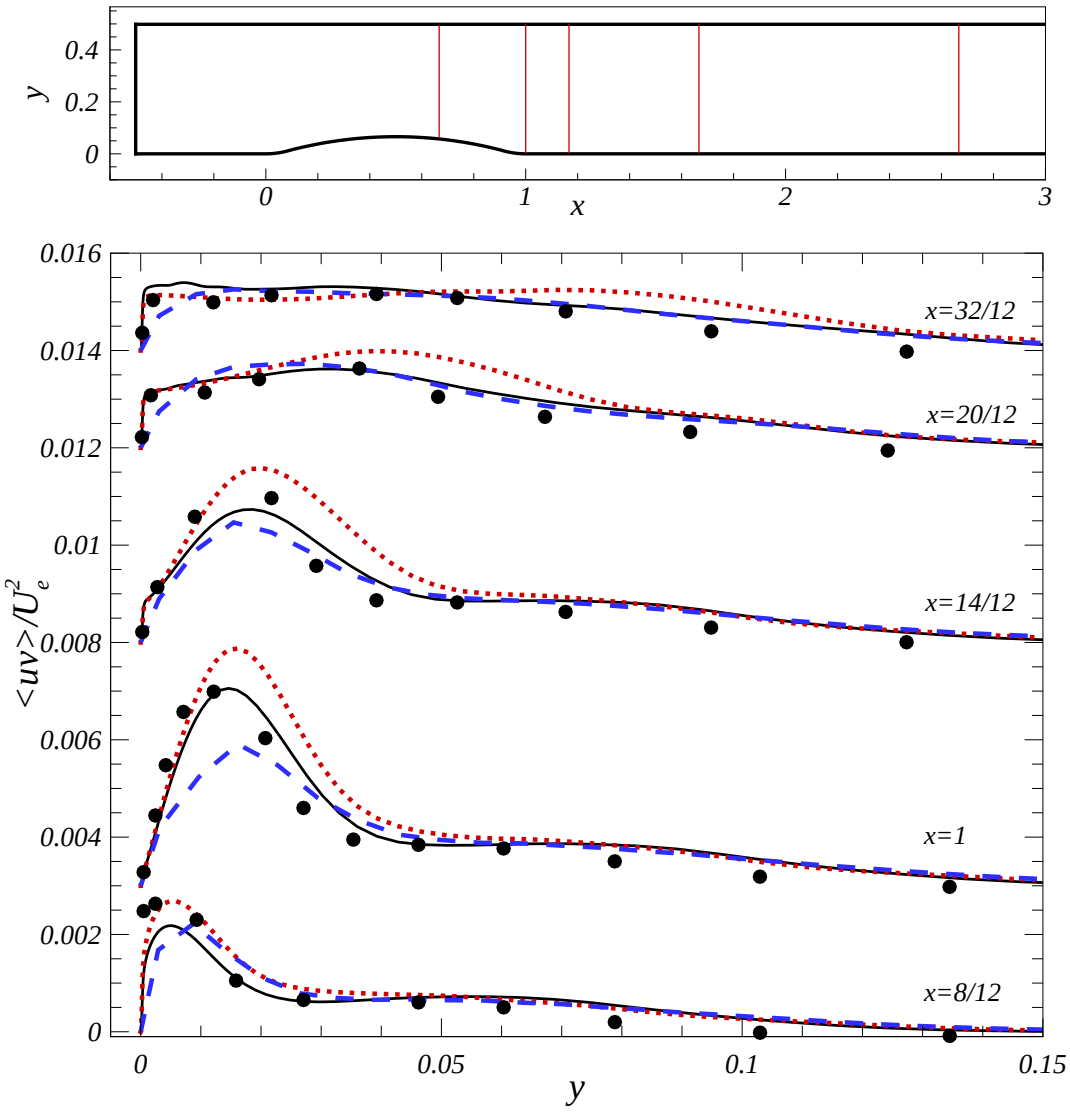

Figure 4.14: Total (resolved + modeled) Reynolds shear stress profile. Log law; WMLES; WMLES with stochastic forcing; • Experiments.

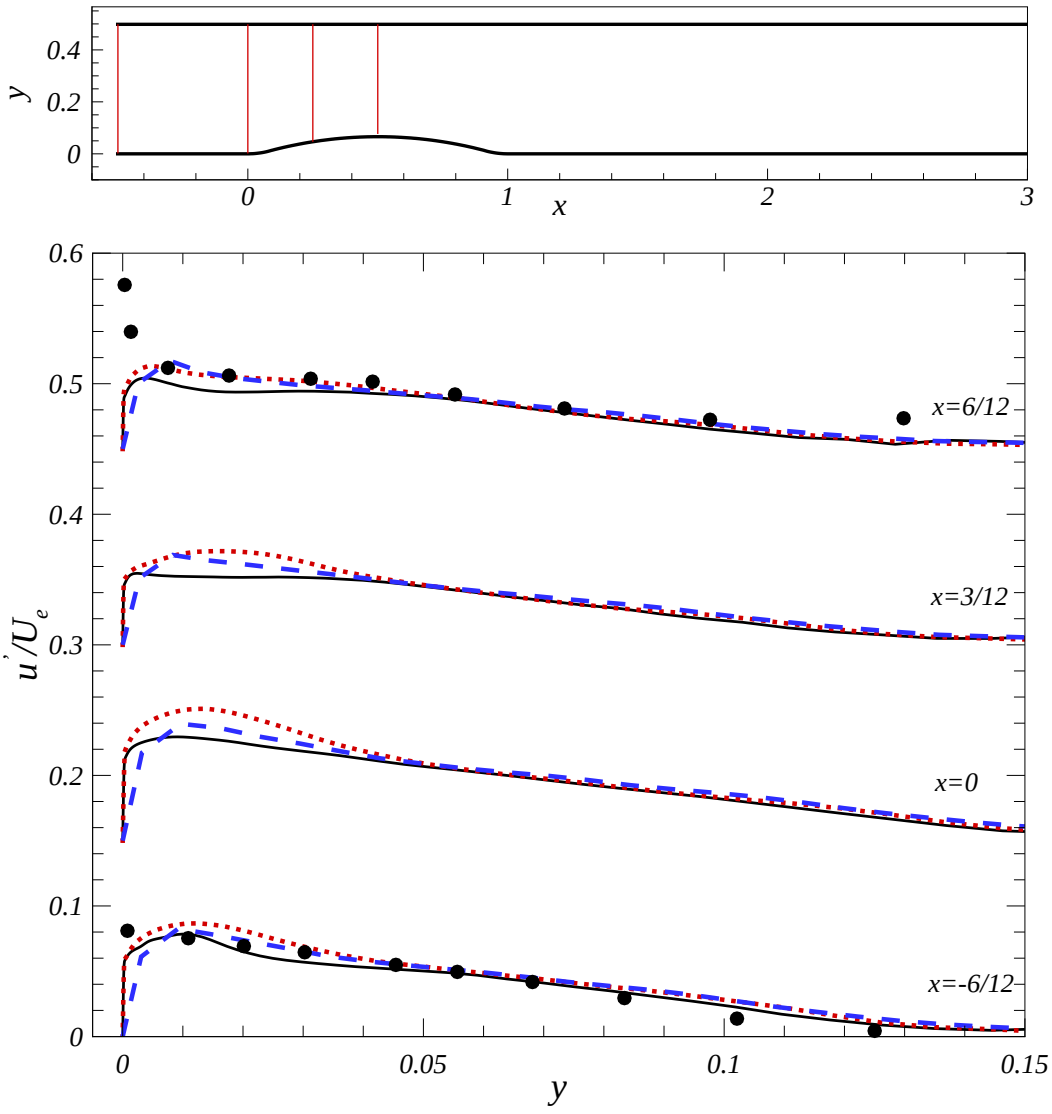

Figure 4.15: RMS of u velocity fluctuations. Log law; WMLES; WMLES with stochastic forcing; • Experiments.

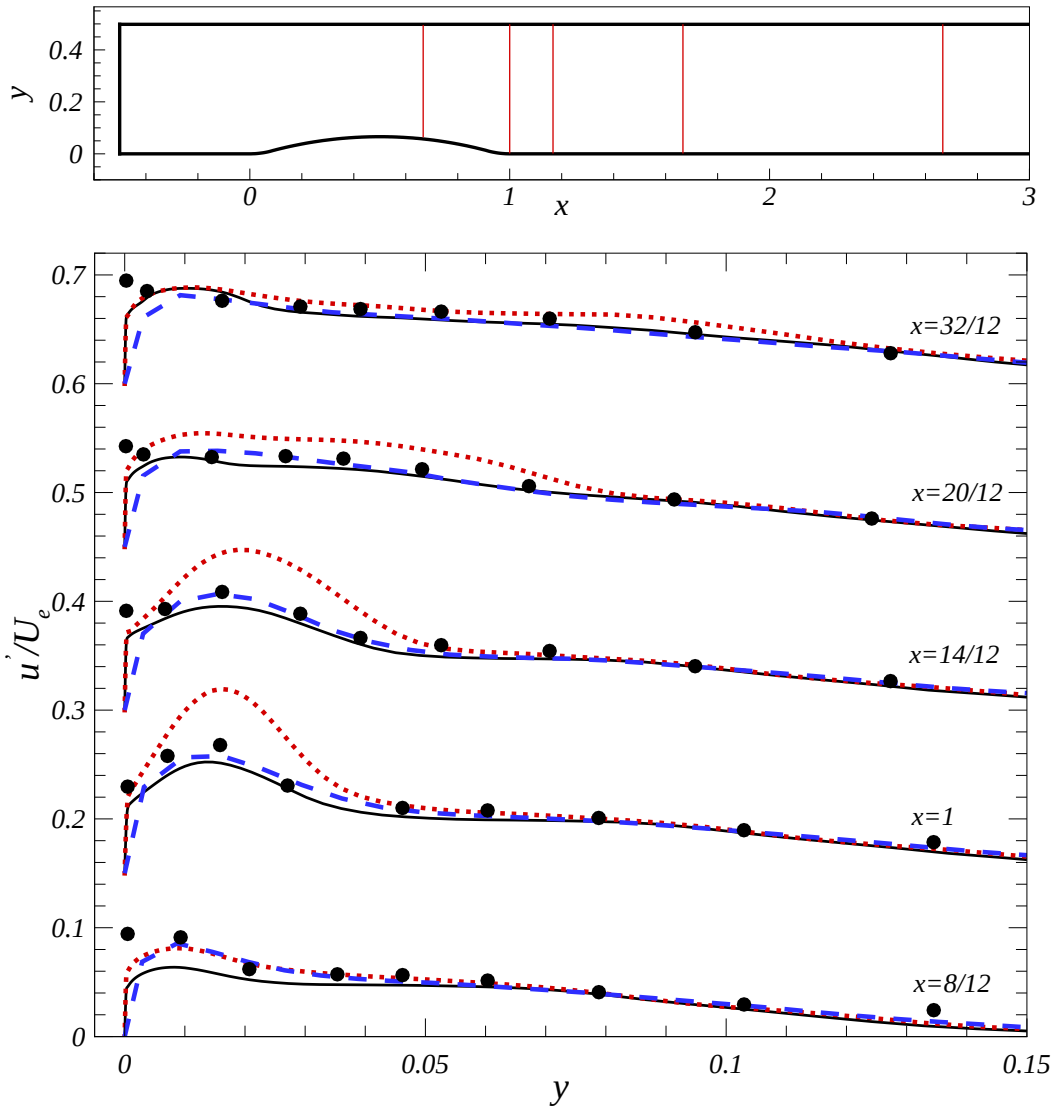

Figure 4.16: RMS of u velocity fluctuations. Log law; WMLES; WMLES with stochastic forcing; • Experiments.

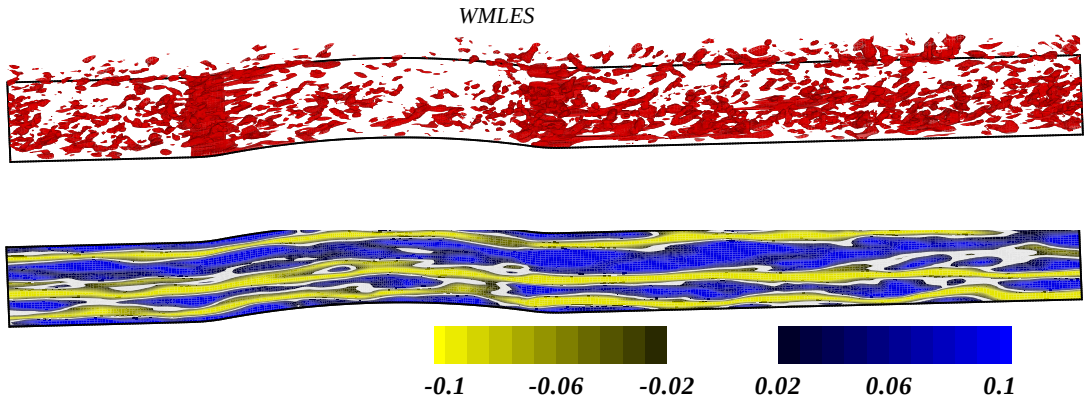

Figure 4.17: Iso-surfaces of $Q = 18$ [*(a)*] horizontal velocity-fluctuation contours in a plane parallel to the wall at $y_w = 0.005$ ($y_w/\delta_{ref} = 0.05$) [*(b)*].WMLES calculation

over-prediction of the Reynolds stresses in the recovery region. In the ramp, the flow separation was a strong perturbation effective in breaking up the super-streaks present in the RANS/LES transition region, whereas the perturbations to the mean flow in the bump are not strong enough to break up the super-streaks. From figure 4.17, it can be seen that super-streaks extend from the inlet to the outflow boundary. Figure 4.18 shows the iso-surfaces of $Q = 18$ and the contours of horizontal velocity fluctuations in a plane parallel to the wall for the WMLES with the stochastic forcing. Comparing figures 4.18 and 4.17 shows that the WMLES calculation with stochastic forcing has more eddy content in the upstream attached boundary layer and on the convex region of the bump, and has less energetic eddies near the trailing edge of the bump, and a weaker streamwise coherence of 'super-streaks'. All of these factors account for the improved prediction of the flow field with the addition of the stochastic forcing.

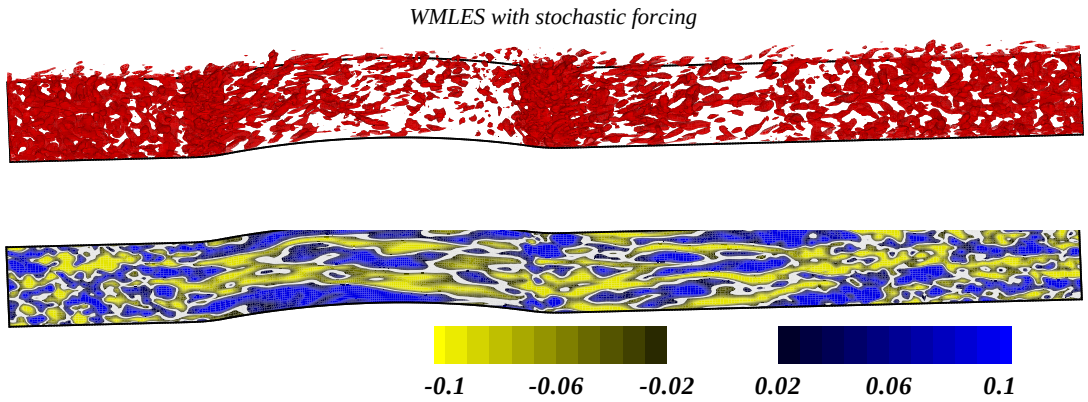

Figure 4.18: Iso-surfaces of $Q = 18$ [*(a)*] horizontal velocity-fluctuation contours in a plane parallel to the wall at $y_w = 0.005$ ($y_w/\delta_{ref} = 0.05$) [*(b)*].WMLES with stochastic forcing

The amplitude of the stochastic forcing used in the WMLES calculation is shown in figure 4.19. Note that, forcing is set to zero in the convex region of the bump. In the first concave region of the bump forcing becomes inactive naturally due to the resolved stresses being larger than the modeled stress in the interface region. Similar to the ramp problem, the adverse pressure gradient in second half of the bump causes the resolved eddies to become energetic, so that the forcing becomes inactive for a short distance downstream of the trailing edge.

4.5 Summary

For the two-dimensional bump problem, all the methods tested performed reasonably well. In the adverse pressure gradient region, the two WMLES calculations and the SST model predicted the mean horizontal velocity better than the

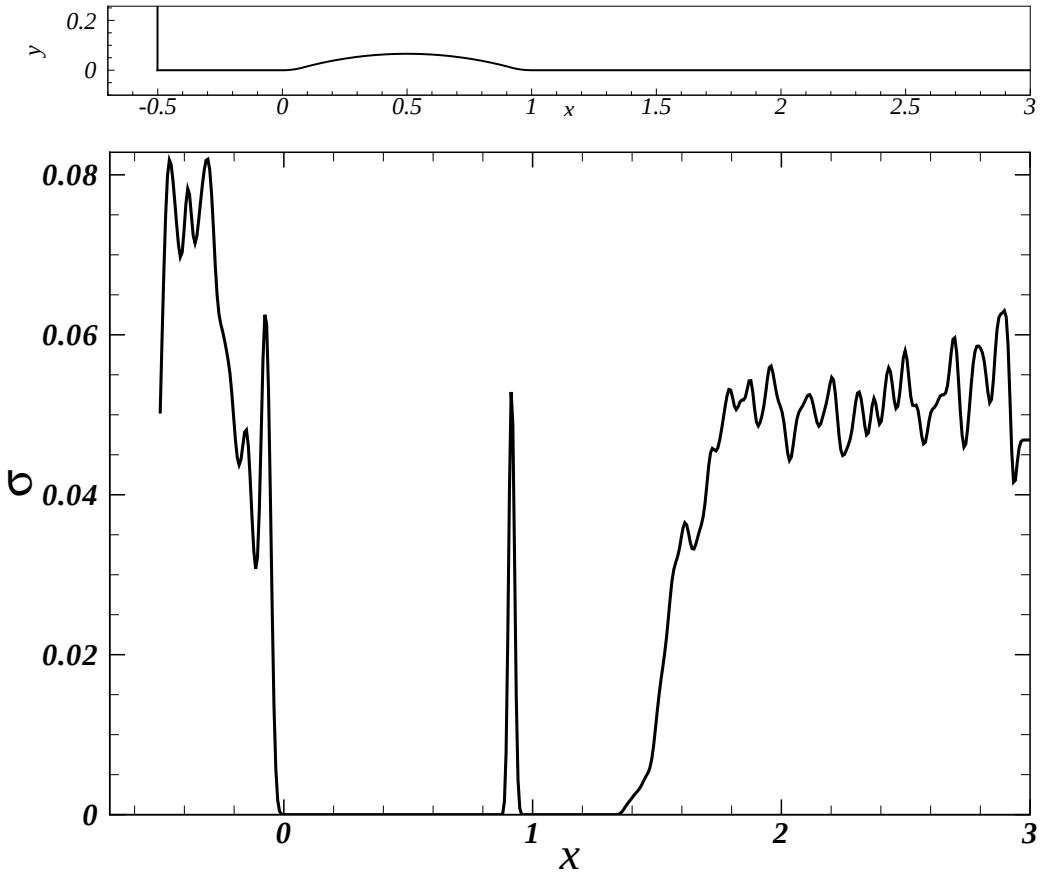

Figure 4.19: RMS of the stochastic forcing.

other RANS models tested. The Reynolds stress transport model predicted the shear stress and rms of the fluctuations accurately everywhere confirming the superiority of the anisotropy resolving models. The SA-RANS and the SST model under-predicted the shear stress by 30% in the adverse pressure gradient region. The WMLES without the stochastic forcing over-predicted the shear stress in the recovery region by 15% due to more energetic eddies generated in the upstream adverse pressure gradient region. Addition of the stochastic forcing to the WMLES calculation yields improved results. The flow recovery after the intermittent separation was predicted well by all the calculations.

Chapter 5

Flow past a swept bump

This chapter presents results from numerical simulations of a flow that is three-dimensional in mean. The flow configuration consists of the two-dimensional bump described in the previous chapter swept at an angle of 45^0 to the approaching turbulent boundary layer. Numerical simulations were performed for a momentum Reynolds number of 11,680 and the results are compared to the measured values from DeGraaff's experiment [33].

5.1 Introduction

Three-dimensional flows are characterized by change in mean flow direction with distance from the surface. In engineering applications three-dimensional flows occur in many instances such as, on swept wings, through curved ducts, at wing/body junctions, in turbomachinery etc. Bradshaw [15] classified three-dimensional flows as either skew-induced, in which three-dimensionality arises either due to applied spanwise pressure gradient (pressure driven) or wall-shear stress along the spanwise direction (shear driven), and stress-induced, in which three-dimensionality arises due to Reynolds stress gradients. In pressure driven flows, the applied spanwise pressure gradient turns slow-moving fluid particles in the near-wall region through a larger

angle than fast-moving fluid particles in the outer region. In shear driven flows, the applied shear stress slowly diffuses spanwise velocity across the boundary layer. A characteristic of three-dimensional flow is the lag of the Reynolds shear stress angle ($\tan^{-1}\langle v'w'\rangle/\langle u'v'\rangle$) with respect to mean shear angle ($\tan^{-1}\langle \partial W/\partial y\rangle/\langle \partial U/\partial y\rangle$). Townsend's structure parameter, a_1, which is defined as the ratio of Reynolds shear stress ($\sqrt{(< u'v' >^2 + < v'w' >^2)}$) to twice the turbulent kinetic energy, is reduced from its typical value of 0.15 observed in the two-dimensional boundary layer, indicating a less efficient mixing in three-dimensional flows. Note that the Reynolds shear stress defined above is invariant with respect to an arbitrary rotation of the $x-z$ axes about y axis. Bradshaw [15] presents a review of various works on three-dimensional flows up until late eighties; Johnston and Flack [57] review experiments results that were published since then, whereas Eaton [39] reviews experiments conducted in his laboratory to investigate the distortion of near-wall turbulence structures.

Bradshaw and Pontikos [16] report experimental measurements on a swept wing. The flow over the swept wing experienced an adverse streamwise pressure gradient as well as a spanwise pressure gradient. Their results shows that in three-dimensional turbulent boundary layer the diffusion of momentum, turbulent energy and shear stress across the boundary layer is reduced. They hypothesize that the large eddies present in two-dimensional flows are tilted sideways by spanwise shear which reduces their efficiency in mixing.

Moin *et al.* [84] numerically studied the transient three-dimensional flow created due to application of a spanwise pressure gradient in a channel flow. They observe a decrease in turbulent kinetic energy, Reynolds shear stress and the structure parameter, a_1. They attribute the decrease in pressure-strain as the cause for change in turbulence; decrease in pressure-strain results in a reduced production of wall-normal Reynolds stress $< v'^2 >$ and leads to a decrease in the wall-normal Reynolds stress. This results in the suppression of Reynolds shear stress $< u'v' >$ production and causes reduced values of Reynolds shear stress which in turn affects the turbulent kinetic energy production and results in decreased turbulent kinetic energy.

Coleman *et al.* [27] performed direct numerical simulation of channel flows subjected to spanwise wall motion. They observed a decrease in turbulent kinetic energy and wall shear stress which later recover to values greater than their initial values. The streamwise and spanwise spectra showed that the small structures respond to the spanwise shear by reorienting sooner than large structures. They conjecture that the effect of shear driven three-dimensional flows on turbulence structure is due to the modification of the interaction between the streamwise vortices and the near-wall streaks.

Kannepalli and Piomelli [59] performed large-eddy simulation to study the response of a spatially developing two-dimensional turbulent boundary to spanwise wall-shear and its subsequent relaxation to a two-dimensional state after the re-

moval of the spanwise-wall shear. The boundary layer development region can be divided into five regions; an equilibrium two-dimensional region, non-equilibrium region following the imposition of spanwise wall-shear stress where the flow becomes three-dimensional, a near equilibrium three-dimensional region where the spanwise velocity changes only in the outer region, a non-equilibrium region where the three-dimensional flow recovers to a two-dimensional state after the removal of spanwise wall-shear stress and finally an equilibrium region where the flow is close to a two-dimensional state. The spanwise velocity component grows like a Stokes layer independent of the streamwise velocity and it is self-similar when normalized by the wall-velocity. They observe that the imposition of the spanwise shear disrupts the near-wall streaks and the vortical structures in the outer region; downstream, new structures and the near-wall streaks aligned with the wall-shear are generated. They attribute this disruption of turbulence structures as the cause for reduction in the Reynolds shear stress in the non-equilibrium region. They also observe a reduction of turbulent kinetic energy in the non-equilibrium regions which they attribute to the decreased production.

Kiesow and Plesniak [61] experimentally studied the development of shear driven three-dimensional turbulent boundary layer in a configuration similar to the one numerically studied by Kannepalli and Piomelli [59]. Their flow visualization using laser induced fluorescence showed that the near-wall streak length are reduced by 50% due to imposition of spanwise wall-shear stress. Power spectra of velocity

shows that the energy is shifted to higher frequency implying a lower streamwise length scale. The boundary layer thickens and the deficit in the streamwise velocity component increases with the increase in the cross flow.

5.2 Problem formulation

The accuracy of WMLES and various RANS models for three-dimensional flows is tested in this work. A three-dimensional geometry is formed by turning the two-dimensional bump at an angle of 45 degrees to the inlet mean flow. This creates a spanwise pressure gradient that turns the streamlines to generate a three-dimensional boundary layer. Experiments on this geometry were conducted by Webster *et al.* [138] and DeGraaff [33] and the results for the Reynolds number simulated in the present study are reported in [33]. Wu and Squires [141] simulated this flow at a lower Reynolds number ($Re_\theta = 3800$) than the one studied in this work. In the experiments [33], a suction slot is present parallel to the spanwise axis of the bump to facilitate the development of a boundary layer that is homogeneous along the spanwise axis of the bump. In the numerical calculations, the computational domain (see the sketch in figure 5.1) is rotated to an angle of 45 degrees to the inlet mean flow so that spanwise direction (z_1) of the computational domain coincides with the spanwise axis of the bump. Numerical calculations use the coordinate system (x_1, y, z_1), where z_1 is a direction of homogeneity; the flow quantities are then transformed to the (x, y, z) coordinate system for comparison with experimental

values. The reference location is located one-half chord-length upstream of the leading edge of the bump. The momentum Reynolds number Re_θ is 11,680 at the reference location.

RANS calculations were performed with the SA model, the $k-\epsilon$ model, the SST model and the Reynolds stress transport model. Similar to the two-dimensional bump problem, the $k-\epsilon$ model gave results which are very close to those of the SA-RANS model and are not shown. WMLES were performed with and without the application of stochastic forcing. Large-eddy simulations were performed with the Lagrangian dynamic model and log-law boundary conditions. All the calculations used the same grid that was used in two-dimensional bump calculation. RANS and LES results are presented in the following section and the WMLES results are presented after the following section.

5.3 RANS and LES results

Figure 5.2 shows the pressure coefficients, the streamwise and the spanwise skin-friction coefficients which are defined as

$$C_p = \frac{p - p_{ref}}{\rho U_{ref}^2/2}; \qquad C_f = \frac{\tau_{ws}}{\rho U_\infty^2/2}; \qquad C_{fz} = \frac{\tau_{wz}}{\rho U_\infty^2/2}, \tag{5.1}$$

where τ_{ws} is the streamwise wall shear, τ_{wz} is the spanwise wall shear, U_∞ is the velocity at the edge of the boundary layer at the current location, p_{ref} is the wall pressure at $x = 1.667$ and U_{ref} is the velocity at the edge of the boundary layer at $x = 1.667$. The wall-pressure coefficient was measured in the experiments for a lower

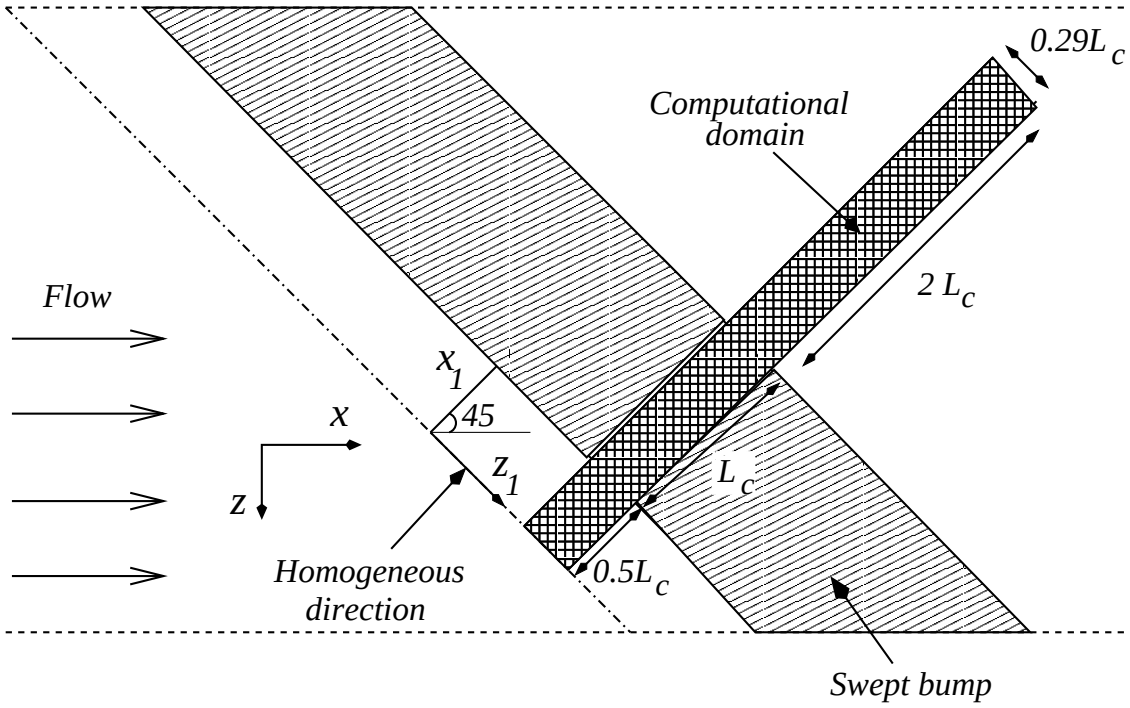

Figure 5.1: Top view of the computational domain

Reynolds number with $Re_\theta = 3260$ at the reference section. All the calculations agree with each other, but they differ from the experimental pressure coefficient at the low Reynolds number in the flat-plate region before the bump. This implies that all the calculations predict a stronger adverse pressure gradient than the experiment near the leading edge.

Note that in experiments, the streamwise skin-friction was measured only for the low Reynolds number($Re_\theta = 3260$) case. Streamwise skin-friction for this high Reynolds number was estimated by the same assumption used in the two-dimensional problem. In the flat-plate region ahead of the bump, the trend seen in the two-dimensional bump problem is repeated here. The SST model predicts the

skin-friction accurately whereas the Reynolds stress transport model over-predicts it. In the adverse pressure gradient region after the bump, the SST model and the LES calculation predict the skin-friction reasonably well. All the RANS models predict the recovery accurately.

Figures 5.3 and 5.4 show the mean horizontal velocity profiles at select locations. In these figures, the mean horizontal velocity is normalized by the local free stream velocity. Experimental data is available only from the summit of the bump and at the reference location. All the calculation predict the effect of the adverse pressure gradient near the leading edge and the favorable pressure gradient till the summit of the bump. In the adverse pressure gradient region, all the RANS models over-predict the mean velocity in the near-wall region whereas the LES calculation based on the log-law boundary condition predicts it reasonably well. The RANS models good prediction of the recovery region is partly due to their incorrect prediction of deceleration of the mean velocity in the adverse pressure gradient region.

Figure 5.5 shows the streamlines in a plane parallel to the wall obtained from the WMLES which is representative of the trends seen in all the calculations. The pressure gradient along the direction of homogeneity ($\partial p/\partial z_1$) is zero, so that the spanwise pressure-gradient can be expressed in terms of the streamwise one: $\partial p/\partial z = -\partial p/\partial x \ \tan\alpha$). Thus the spanwise pressure gradient is of opposite sign to the streamwise pressure gradient. The turning of the streamlines along the spanwise direction can be explained in terms of the spanwise pressure gradient: a

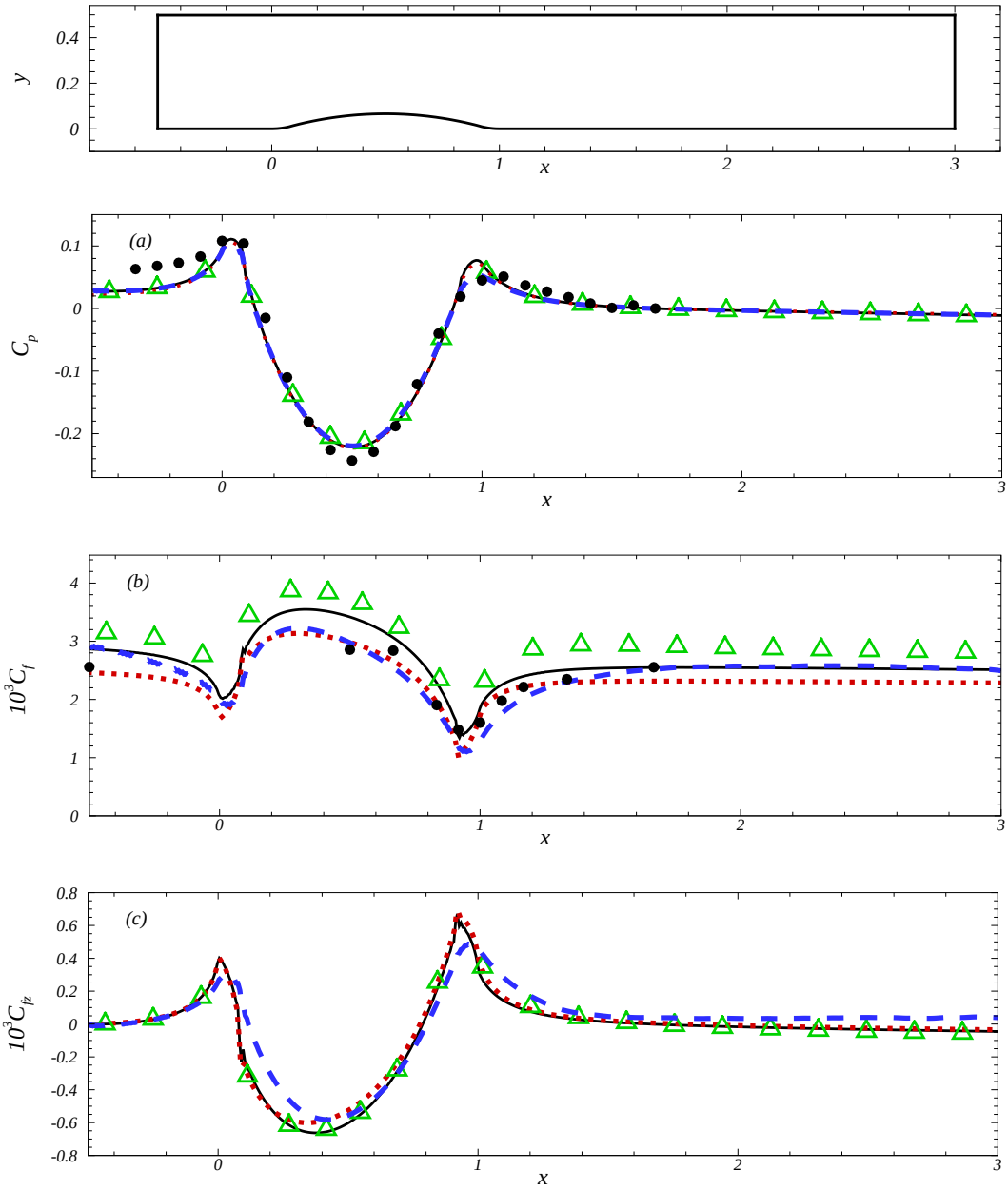

Figure 5.2: Profiles of (a) pressure coefficient (b) streamwise skin-friction coefficient and (c) spanwise skin-friction coefficient. ——— SA-RANS; ····· SST model; △ Reynolds stress transport model; – – – Log law; • Experiments.

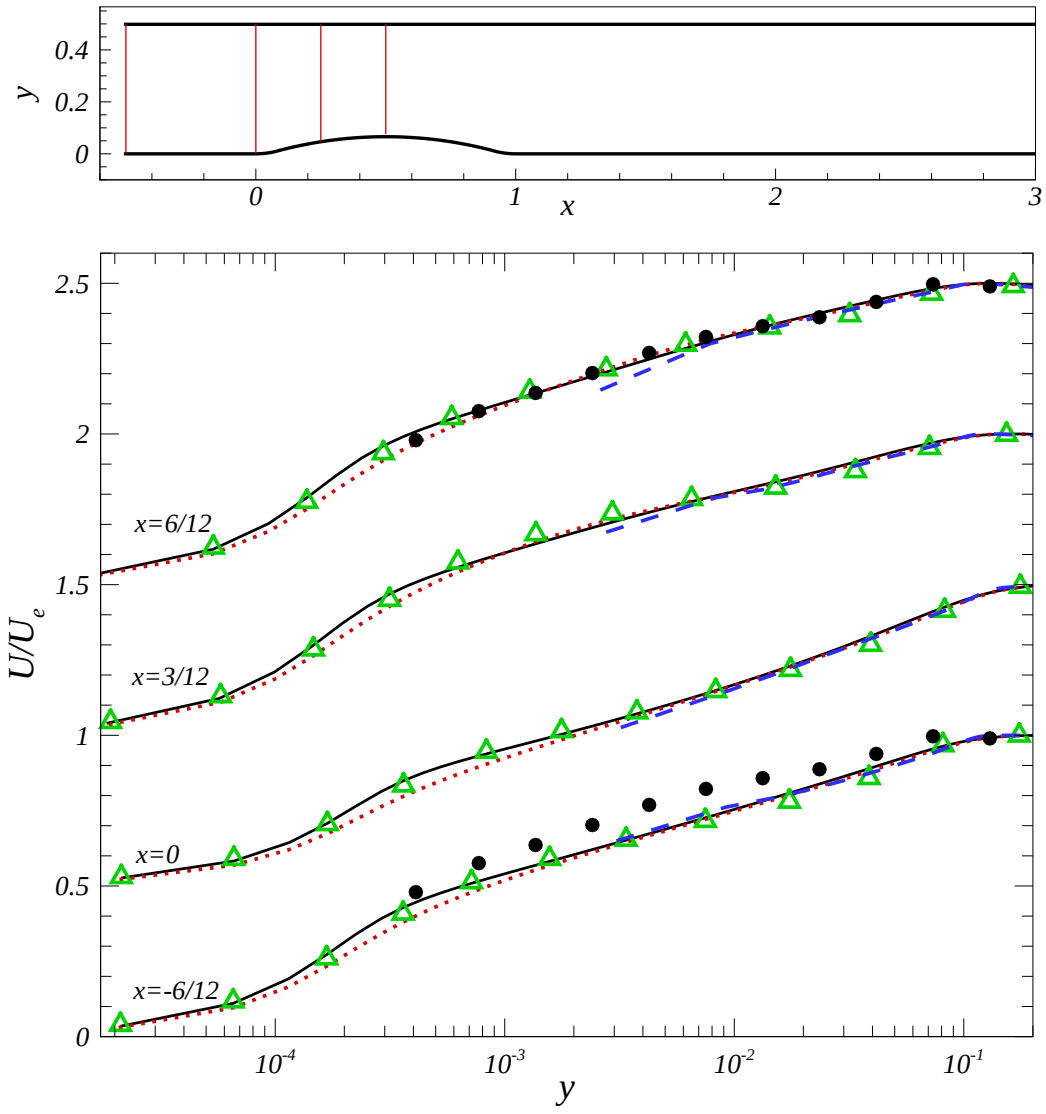

Figure 5.3: Mean horizontal velocity profile. ——— SA-RANS; ····· SST model; △ Reynolds stress transport model; – – – Log law; • Experiments.

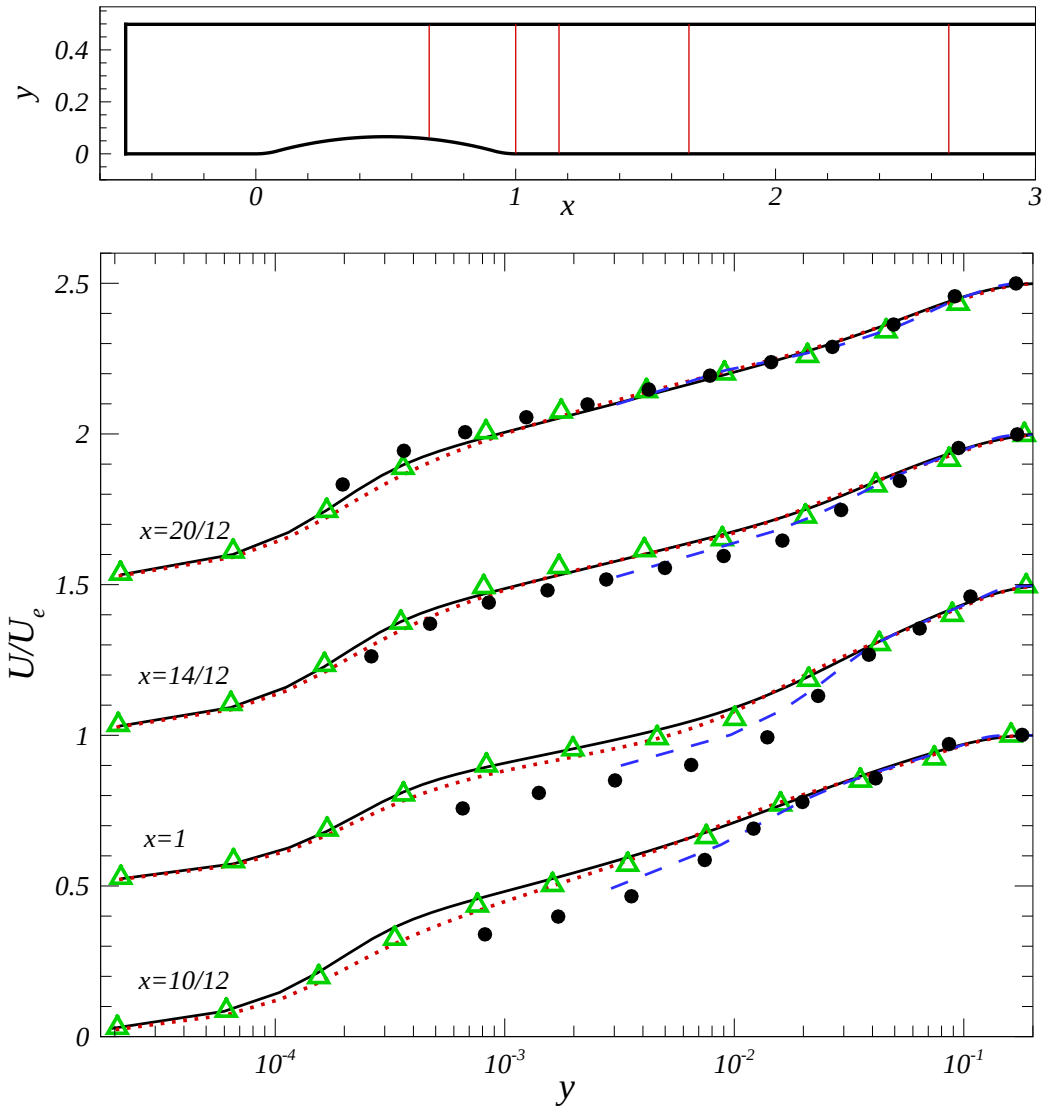

Figure 5.4: Mean horizontal velocity profile. ——— SA-RANS; ····· SST model; △ Reynolds stress transport model; – – – Log law; • Experiments.

mild adverse pressure gradient region exists ahead of the bump, which results in a positive spanwise pressure gradient. Hence in this region the flow turns slightly in the positive z direction. In the favorable pressure gradient region, a negative spanwise pressure gradient acts on the flow which turns the flow in the negative z direction. In the adverse pressure gradient region after the bump summit, a positive spanwise pressure gradient acts on the flow. The flow responds to this positive spanwise pressure gradient by turning into the positive z direction slowly. Downstream of the trailing edge, where there is no streamwise pressure gradient and consequently no spanwise gradient, the flow slowly relaxes to a two-dimensional boundary layer.

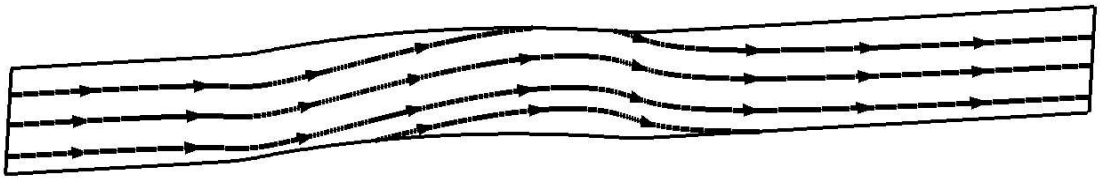

Figure 5.5: Streamlines in a plane parallel to the wall at $y_w = 0.0055$ ($y_w/\delta_{ref} = 0.06$) WMLES calculation

Figures 5.6 and 5.7 show the mean spanwise velocity profiles at the same locations. At the leading edge, the positive spanwise pressure gradient, turns the flow along the positive z direction. The maximum spanwise velocity is reached in the near-wall region since the slow- moving near-wall flow can be turned through a larger angle than the fast-moving flow in the outer region. At the summit of the bump, the flow is turned along the negative z direction due to the negative spanwise pressure-gradient. At the bump summit, all the calculations predict the mean spanwise velocity reasonably well. At the trailing edge, the peak in the spanwise velocity is under-predicted by all the calculations. In the recovery region, all the calculations predict a faster return to two-dimensionality than the experiments.

Figures 5.8 and 5.9 show the Reynolds shear stress profiles at select locations. The SST model and the SA-RANS model under-predict the Reynolds shear stress in the adverse pressure gradient region whereas the Reynolds stress transport model and the LES calculation based on the log-law boundary condition show a better match with the experiments. Figures 5.10 and 5.11 show the rms of u-velocity fluctuations. Both Reynolds stress transport model and the LES calculation based

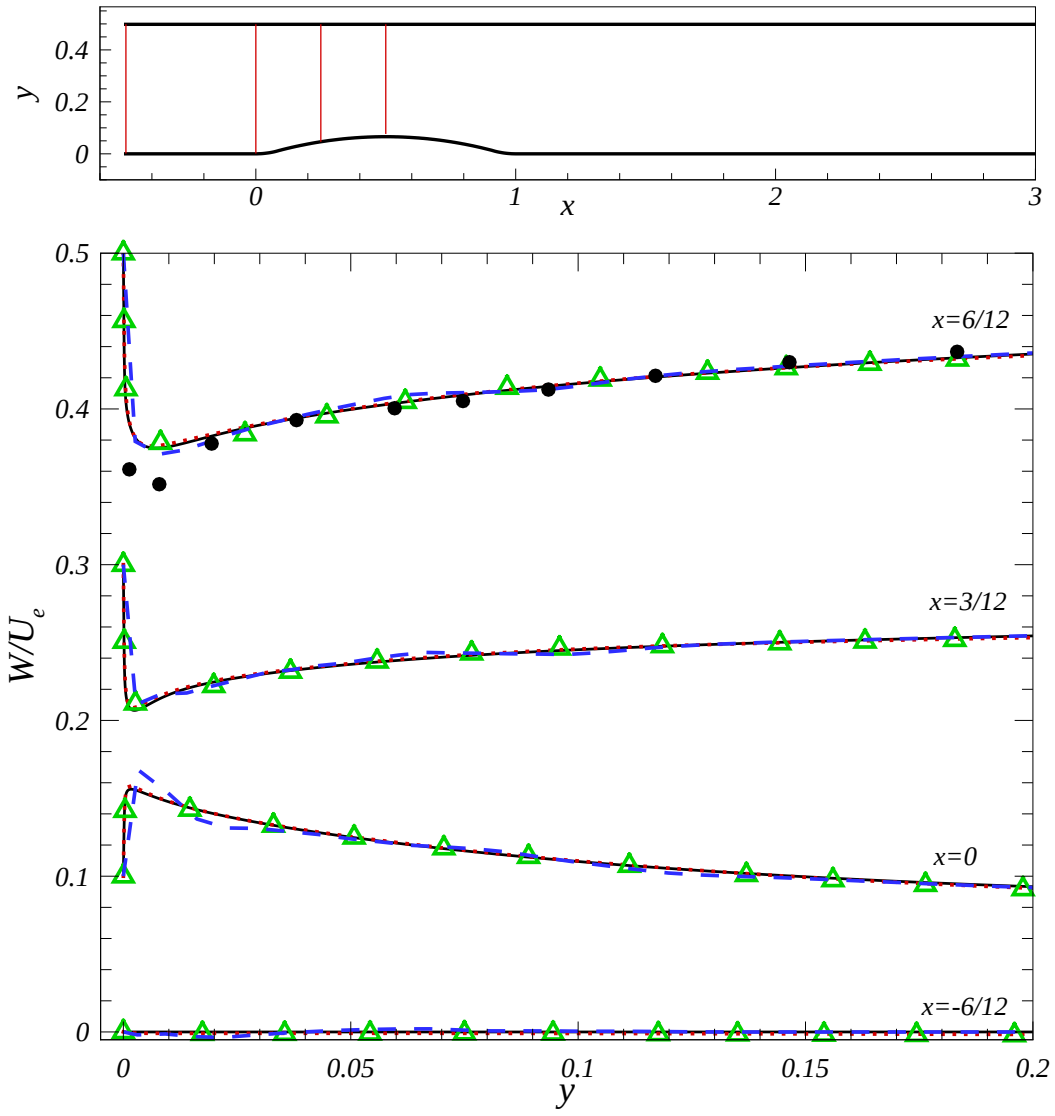

Figure 5.6: Mean spanwise velocity profile. ——— SA-RANS; ····· SST model; △ Reynolds stress transport model; – – – Log law; • Experiments.

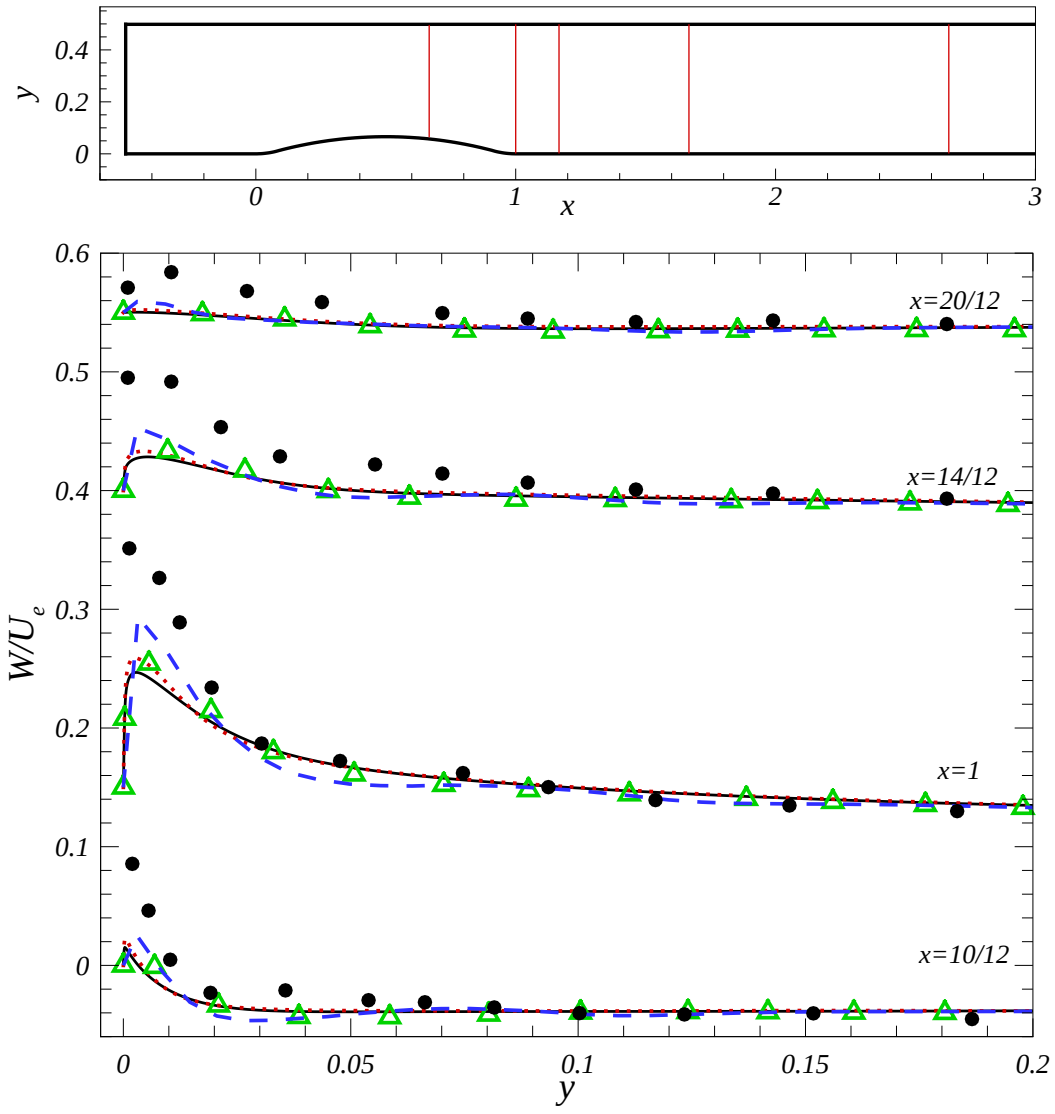

Figure 5.7: Mean spanwise velocity profile. ——— SA-RANS; ····· SST model; △ Reynolds stress transport model; – – – Log law; • Experiments.

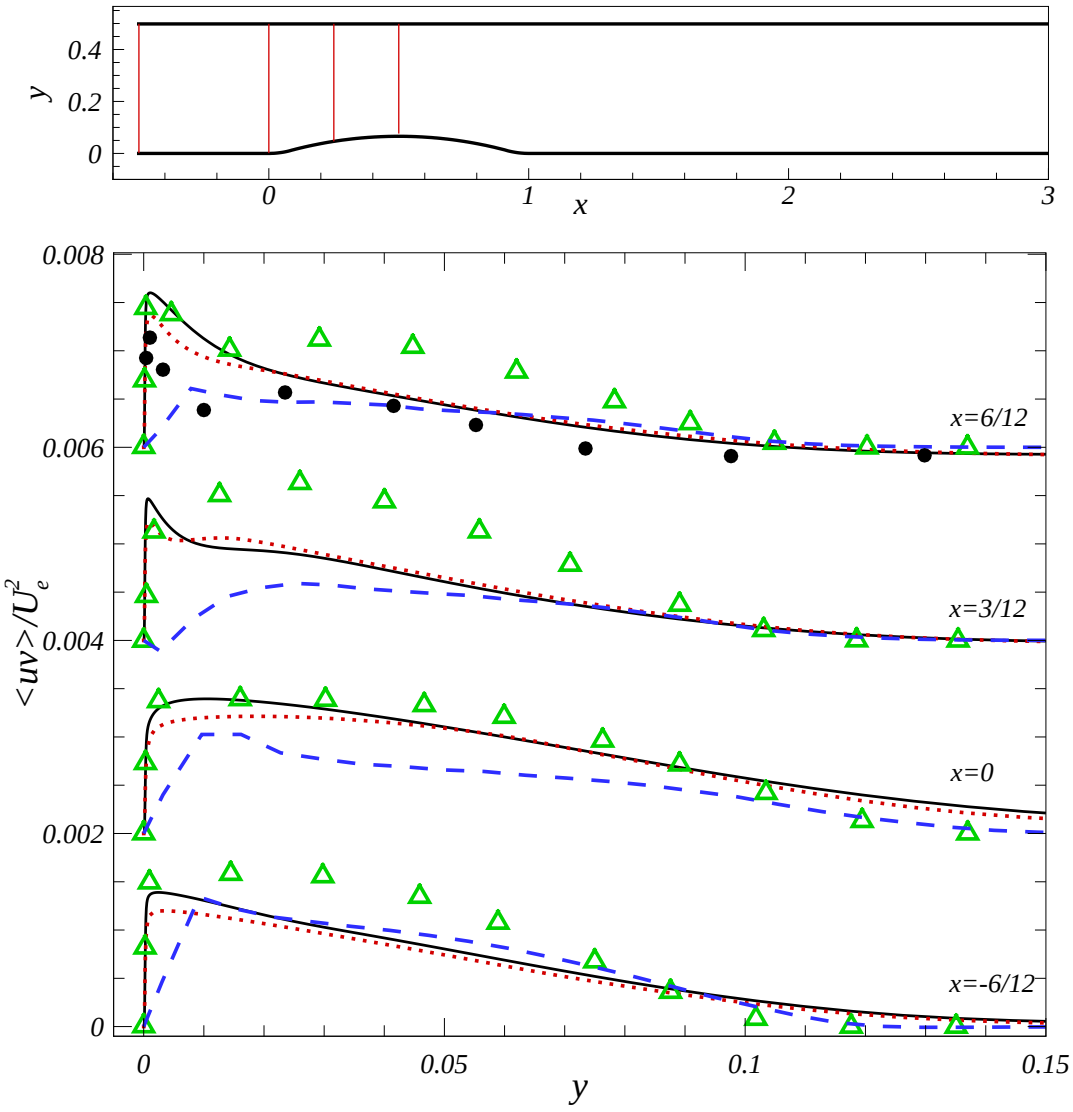

Figure 5.8: Total (modeled + resolved) Reynolds shear stress profile —— SA-RANS; ------ SST model; △ Reynolds stress transport model; – – – Log law; • Experiments.

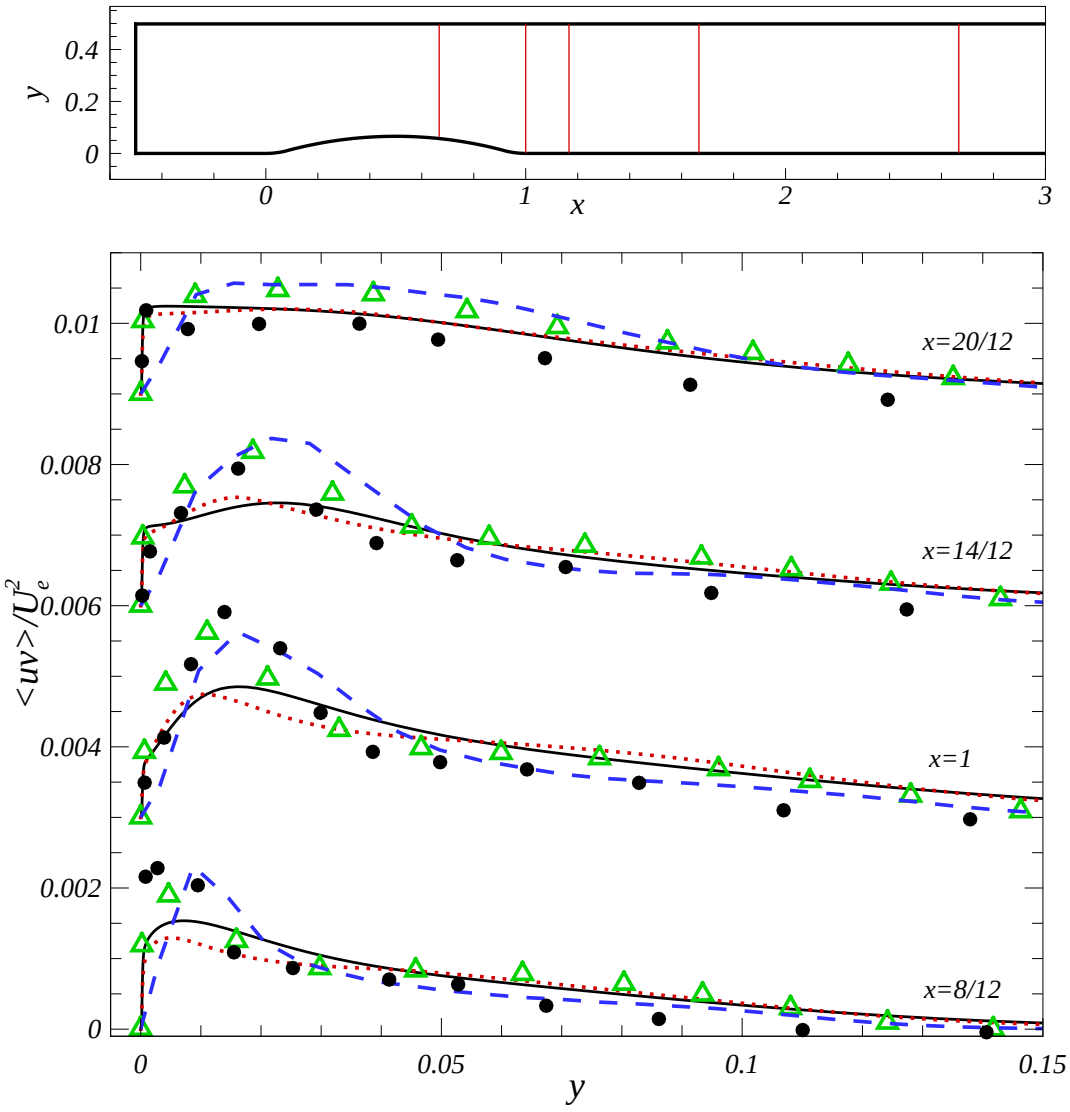

Figure 5.9: Total (modeled + resolved) Reynolds shear stress profile —— SA-RANS; ------ SST model; △ Reynolds stress transport model; – – – Log law; • Experiments.

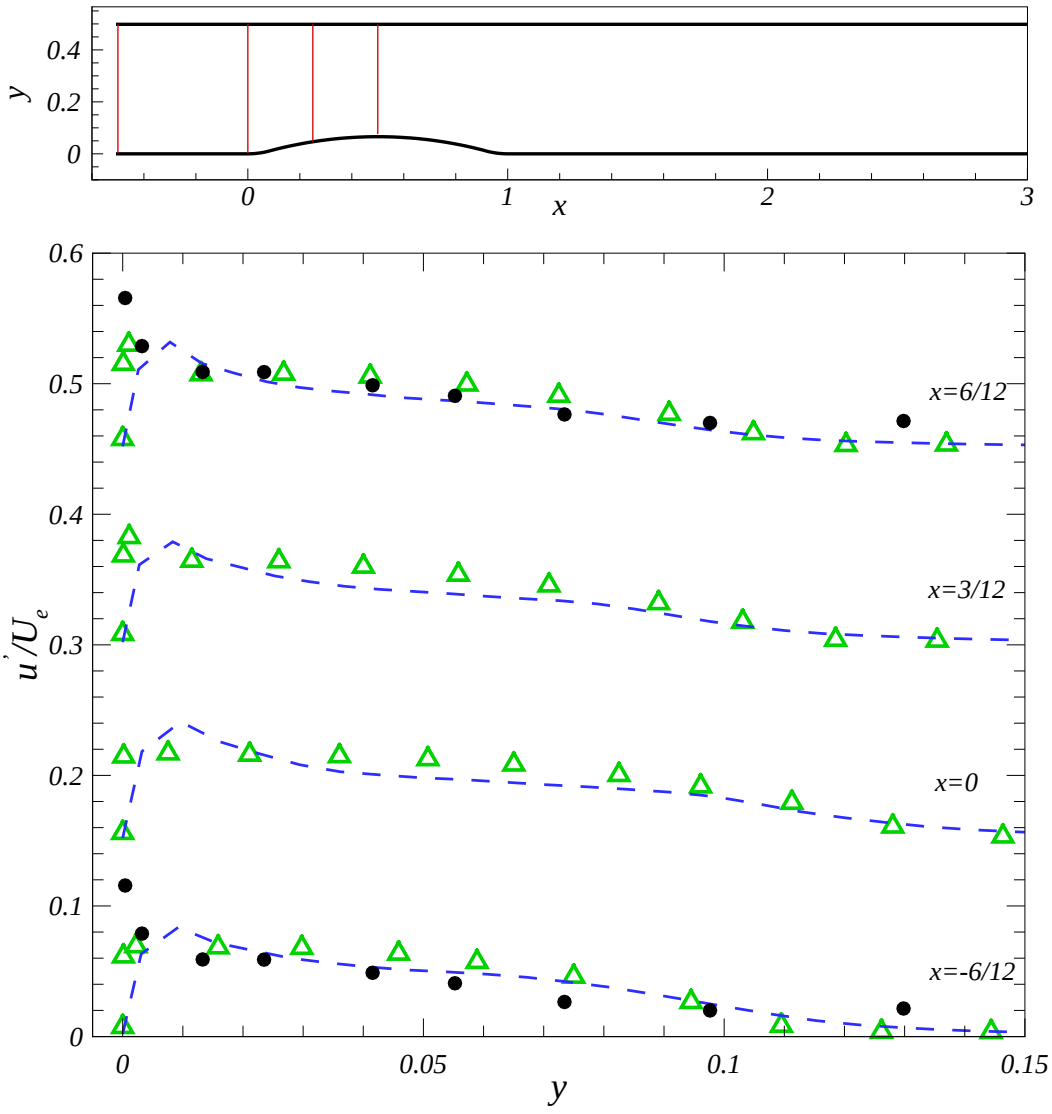

Figure 5.10: RMS of u velocity fluctuation △ Reynolds stress transport model; — — Log law; • Experiments.

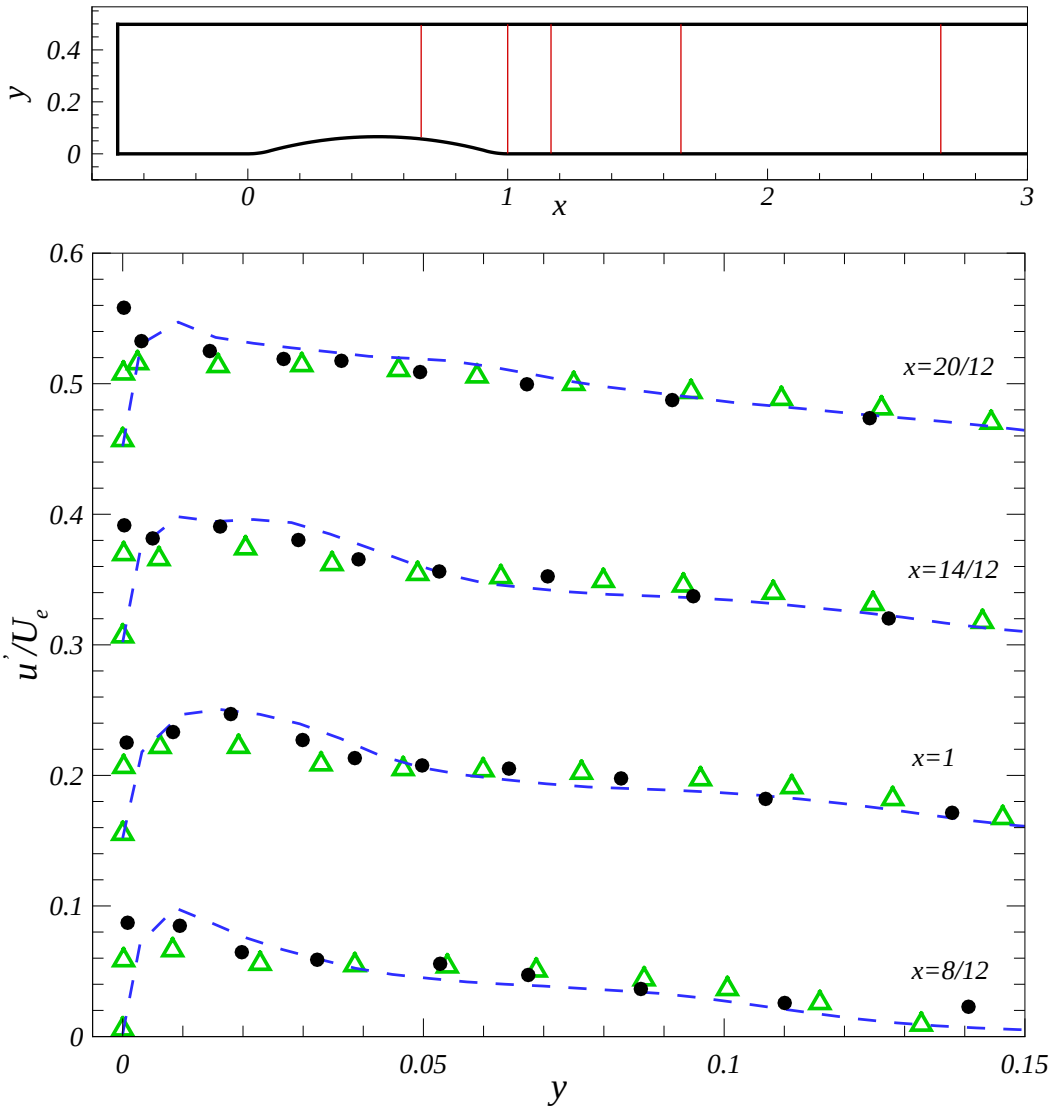

Figure 5.11: RMS of u velocity fluctuation △ Reynolds stress transport model; — — Log law; • Experiments.

on the log-law boundary condition predict it reasonably well everywhere.

5.4 WMLES results

Figure 5.12 shows the variation of pressure coefficient, streamwise friction coefficient and the spanwise friction coefficient over the flow domain. In the flat-plate region ahead of the bump, the WMLES without the stochastic forcing show the expected under-prediction and the addition of the stochastic forcing improves it. Over the bump and in the recovery region, both the WMLES show a good agreement with the experiments. The spanwise skin-friction coefficient predicted by both the WMLES agree well.

Figures 5.13 and 5.14 show the mean horizontal velocity profiles at select locations. Note that, in the adverse pressure gradient region, unlike the RANS models, both the WMLES show a much better agreement with the measured values from the experiment. Figures 5.15 and 5.16 show the mean horizontal spanwise velocity profiles at the same locations. At the summit of the bump, the prediction of the spanwise velocity is good. Near the trailing edge, the peak value of the spanwise component is under-predicted by all the calculations. Both WMLES calculation show a much faster return to two-dimensional state than the experiments in the recovery region. Figures 5.17 and 5.18 show the Reynolds shear stress at select locations. Unlike the RANS models, which did not predict the knee point in the Reynolds shear stress profile, both WMLES calculations predict the knee point and

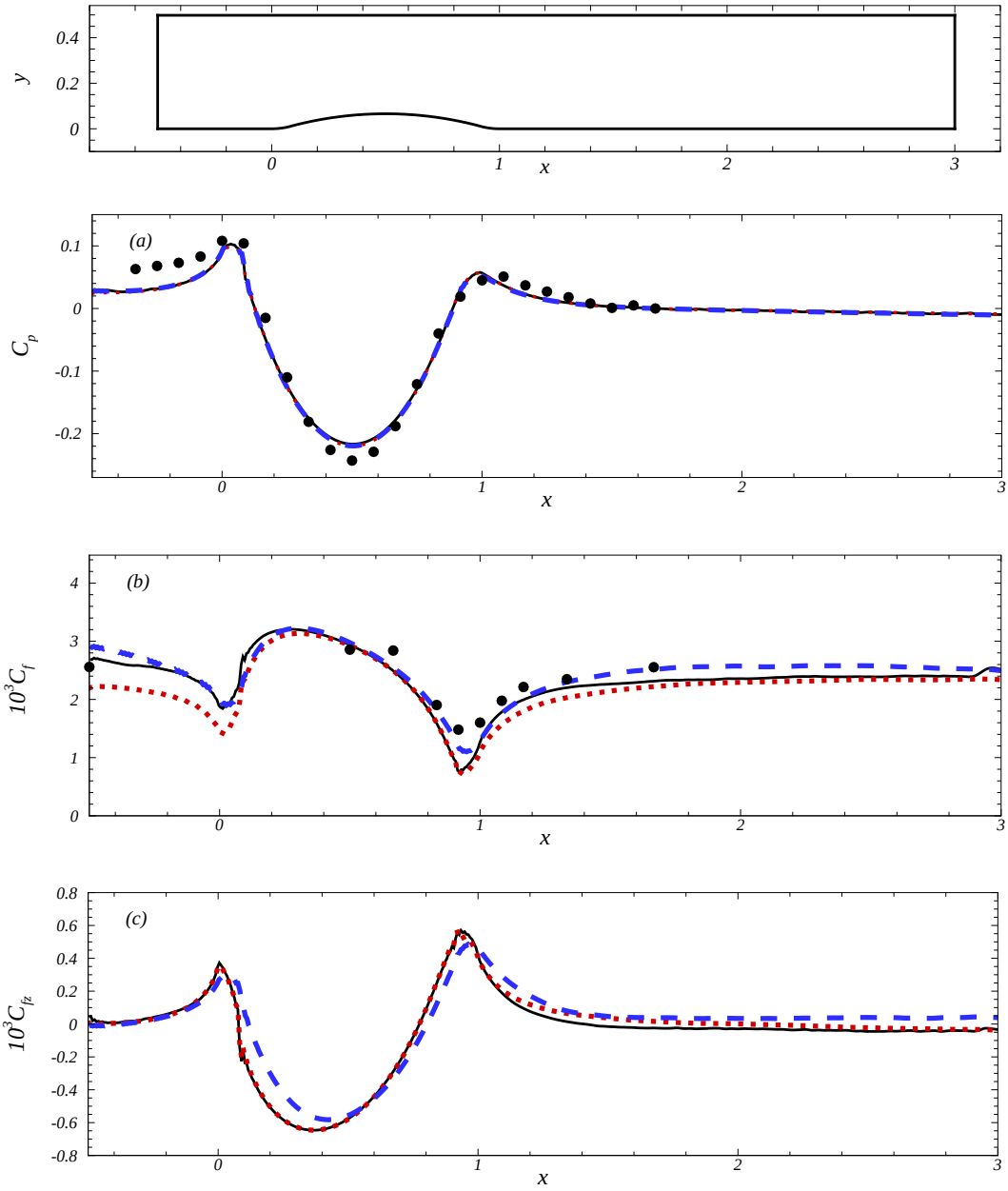

Figure 5.12: Profiles of (a) pressure coefficient (b) streamwise skin-friction coefficient and (c) spanwise skin-friction coefficient. — Log law; ····· WMLES; —— WMLES with stochastic forcing; • Experiments.

the internal layer development accurately in the first half of the bump. In the adverse pressure gradient region, the WMLES without the stochastic forcing under-predicts the Reynolds shear stress; the addition of the stochastic forcing improves it. Overall, the WMLES with the stochastic forcing shows good prediction everywhere. Figures 5.19 and 5.20 show the rms of u-velocity fluctuations at select locations. Both WMLES show good agreement with the measured values from experiments everywhere. Note that, for the two-dimensional bump, the WMLES without the stochastic forcing over-predicted the u-velocity fluctuations in the adverse pressure gradient region; in the three-dimensional bump case, the magnitude of the adverse pressure gradient is smaller which perhaps results in good prediction of the Ryenolds stresses.

5.5 Summary

For the three-dimensional bump problem, all the RANS models tested predicted the mean horizontal velocity poorly in the adverse pressure gradient region. The SST model and the SA-RANS model under-predicted the Reynolds shear stresses in the adverse pressure gradient region. The Reynolds stress transport model predicted the Reynolds stresses better, probably due to its ability to resolve the stress anisotropy. Compared to the two-dimensional bump, the magnitude of the pressure gradient in the three-dimensional bump case is smaller due to lesser constriction and expansion imposed by the three-dimensional geoemetry. This results

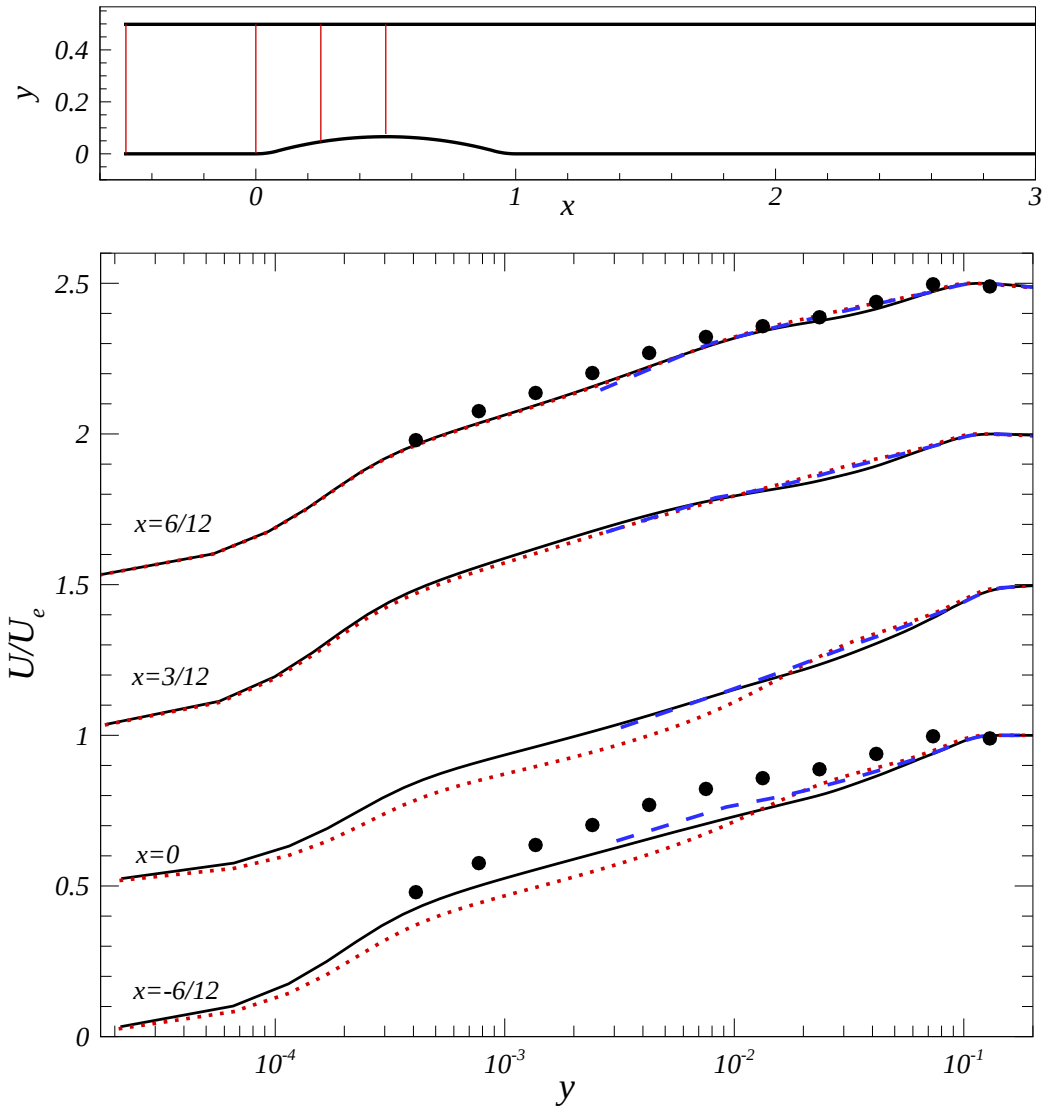

Figure 5.13: Mean horizontal velocity profile. Log law; WMLES; WMLES with stochastic forcing; • Experiments.

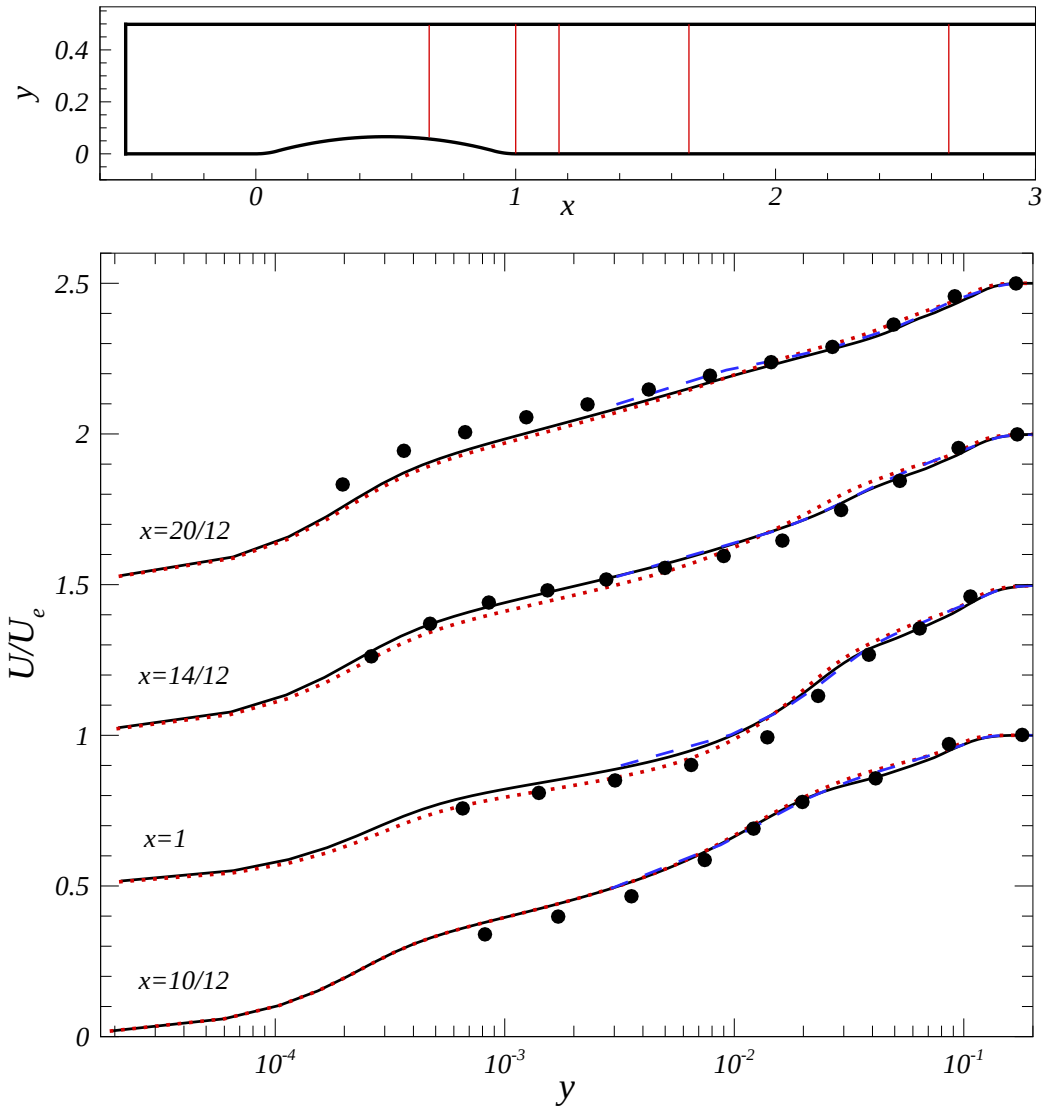

Figure 5.14: Mean horizontal velocity profile. — Log law; ····· WMLES; ——— WMLES with stochastic forcing; • Experiments.

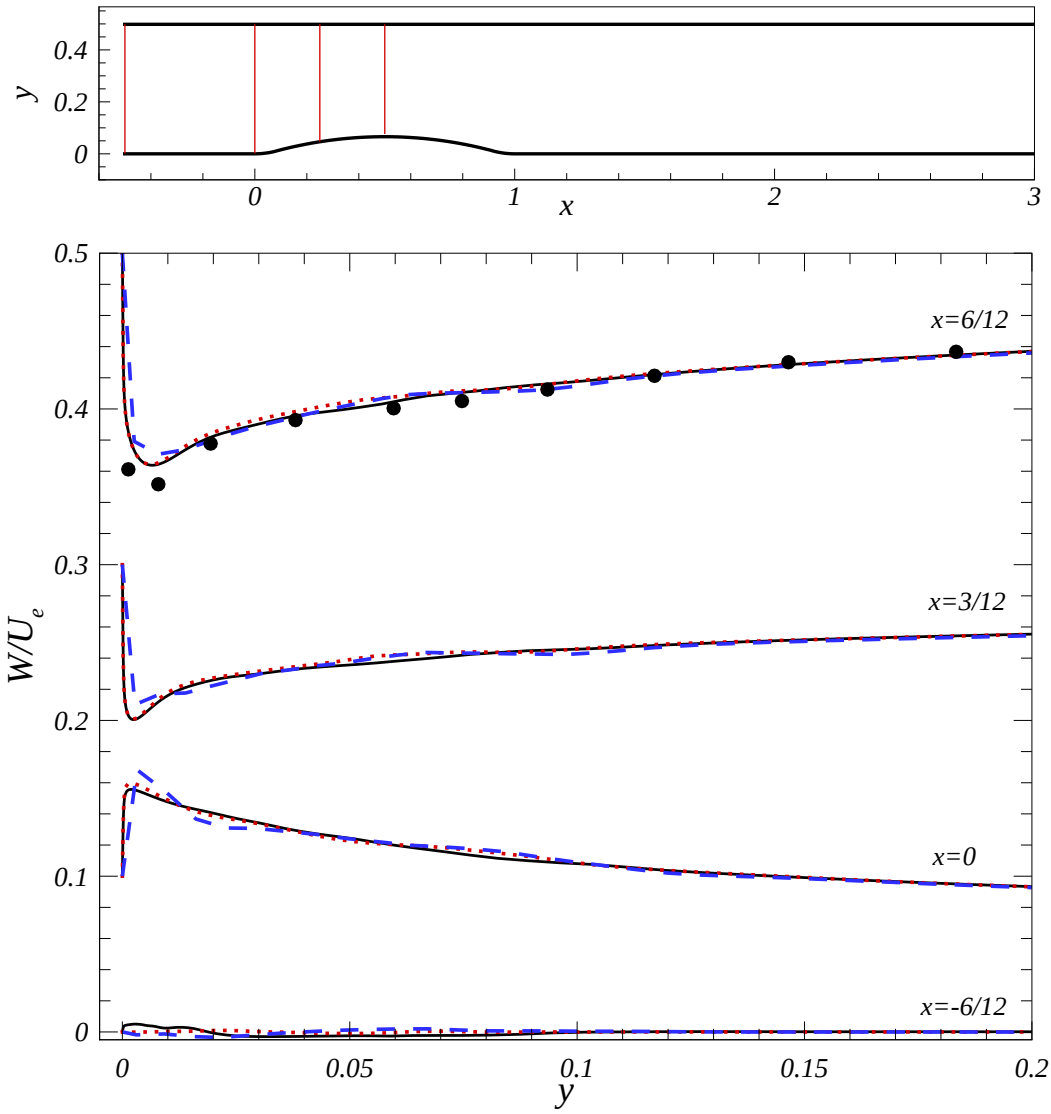

Figure 5.15: Mean spanwise velocity profile. Log law; WMLES; WMLES with stochastic forcing; • Experiments.

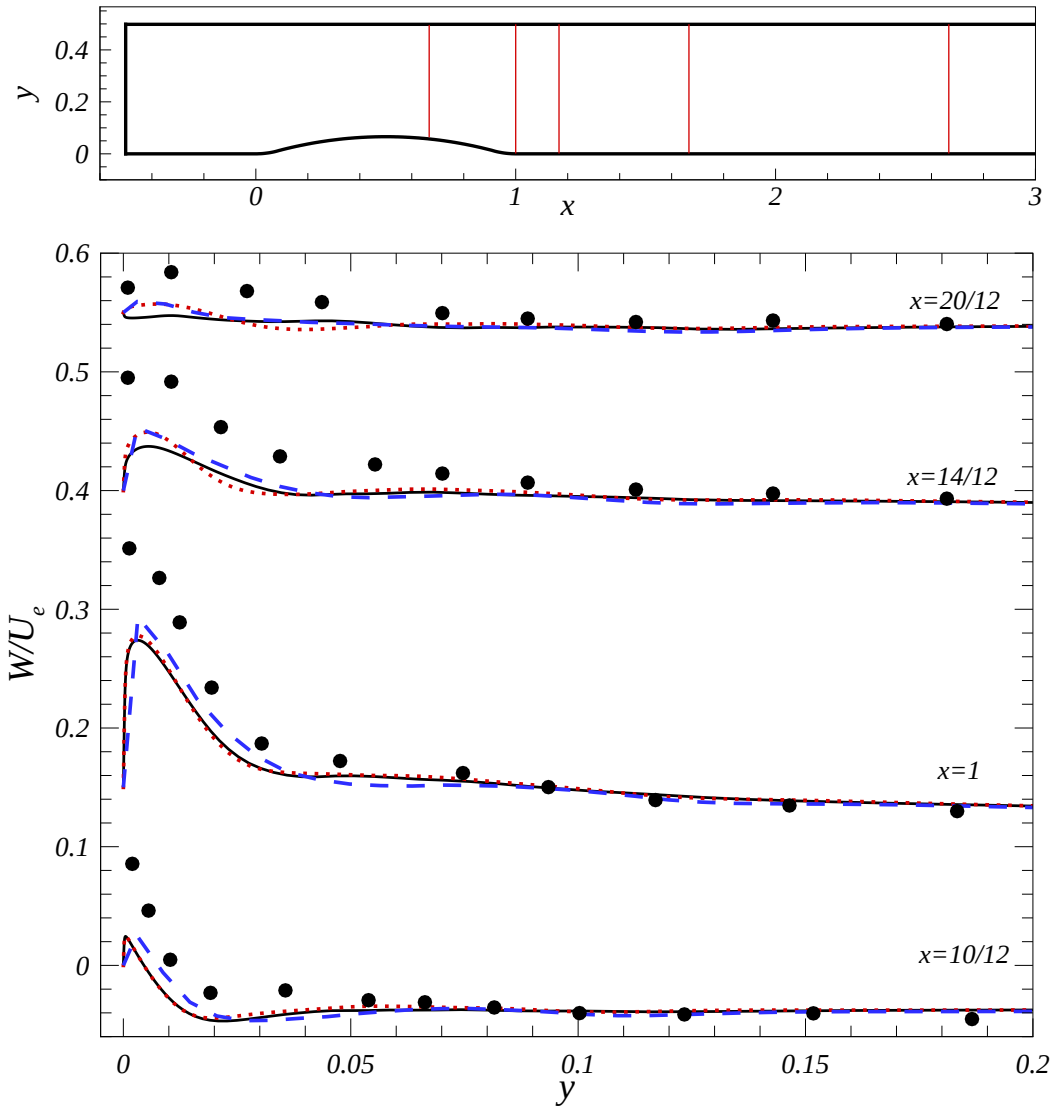

Figure 5.16: Mean spanwise velocity profile. Log law; WMLES; WMLES with stochastic forcing; • Experiments.

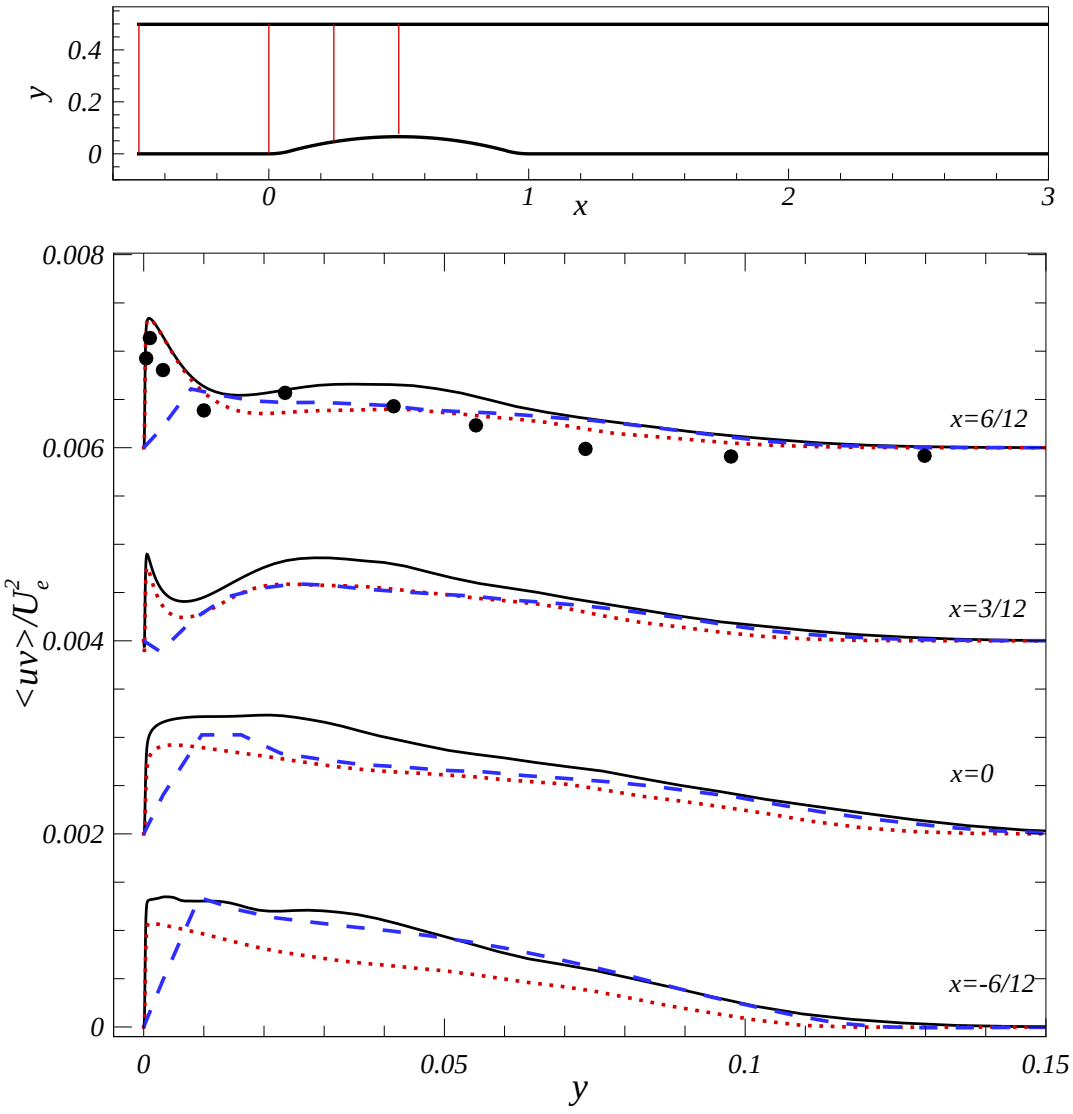

Figure 5.17: Total (modeled + resolved) Reynolds shear stress profile ▬ Log law; ▬ WMLES; ▬ WMLES with stochastic forcing; ● Experiments.

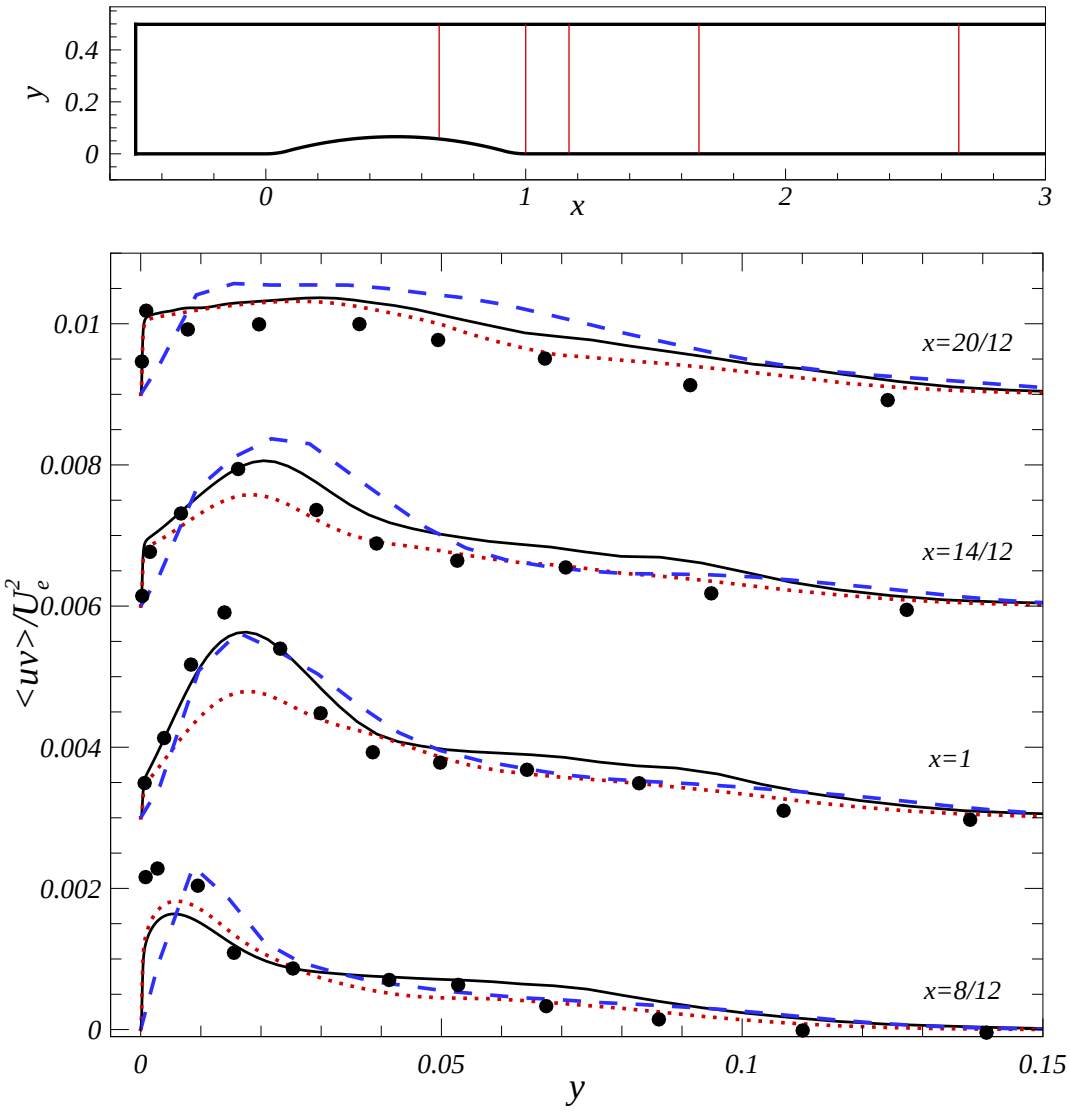

Figure 5.18: Total (modeled + resolved) Reynolds shear stress profile — Log law; ····· WMLES; —— WMLES with stochastic forcing; • Experiments.

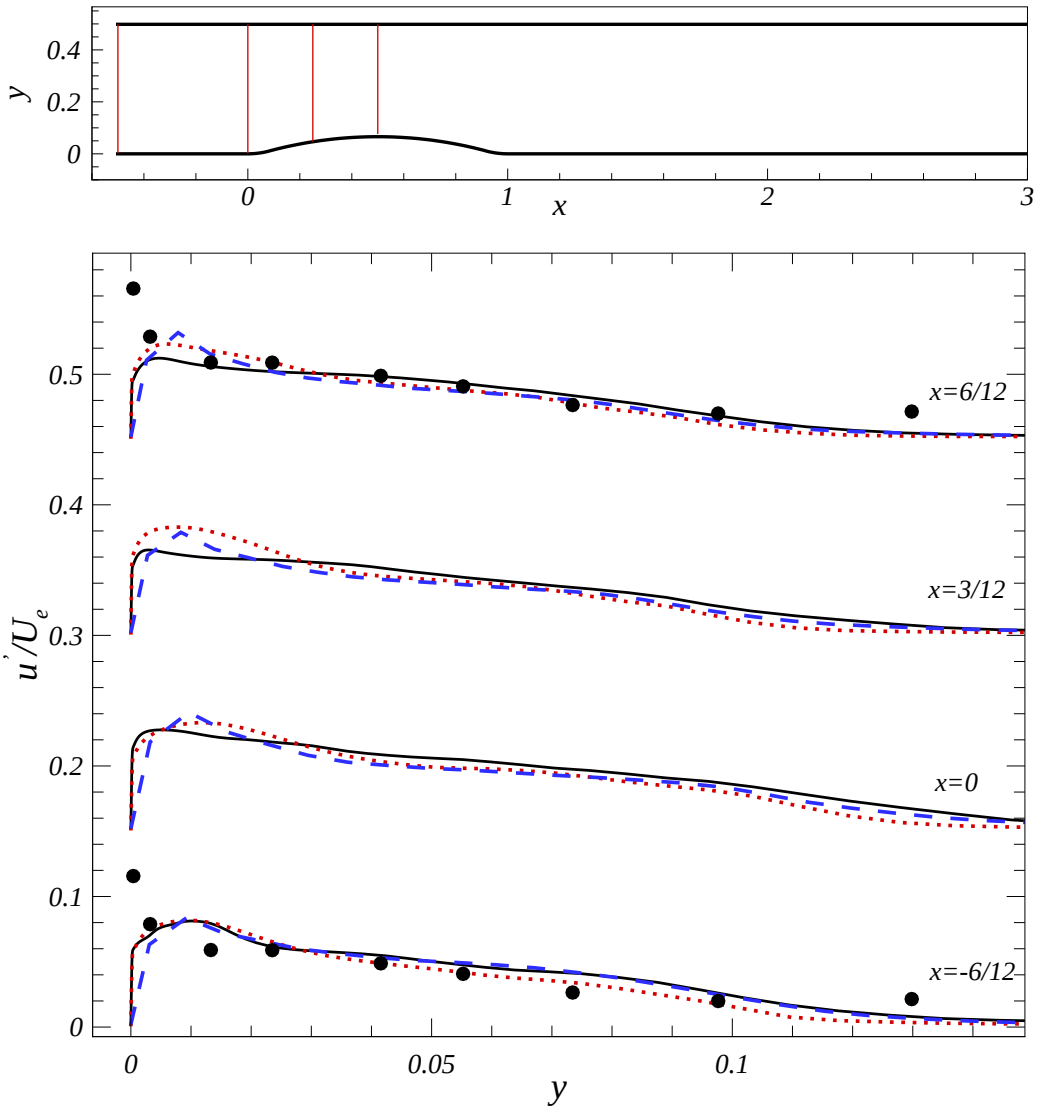

Figure 5.19: RMS of u velocity fluctuation — Log law; ····· WMLES; ——— WMLES with stochastic forcing; • Experiments.

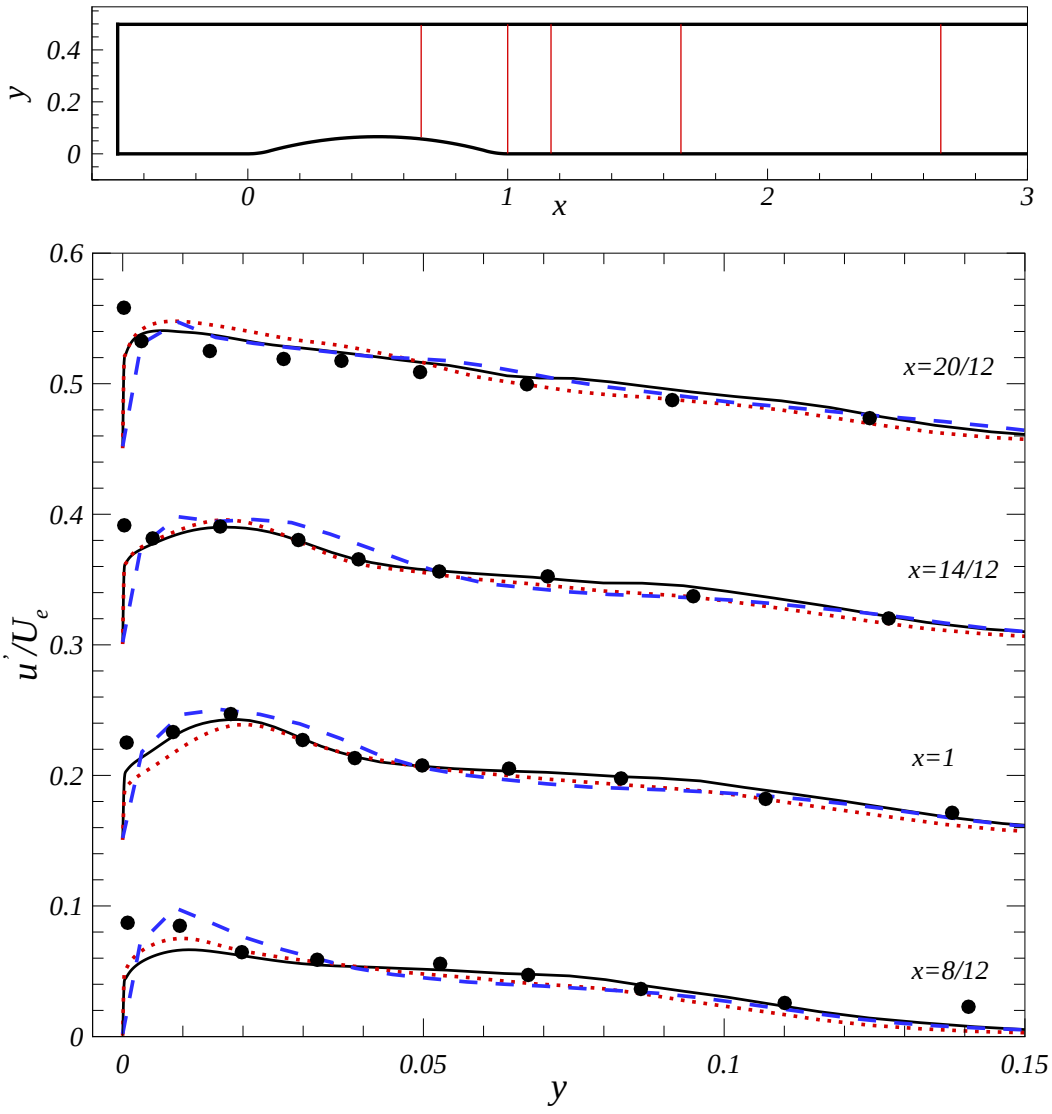

Figure 5.20: RMS of u velocity fluctuation — Log law; ····· WMLES; ——— WMLES with stochastic forcing; • Experiments.

in good prediction of the flow field by both the WMLES calculations. LES based on the log-law boundary condition, which is designed to give accurate prediction in equilibrium flows, also showed good prediction as the non-equilibrium effects due to the pressure gradients is smaller in this case compared to the ramp problem.

Chapter 6

Turbulent oscillating boundary layer

This chapter presents results from numerical simulations of a turbulent oscillating boundary layer on a flat plate. Simulations were performed for a Stokes Reynolds number of 3600 on smooth- and rough-wall and the results are compared to the measured values from Jensen *et al.* [55] experiments.

6.1 Introduction

The boundary layer driven by an oscillating freestream has important applications, both in engineering and in the earth sciences. An example of the latter is the wave-induced boundary layer near the sea floor, which affects sediment transport and mixing of biological material near the bottom ([47]); an understanding of the physical features of the turbulent flow in these regions is of critical importance.

This flow has an exact solution in the laminar regime (a trivial extension of Stokes' second problem, [128]), characterized by an oscillating part confined to a layer of thickness $\delta_s = (2\nu/\omega)^{1/2}$ (where ν is the kinematic viscosity, $\omega = 2\pi/T$ the frequency of oscillation and T its period), sometimes referred to as the "Stokes-layer thickness". An important feature of this exact solution is the fact that the wall shear stress, τ_w, is out of phase with the freestream velocity, U_∞, the wall stress leading

the freestream velocity by 45^0.

On the basis of experimental studies ([51, 115, 55, 106]) and on direct numerical simulations (DNS) of the Navier-Stokes equations ([2, 126, 134, 135]), four flow-regimes can be identified based on the Reynolds number $Re_\delta = \delta_s U_{om}/\nu$ (where U_{om} is the amplitude of the freestream velocity):

1. The laminar regime, in which all disturbances are damped ($Re_\delta < 100$).

2. A disturbed laminar regime, in which finite-amplitude perturbations are maintained, superposed on the laminar solution ($100 < Re_\delta < 550$).

3. An intermittently turbulent regime, in which the flow is turbulent during part of the cycle ($550 < Re_\delta < 1800$).

4. A fully turbulent regime, in which turbulence is maintained through most of the cycle ($3500 > Re_\delta > 1800$) or all of it ($Re_\delta > 3500$).

The last two regimes are of particular interest to the oceanographic community, since the wave-induced boundary layer is usually characterized by values of Re_δ in the range $500 - 3000$.

Akhavan *et al.* [1] performed experiments to study the turbulent oscillating boundary layer in a circular pipe and presented results in the intermittently turbulent regime. They observed that the turbulence appears explosively towards the end of the acceleration stage and is sustained during the deceleration stage. They showed that the mean velocity satisfies the log-law during the deceleration stage

where the flow is turbulent. They also showed that the production of turbulence is reduced during the acceleration stage and the mean velocity agrees with the laminar profile.

Sarpkaya [106] performed experiments to investigate the formation of low-speed streaks and coherent structures in the disturbed laminar and the intermittently turbulent regime. Their experiments showed that at $Re_\delta = 400$, few low-speed streaks form at the late deceleration stage and they disappear during the acceleration stage; no hairpin vortices are formed at this Reynolds number. Between $Re_\delta = 780 - 880$, the phase lead of the wall-stress over the freestream velocity decreases to 13^0. Their flow visualization in the intermittently turbulent regime showed the formation of streaks and its subsequent break up, leads to the generation of coherent structures such as arches, hairpins etc.

Spalart [126] investigated numerically the flow in the intermittently turbulent regime (at $Re_\delta = 1000$). They performed direct numerical simulations (DNS), in which the Navier-Stokes equations are discretized and solved on a grid fine enough to resolve the dissipative scales of motion, the Kolmogorov scales, and also obtained numerical solutions of the Reynolds-Averaged Navier-Stokes (RANS) equations with a one-equation turbulence model. They developed a theory to relate the wall stress to the freestream velocity, and tested it using the DNS data in the intermittently turbulent regime, and the RANS results in the fully turbulent case. They report reasonable agreement between the simulations and the theory, and present phase-

averaged DNS results for the $Re_\delta = 1000$ case (the streamwise velocity, the Reynolds stresses and their budgets).

Vittori and Verzicco [135] performed direct numerical simulation in the disturbed laminar regime and the intermittently turbulent regime to study the transition of flow to turbulence. Their bottom wall was not flat but 'imperfect' and defined by a wavy profile. They showed that in the disturbed laminar regime, the flow field is two-dimensional and periodic; the kinetic energy of the disturbance depends on the Reynolds number and also on the magnitude of the imperfection of the bottom wall profile. In the intermittently turbulent regime, the kinetic energy of the disturbance depends only on the Reynolds number.

Hsu *et al.* [53] performed LES of the oscillating boundary layer in the intermittently turbulent regime using the dynamic subgrid-scale (SGS) eddy-viscosity model ([44, 71]) to parameterize the unresolved, subgrid-scale (SGS) stresses, as well as solutions of the RANS equations with a $k - \omega$ (ω here represents the vorticity) model ([104]). They present phase-averaged velocity and Reynolds stress profiles, and obtain good agreement between the RANS and LES predictions.

Lohmann *et al.* [72] performed LES of an ventilated oscillating boundary layer (*i.e.*, a boundary layer with flow through the bottom boundary, such as would occur in a porous medium) in the fully turbulent regime using the classical Smagorinsky ([116, 70]) SGS model. They also report the results of a case without transpiration velocity that matches one of the cases studied experimentally by [55]. The grid

spacing they used, however, was insufficient to resolve the near-wall eddies, and resulted in an incorrect prediction of the time evolution of the wall shear stress and of the statistical quantities.

Salon *et al.* [105] performed simulations of the oscillating boundary layer in the turbulent regime, for $Re_\delta = 1790$ (Case 8 in the study by Jensen *et al.* [55]). Their simulations used the Dynamic Mixed Model ([143, 136]) in the contravariant form of Armenio and Piomelli [4]. They used a finer grid than that used by Lohmann *et al.* [72], and were able to resolve the near-wall structures. They obtained very good agreement with the experiment on all statistical data (except on the turbulence intensities during the part of the cycle where the flow changes direction—an issue that will be discussed later), and investigated the evolution of the flow structures, observing significant qualitative differences between the near-wall and the outer-layer behavior.

The accuracy of wall-layer models for oscillating flows is one of the focuses of this investigation, which aims to validate the LES model for high-Reynolds number oscillating flows using advanced SGS models and approximate wall-layer treatments. Since roughness is often an important feature of geophysical flows, its inclusion in the approximate wall treatment will be investigated.

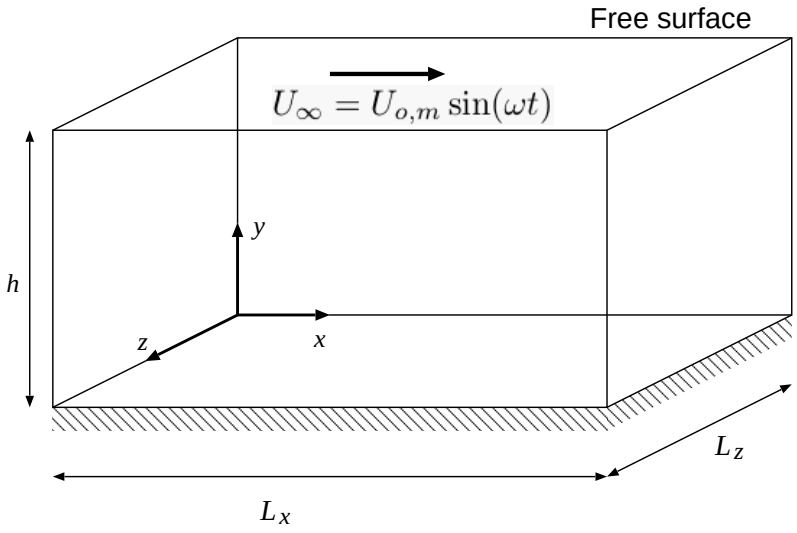

Figure 6.1: Sketch of the physical configuration.

6.2 Problem formulation

The computational configuration is sketched in Figure 6.1. The calculations are carried out in a Cartesian domain. Periodic boundary conditions are used in the streamwise (x) and spanwise (z) directions. At the freestream, the wall-normal velocity is set to zero, as are the vertical derivatives of the streamwise and spanwise velocity components. The flow is driven by a periodic pressure gradient $f = A\cos(\omega t)$ in the streamwise direction, which results in a sinusoidal variation of the freestream velocity, $U_\infty = U_{om}\sin(\omega t)$ with $U_{om} = A/\omega$. The amplitude A and frequency ω are set to match the experimental [55] parameters. The results from the simulations are compared to the experimental data by Jensen *et al.* [55], which were obtained in a rectangular duct driven by an oscillating pressure gradient. In the experiments, the oscillation period was maintained constant at $T = 9.72$s (giving a thickness of

the Stokes layer, $\delta_s = (2\nu/\omega)^{1/2} = 1.8 \times 10^{-3}$m); the pressure-gradient amplitude was varied to achieve a wide range of Reynolds numbers, spanning the disturbed laminar, intermittently turbulent and fully turbulent regimes. In the present work, simulations are performed for two cases reported in Jensen *et al.*

1. Case 10: the flow is turbulent, with $Re_a = 6 \times 10^6$ (based on U_{om} and on the amplitude of the freestream motion $a = U_{om}/\omega$) and $Re_\delta \simeq 3600$. At this Reynolds number the velocity satisfies a logarithmic law through most of the cycle.

2. Case 13: the flow conditions are the same as those of Case 10, but a rough wall is used. The equivalent sand roughness (normalized by the maximum friction velocity $u_{\tau m}$) is $k_{sm}^+ = 84$, corresponding to $k_o = 0.0277$mm.

Calculations are performed with the WMLES (without the stochastic forcing) and with various other subgrid scale models using approximate boundary condition based on log-law and its variants. For the ramp and bump problem studied in previous chapters, the flow field predicted by the WMLES always showed better agreement with the measured values from experiments when stochastic forcing was applied. The application of the stochastic forcing requires continuous averaging of the flow field on short time intervals (roughly a fraction of the eddy turn over time) so that the controller can update the magnitude of the stochastic forcing; the initial transient in this type of simulation is also long since the controller has to reach the appropriate magnitude of the stochastic forcing starting from zero. In

flows where the statistics are not stationary in time, such as the one studied here, continuous time averaging cannot performed. A method to apply the stochastic forcing based on the dynamic controller would have been, perhaps, to define multiple controllers that are active during different phases of the time period; this would have required the simulation to be run for many time periods before controllers predict stable values of the stochastic forcing. The computational resources needed for this type of simulation is not available, therefore, the WMLES calculation was performed without the application of the stochastic forcing. The different versions of the approximate boundary conditions tested are described below.

The simplest approximate boundary condition is based on the existence of an equilibrium layer which results in a logarithmic law ([32, 107, 48, 97]). Knowing the average velocity in the outer layer (and, in particular, at the first grid point), the friction velocity u_τ can be calculated by solving

$$U_{ol}^+ = \frac{U_{ol}}{u_\tau} = \frac{1}{\kappa} \log \frac{y_{ol} u_\tau}{\nu} + B \tag{6.1}$$

where the subscript ol indicates the first grid point in the outer layer, and $U_{ol} = \langle \overline{u}_{ol} \rangle_{xz}$ is the velocity at the first outer-layer point averaged over an $xz-$plane. The von Kàrmàn constant κ is generally taken to be 0.41, and $B \simeq 5.0 - 5.5$ (we used the value 5.0). The logarithmic law (6.1) is matched to a linear law $U_{ol}^+ = y_{ol}^+$ for $y_{ol}^+ < 11$ to account for low-Reynolds number effects that may occur near flow reversal.

Once the plane-averaged stress $\langle \tau_w \rangle = \rho u_\tau^2$ is known, the following boundary conditions is applied for the streamwise and spanwise components of the wall stress,

and the wall-normal velocity:

$$\tau_{w,x}(x,z,t) = \left[\frac{\langle\tau_w\rangle_{xz}}{U_{ol}}\right]\overline{u}(x,y_{ol},z,t) \tag{6.2}$$

$$v(x,0,z,t) = 0 \tag{6.3}$$

$$\tau_{w,z}(x,z,t) = \left[\frac{\langle\tau_w\rangle_{xz}}{U_{ol}}\right]\overline{w}(x,y_{ol},z,t) \tag{6.4}$$

where the dependence of U_{ol} and $\langle\tau_w\rangle$ on time is omitted.

This approach can also be used for rough-wall boundary layers. In this case the logarithmic law (6.1) can be replaced with one of the following formulations (see the review by Jimenez [56]):

$$\frac{\overline{U}_{ol}}{u_\tau} = \frac{1}{\kappa}\log\frac{y_{ol}}{k_o} \tag{6.5}$$

where k_o is the roughness length, related to the "equivalent sand roughness", k_s, by $k_o = 0.033k_s$.

An alternative way to express (6.5) is

$$\frac{\overline{U}_{ol}}{u_\tau} = \frac{1}{\kappa}\log\frac{y_{ol}u_\tau}{\nu} + B - \Delta U^+. \tag{6.6}$$

This form is particularly useful in transitionally rough cases ($k_s^+ < 4$), in which a correlation due to [26] can be used:

$$\Delta U^+ = \frac{1}{\kappa}\log(1 + 0.26k_s^+). \tag{6.7}$$

Note that in the present application the wall stress is close to zero during part of the cycle: at these times the value of k_s^+ will be necessarily small.

Another modification of the logarithmic law (6.1) was proposed by Marusic *et al.* [76]. Following Piomelli *et al.* [97], they proposed the use of a shift in the

downstream direction between the outer-layer velocity point and the point where the wall stress is calculated. This shift is due to the inclination of the near-wall structures. In addition, Marusic *et al.* [76] suggested separating the mean wall stress from its fluctuating part, which can be multiplied by a constant to match the wall-stress fluctuations better. The model they propose (which will be referred to as "MKP model") replaces (6.2) and (6.4) with

$$\begin{aligned} \tau_{w,x}(x,z,t) &= \langle \tau_w \rangle_{xz} \\ &\quad + \alpha_\tau u_\tau \left[\overline{u}(x+\Delta_s, y_{ol}, z, t) - U_{ol} \right] \qquad (6.8) \\ \tau_{w,z}(x,z,t) &= \alpha_\tau u_\tau \overline{w}(x+\Delta_s, y_{ol}, z, t). \qquad (6.9) \end{aligned}$$

Here, α_τ is a constant (the value 0.10 was suggested by Marusic *et al.* to match the spectrum of τ_w given by (6.8) with the experimental one). Following Piomelli *et al.* [97], they recommend $\Delta_s = y_{ol} \cot 13^0$ for $y_{ol}^+ > 60$.

Most of the data shown in the following is averaged over planes parallel to the wall and ensemble-averaged according to

$$\langle f \rangle = \frac{1}{N} \frac{1}{L_x L_y} \sum_1^N \int_0^{L_x} \int_0^{L_z} f(x, y, z, \phi + n\pi) dx dz \qquad (6.10)$$

where ϕ is the phase. The symmetry (or antisymmetry) of the flow between phases ϕ and $\phi + \pi$ is also exploited to double the sample size. For all calculations, an initial transient of at least 5 periods was discarded, and statistics were accumulated over the next 5 periods.

6.3 Oscillating boundary layer on a smooth wall

The calculations of case 10 are summarized in Table 6.3. Four subgrid scale models were tested: SA in WMLES mode, Smagorinsky, Lagrangian Dynamic Eddy Viscosity (LDEV) and Scale-Dependent Lagrangian Dynamic Eddy Viscosity (SDLDEV), (cases 101 through 104). Two types of boundary conditions were tested: the standard logarithmic law and the MKP modification (cases 103 and 105). The grid convergence of the results are evaluated with cases 104 and 106. In the SA WMLES calculation the grid is uniform in x and z, but stretched in y so that the first grid point always occurs at $y^+ \leq 1$; in the other cases the grid is uniform in all directions up to half of the domain size, and then stretched in the outer layer. This results in grid cells that, near the wall, are cubic with grid size 6mm for the coarse grid (the domain size is 0.71m×0.23m×0.35m), and 3mm in the fine one.

A time-history of the wall stress is shown in Figure 6.2. All models predict the wall-stress development reasonably well. With the WMLES the phase-shift between the wall stress and the freestream velocity (approximately 7^0 in the experiments) is slightly over-predicted. The simulations using dynamic models slightly over-predict the peak wall stress by 6%. The use of the MKP model improves the prediction of the wall stress to within 3% of the experimental data. A comparison between the coarse and fine-mesh results with the SDLDEV model indicates that the fine grid predicts phase-shift between the wall stress and the freestream velocity better.

It is not surprising that the simple logarithmic law boundary condition gives

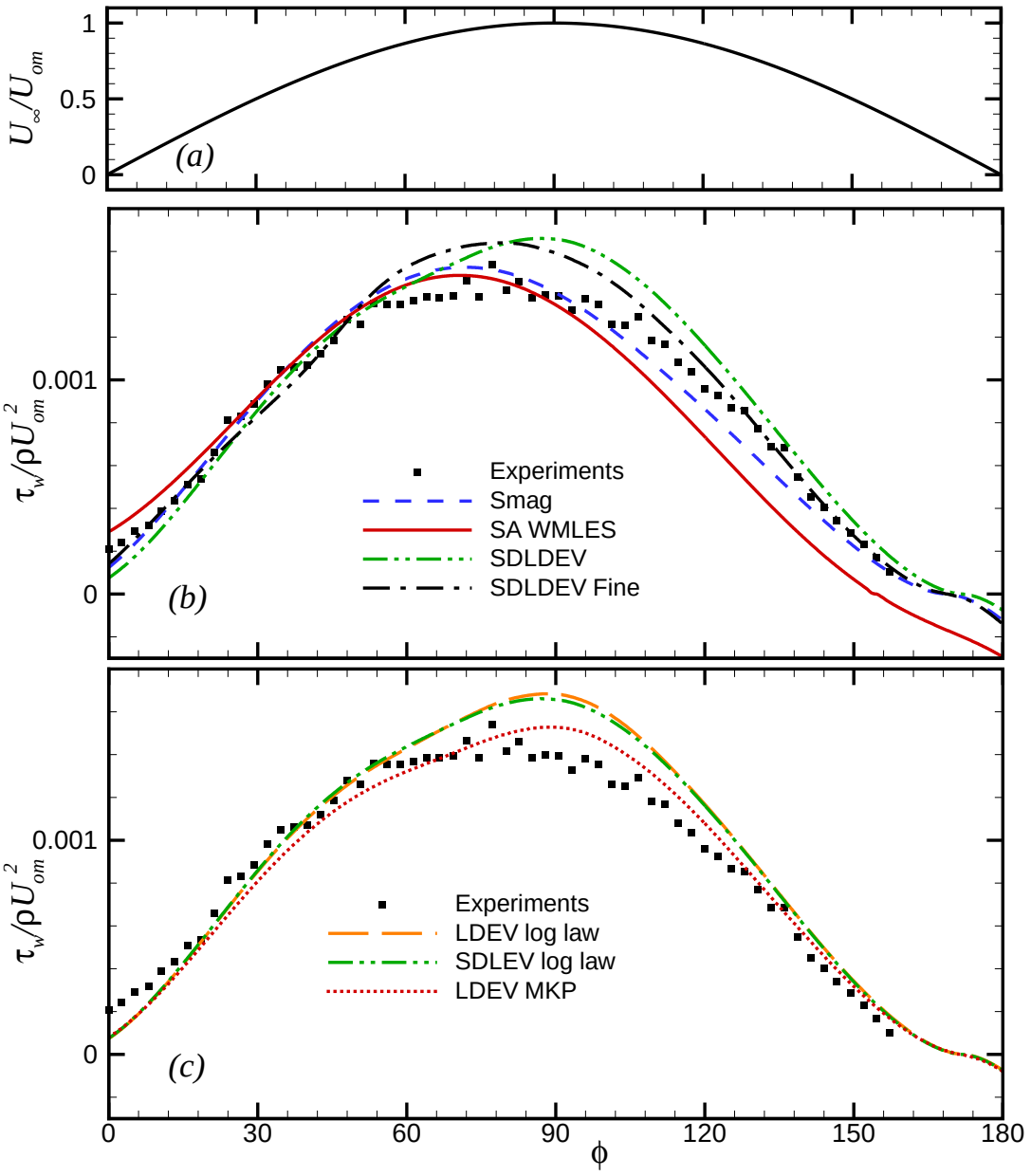

Figure 6.2: Wall stress as a function of phase. *(a)* Freestream velocity; *(b)* Cases 101–104 and 106; *(c)* cases 103 and 105.

	Domain	Grid	Wall model	SGS Model
101	384×128×192	144×144×96	No-slip	SA
102	384×128×192	120×32×60	Log law	Smag
103	384×128×192	120×32×60	Log law	LDEV
104	384×128×192	120×32×60	Log law	SDLDEV
105	384×128×192	120×32×60	MKP	LDEV
106	384×128×192	240×80×120	Log law	SDLDEV

Table 6.1: Summary of Case 10 calculations. The domain size is normalized by Stokes layer thickness, δ_s. The logarithmic law used is given by (6.1).

good results, since it is known from the experimental data that a logarithmic law exists between $\phi = 15^0$ and 170^0 ([55]). One intrinsic limitation of LES that use wall-layer models, however, is the fact that at the first grid point the grid size (which is of the order of the distance of the first point to the wall, y_{ol}) is not much smaller than the integral scale of the flow, κy_{ol}. One, therefore, expects a larger error in the LES predictions at the first few grid points; how far this error propagates into the core of the flow is an important measure of the accuracy of a particular model. Cases 103-105 which used the same grid but different versions of dynamic model and different approximate boundary condition gave very similar results, therefore, results from case 104 are only shown. Note, although the MKP model (case 105) predicted wall-stress in better agreement with experiments compared to the log-law

boundary condition (case 103 and 104), the flow field prediction from all three cases agree with each other away from the wall.

The WMLES predicts the mean velocity profile incorrectly throughout the layer. Near the wall, there is a significant momentum deficit during the deceleration phase, while the velocity is over-predicted at the beginning of the acceleration, probably due to the excessive SGS eddy viscosity predicted by the model (Figure 6.4). The Smagorinsky model results in a similar behavior, although less drastic, as the viscosity it predicts is slightly lower. The dynamic models give better agreement with the experiments. They predict lower viscosity in the near-wall region, and a somewhat higher one away from the wall. The agreement of the simulations that use the dynamic model is better in the near-wall region than in the outer flow; differences between the experimental and numerical setup (the finite-size duct used in the experiment, for instance) may result in differences in the freestream velocity between the simulation and experimental data even if the pressure gradient imposed (and, therefore, the nominal free-stream velocity) is the same.

Instantaneous picture of the flow for the simulation that used the scale-dependent Lagrangian Dynamic Eddy-Viscosity model (SDLDEV) are shown in Figure 6.5 by isosurfaces of the second invariant of the velocity gradient tensor, Q:

$$Q = \frac{1}{2}\left(\overline{\Omega}_{ij}\overline{\Omega}_{ij} - \overline{S}_{ij}\overline{S}_{ij}\right); \tag{6.11}$$

positive values of this quantity highlight regions of high vorticity in which the rotational motion is stronger than the shear; Q is, therefore, one of the criteria most

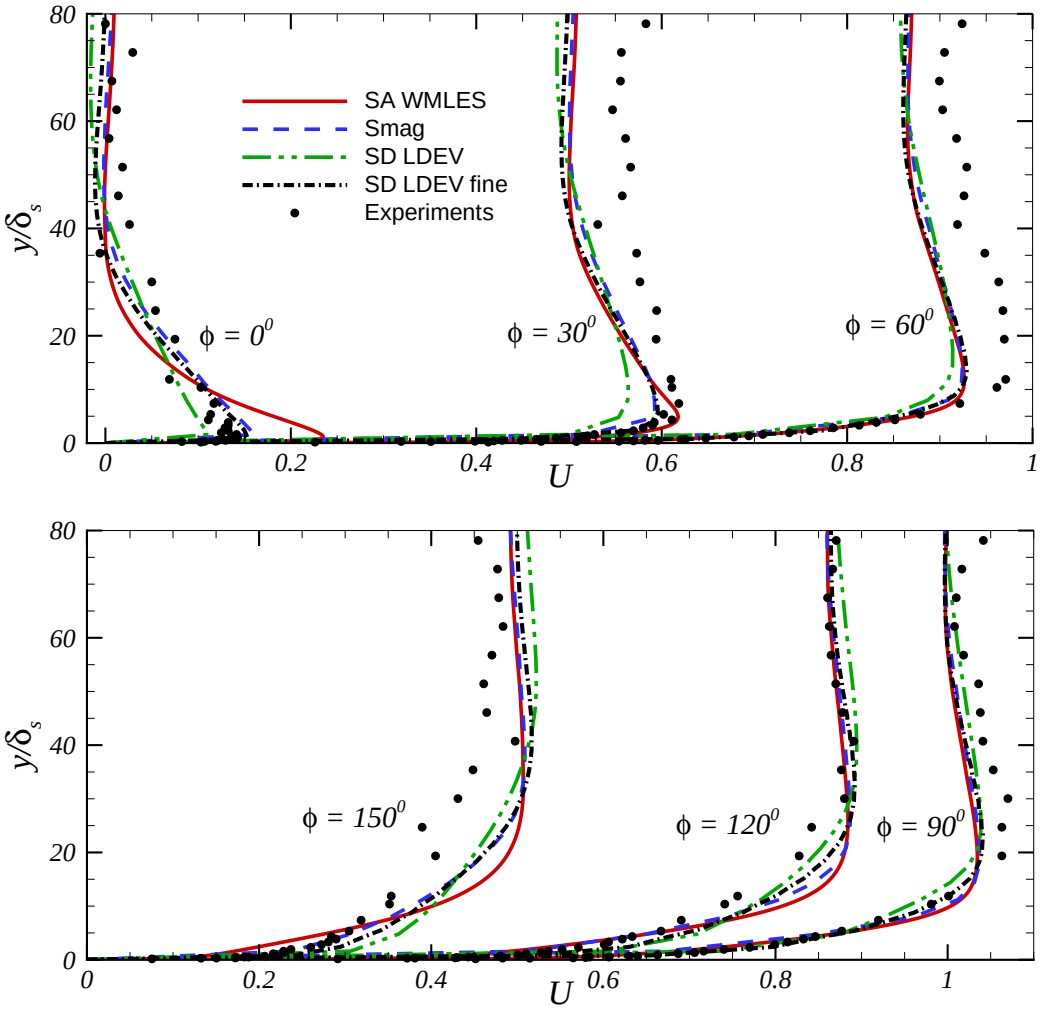

Figure 6.3: Mean velocity profiles, smooth wall. *(a)* $\phi = 0^0$, 30^0 and 60^0; *(b)* $\phi = 90^0$, 120^0 and 150^0.

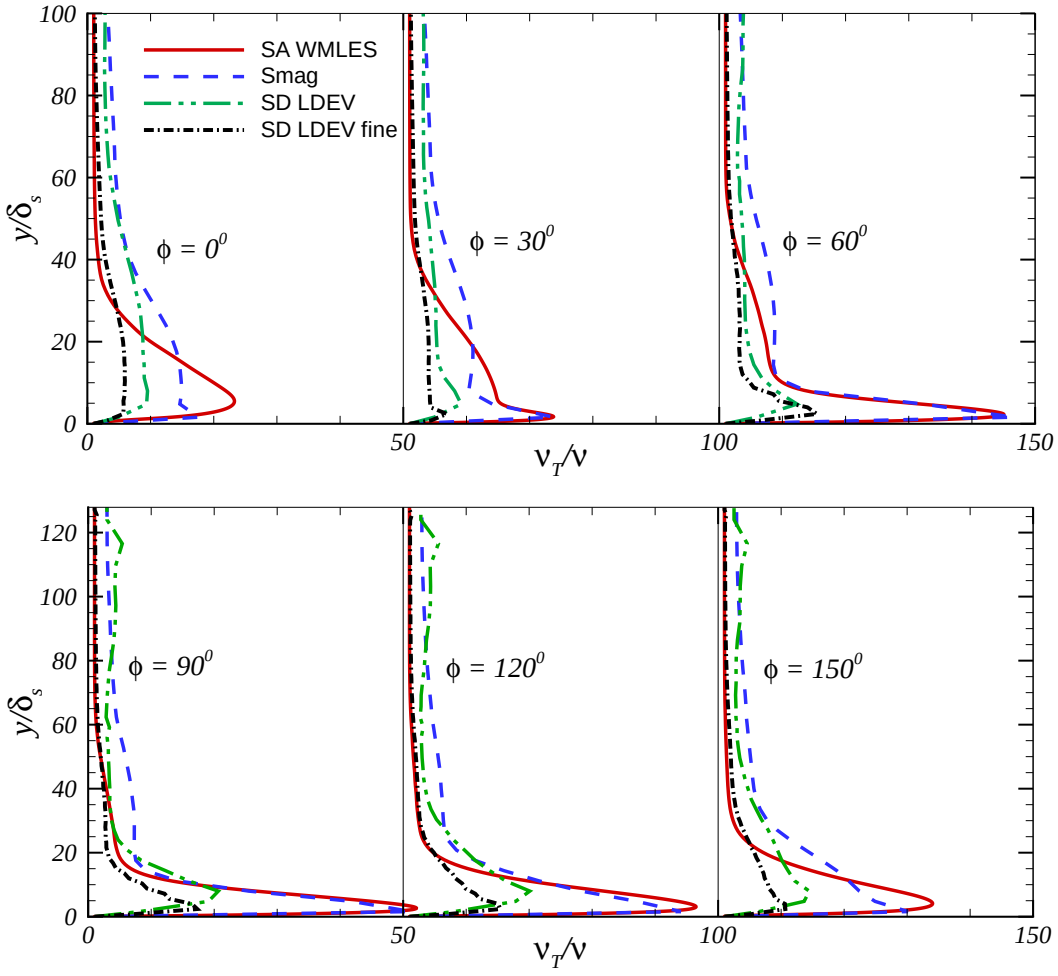

Figure 6.4: Subgrid-scale eddy viscosity, smooth wall. *(a)* $\phi = 0^0$, 30^0 and 60^0; *(b)* $\phi = 90^0$, 120^0 and 150^0. Each profile is shifted by 50 units horizontally for clarity.

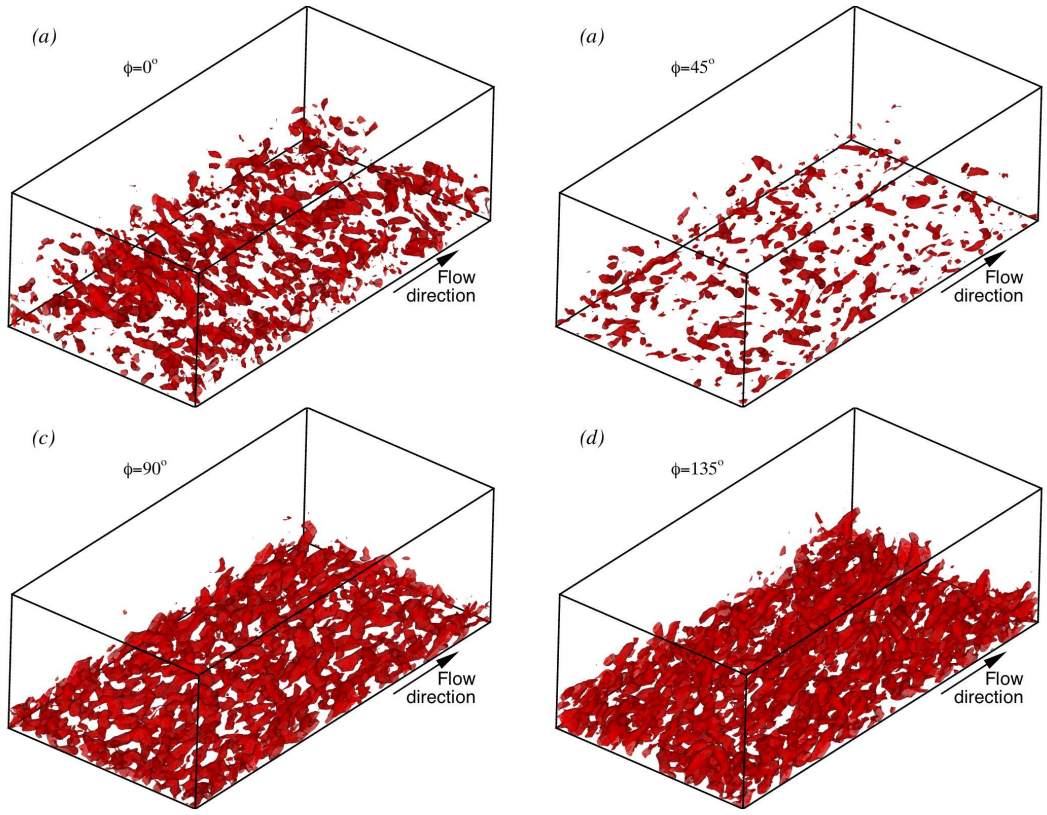

Figure 6.5: Instantaneous isosurfaces of $Q = 1$ [Q is defined in equation (6.11)]. Case 104: smooth wall, SDLDEV SGS model with logarithmic boundary conditions. *(a)* $\phi = 0^0$; *(b)* $\phi = 45^0$; *(c)* $\phi = 90^0$; *(d)* $\phi = 135^0$.

commonly used for vortex identification ([54, 38]). During the acceleration phase, the turbulent eddies are damped initially, then followed by their rapid regeneration as the freestream velocity becomes approximately constant. During the deceleration phase, a realistic distribution of hairpin vortices can be seen, with a predominance of "heads" ([103]), as expected in the outer layer of a wall-bounded flow.

Figure 6.6 shows the time-development of the SGS eddy viscosity. It can be seen that it remains nearly constant during the acceleration, and grows explosively

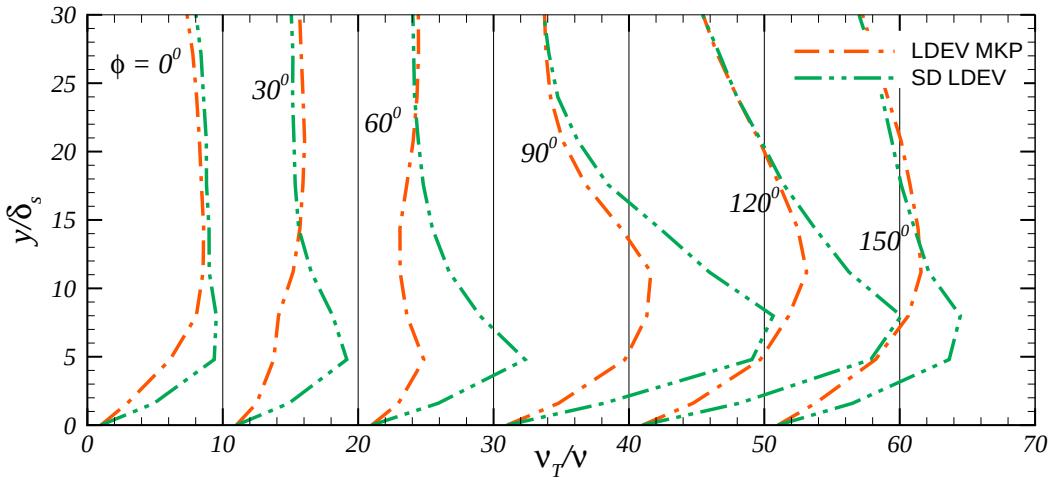

Figure 6.6: Subgrid-scale eddy viscosity, smooth wall. Cases 105 (LDEV model) and 104 (SDLDEV model) with logarithmic law boundary conditions. Profiles are shifted by 10 units for clarity.

at the end of the acceleration and during the deceleration, reflecting the generation of turbulent eddies shown in Figure 6.5. The Scale-Dependent Lagrangian Dynamic Eddy-Viscosity model (SDLDEV) predicts a larger SGS eddy viscosity than the single-coefficient version (LDEV) in the near-wall region, but the mean velocity is not significantly affected.

Profiles of the streamwise and wall-normal turbulence intensities, u_{rms} and v_{rms} are shown in Figures 6.7 and 6.8. The WMLES model does not predict the intensities well even qualitatively. The dynamic models, on the other hand, give better agreement with the experimental results near the wall. In the outer layer, the agreement is very good at $\phi = 60^0$ and 90^0, less so at the other phases. The experimental data consistently shows higher values of the turbulence intensity than

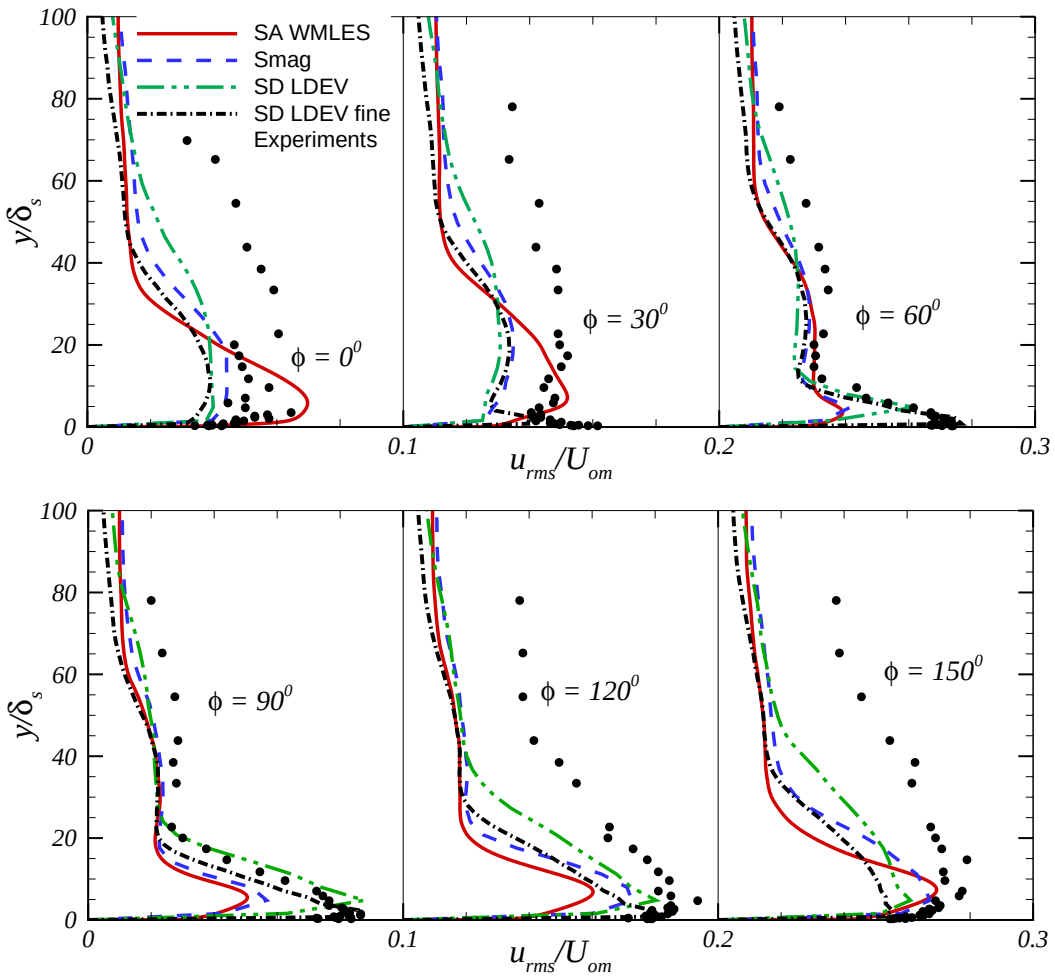

Figure 6.7: Streamwise turbulence intensity, smooth wall. *(a)* $\phi = 0^0$, 30^0 and 60^0; *(b)* $\phi = 90^0$, 120^0 and 150^0. Each profile is shifted by 0.1 units horizontally for clarity.

the LES. This difference was observed in other modeling studies as well ([77, 105]). Mellor [77] attributes the high levels of turbulence in the outer layer measured by Jensen *et al.* [55] to the fact that, at this Reynolds number, some fluid particles are carried out of the test section and into the diffuser (where turbulence would be amplified) before returning to the test section. This error would be most significant around $\phi = 0^0$, and least significant around $\phi = 90^0$. Jensen *et al.* [55] remark on this source of error, however, and mention that it does not lead to contamination of the results. The finite size of the duct is also a source of uncertainty: the measurements (for instance the turbulence intensities shown in Figure 26 of Jensen *et al.* [55]) show significant turbulence at $y/a = 0.04$, corresponding to $y = 0.12$m (close to the duct centerline, $y = 0.14$m). Further study is required to determine the reason for the discrepancy between all the simulations and the experiments.

The vertical fluctuations (Figure 6.8) show the same trends. The near-wall behavior is predicted very well by the dynamic model, while in the outer layer the agreement with the experiments is very good between $\phi = 30^0$ and 90^0, and probably affected by configuration differences at the other phases.

6.4 Oscillating boundary layer on a rough wall

The flow condition for this simulation corresponds to Case 13 in Jensen *et al.* [55]. The equivalent sand roughness, $k_{sm}^+ = 84$, corresponds to fully rough conditions through most of the cycle. Only near flow reversal the roughness height in wall

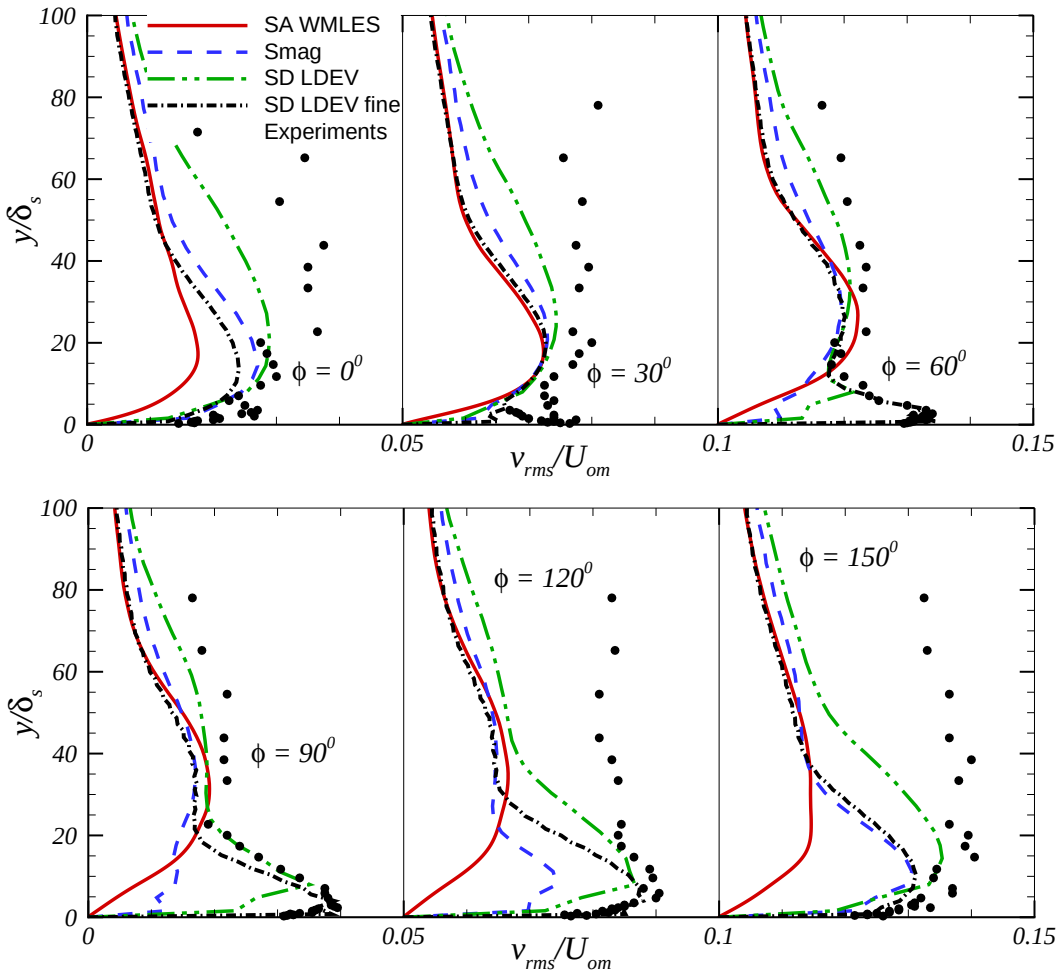

Figure 6.8: Wall-normal turbulence intensity, smooth wall. *(a)* $\phi = 0^0$, 30^0 and 60^0; *(b)* $\phi = 90^0$, 120^0 and 150^0. Each profile is shifted by 0.05 units horizontally for clarity.

	Domain	Grid	Wall model	SGS Model
131	384×128×192	120×32×60	Log law	Smag
132	384×128×192	120×32×60	Log law	LDEV
133	384×128×192	120×32×60	Log law	SDLDEV
134	384×128×192	120×32×60	Colebrook	Smag
135	384×128×192	120×32×60	Colebrook	LDEV
136	384×128×192	120×32×60	Colebrook	SDLDEV

Table 6.2: Summary of Case 13 calculations. The domain size is normalized by Stokes layer thickness, δ_s. The standard logarithmic law is given by (6.5); the Colebrook [26] correlation uses (6.6,6.7).

units decreases so that the flow is transitionally rough. This condition, however, occurs for a very brief time, and transitional roughness effects may not be significant. To investigate whether they are, calculations were performed using the Colebrook [26] correlation, which accounts for these effects. A summary of the calculations of the rough-wall case carried out is in Table 6.2.

The ensemble-averaged velocity profiles are shown in Figure 6.9. All models give similar results; the agreement with the experimental data is comparable to that obtained for the smooth-wall case. The Smagorinsky model again damps the turbulence excessively near the wall (consistent with the findings described in the previous section) due to the excessive levels of SGS eddy viscosity that it predicts.

In general, the effect of the rough wall is to move the peak streamwise velocity away from the wall. Figure 6.10 shows the wall-normal fluctuation intensity, which exhibit a decreased amplification of the vertical fluctuations during late deceleration and early acceleration phase. The LDEV model in this case gives slightly better prediction of the flow statistics. The streamwise fluctuations (Figure 6.11) also show reduced amplification of the turbulence during late deceleration and early acceleration phase. The results obtained with the dynamic models are very similar to each other. The use of the Colebrook [26] correction does not result in significant changes in the results, indicating that transitional-roughness effects may not be important in this case.

6.5 Summary

Large-eddy simulations of a fully turbulent oscillating boundary layer were performed using a variety of subgrid-scale (SGS) stress models and approximate near-wall treatments. Results indicate that dynamic models predict flow development accurately. The simulations showed that the use of models that do not dissipate excessive amounts of energy is crucial. In this flow the acceleration tends to damp turbulent fluctuations, which are then regenerated at the end of the acceleration phase and during deceleration. WMLES and the Smagorinsky model are excessively dissipative and they do not respond quickly enough to the changes caused by the freestream. Dynamic models, on the other hand, predict a much lower SGS

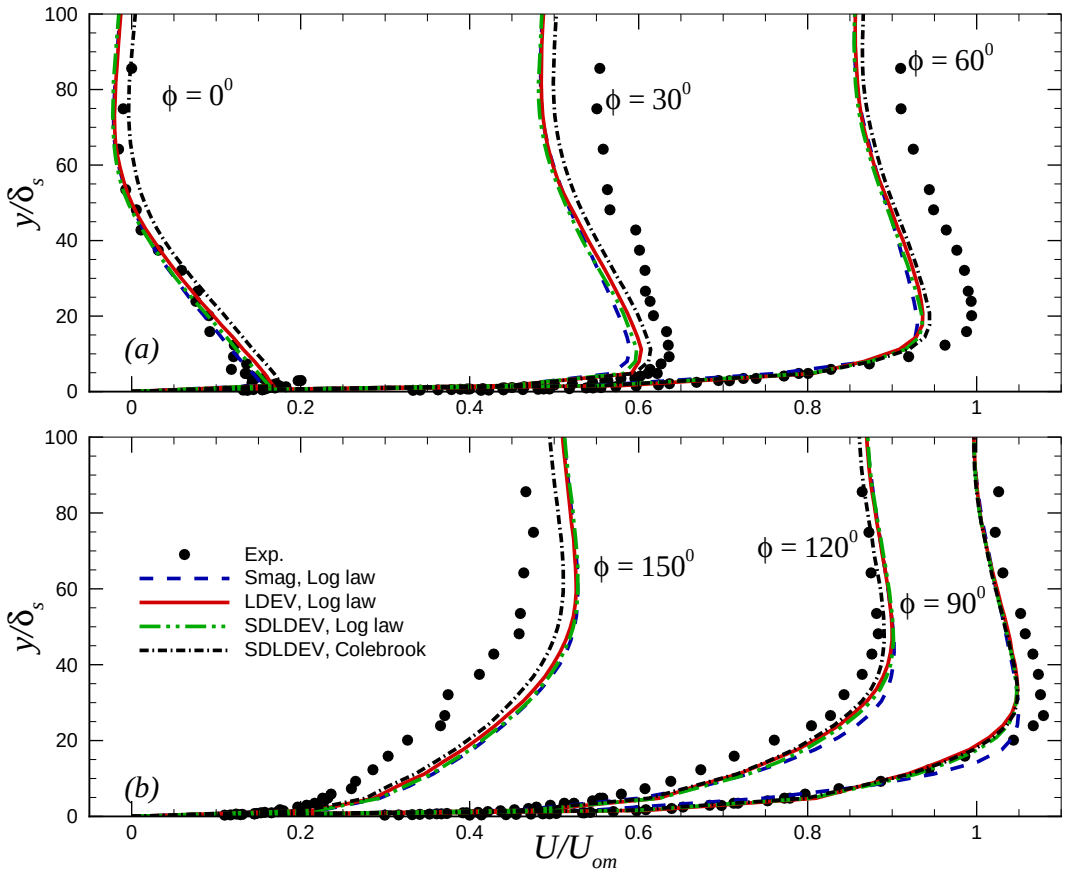

Figure 6.9: Mean velocity profiles, rough wall. *(a)* $\phi = 0^0$, 30^0 and 60^0; *(b)* $\phi = 90^0$, 120^0 and 150^0.

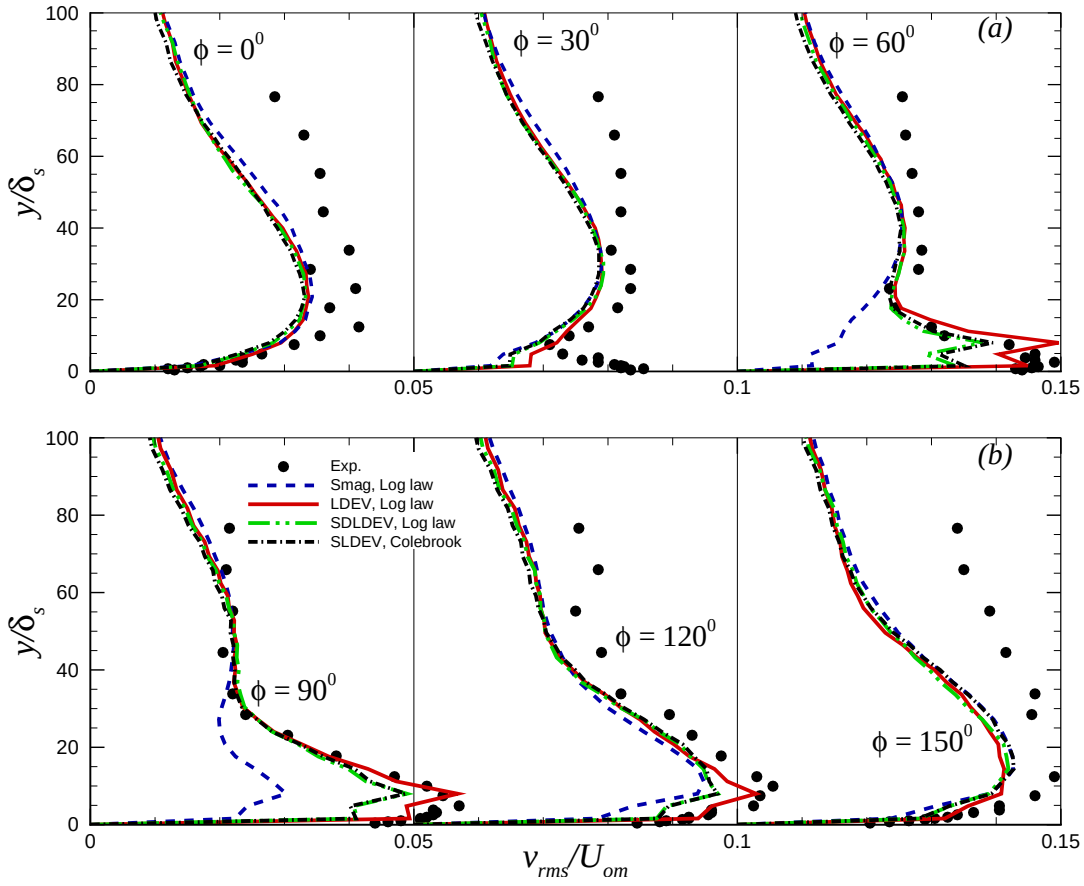

Figure 6.10: Wall-normal turbulence intensity, rough wall. *(a)* $\phi = 0^0$, 30^0 and 60^0; *(b)* $\phi = 90^0$, 120^0 and 150^0. Each profile is shifted by 0.05 units horizontally for clarity.

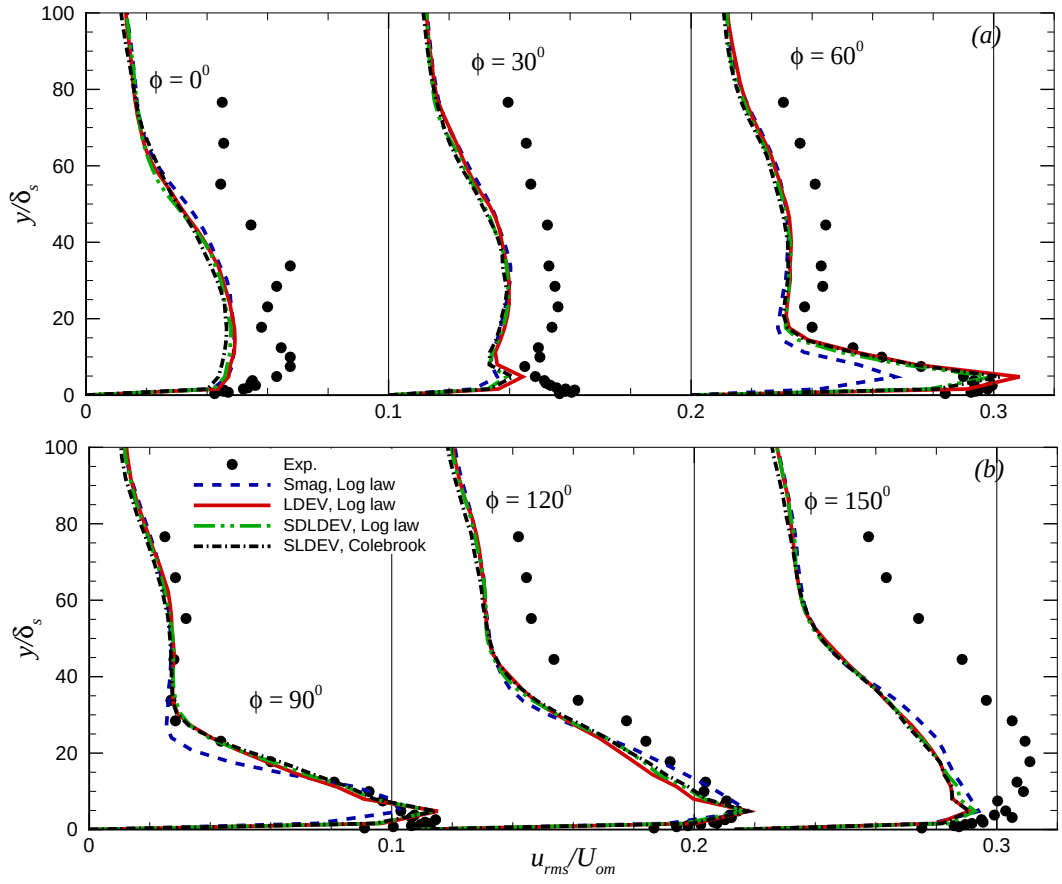

Figure 6.11: Wall-normal turbulence intensity, rough wall. *(a)* $\phi = 0^0$, 30^0 and 60^0; *(b)* $\phi = 90^0$, 120^0 and 150^0. Each profile is shifted by 0.1 units horizontally for clarity.

eddy viscosity, which allows the inner layer to adjust more rapidly to the freestream changes. The logarithmic boundary conditions also gave reasonably accurate results, although use of the MKP modification, which includes a shift between the velocity at the first outer-layer point and the wall stress to account for the inclination of the near-wall eddies and amplifies the wall-stress fluctuations, gave marginally better results. A calculation of the oscillating flow over a rough wall was also performed, and accurate results were obtained with the same models. Transitional roughness effects did not appear to be important.

Chapter 7

Concluding Remarks

7.1 Conclusions

Large-eddy simulation with various wall-layer models and RANS computations have been performed for four non-equilibrium flows. None of the RANS models tested is capable of predicting the flow field accurately when shallow separation is present. The SST model gives reasonable prediction of the mean velocity in the separation region but all models predict a slower recovery. The SA-RANS model and the $k-\epsilon$ model give similar results in attached flows with pressure gradient and curvature effects. A Reynolds stress transport model predicts the Reynolds stresses accurately whereas the SST model and the SA-RANS under-predict Reynolds stresses in attached flows with curvature effects. From the performance of various RANS models, it can be observed that a RANS model that performs well in one flow condition does not always perform well when the flow condition is altered. Different RANS models give the best results in each of the configurations examined.

Large-eddy simulation that uses log-law boundary condition requires the first point in the wall-normal direction to be in the equilibrium region. This results in insufficient resolution to resolve shallow separation and poor prediction of the flow

field. In flow over the two- and three-dimensional bump, on the other hand, since the non-equilibrium effects due to curvature and pressure gradient effects were mild, LES based on log-law boundary condition give excellent prediction. In the oscillating flow tested where the log-law is satisfied during most of the time period, dynamic models with log-law boundary condition gives excellent prediction of the flow field. This suggests that for flows in which the log-law is satisfied or the non-equilibrium effects are mild, LES based on the log-law boundary gives accurate results at a lower computational cost compared to WMLES.

The accuracy of WMLES depends on the generation of resolved eddies at the RANS/LES interface. In regions of flows subjected to concave curvature or adverse-pressure-gradient effects or in separation region, the generation of resolved eddies at the RANS/LES interface is accelerated by the instability of the mean flow; this results in improved prediction of the flow field and also downstream of this region. When WMLES is performed with the addition of stochastic forcing, the generation of resolved eddies is accelerated in equilibrium regions also and results in good prediction of the flow field everywhere. In flows in complex-geometry with mild non-equilibrium effects, WMLES gives accurate results with the addition of the stochastic forcing. In flows with shallow separation, WMLES gives better results than LES with log-law boundary condition and should be the preferred model. However, in oscillating flows, WMLES is excessively dissipative and does not predict the flow development (especially the laminarization effects) accurately. LES with

log-law boundary condition should be used for oscillating flows.

7.2 Future directions

We found the WMLES with stochastic forcing to be the most accurate approach for flows with separation. However, the amplitude of the stochastic forcing had to be set to zero on convex regions of the flow to avoid instability of the simulation. A modification to the dynamic controller which is robust and does not need this ad hoc tuning of the controller is needed before this method can be applied to complex engineering problems. For geophysical flow, where the flow is oscillatory, application of the stochastic forcing based on dynamic controller is infeasible due to the high computational cost needed for the controller to stabilize at the required level of stochastic forcing for various phases of the flow. A different strategy that can predict the required level of the stochastic forcing based on the resolved flow field without any dynamic adjustment and independent of the grid resolution or the time step is needed for the WMLES to be applicable to geophysical flows. Fortunately, if the geometry induced secondary strain rate is low, wall-layer models based on equilibrium flows can give good prediction for this type of flows.

The stochastic forcing method used in this work applies the forcing at the smallest resolved scales where the dissipative action of the viscosity is the largest and might not be very efficient in generating resolved fluctuations. A modification of forcing method that applies the forcing at larger scales compared to the grid spacing

might be more efficient in generating resolved scales. A method that applies forcing at larger scale can be based on the existing resolved fluctuations and should be explored. Another aspect that needs to be explored is the accuracy of the WMLES prediction when the flow development is coupled to a scalar field such as temperature or salinity which happens in oceanographic applications. For this type of problems, it remains to be seen if the application of stochastic forcing at the RANS/LES interface is sufficient to generate resolved scalar fluctuations at the interface or if additional treatment is needed for the scalar field.

Bibliography

[1] Akhavan, R., Kamm, R. D., and Shapiro, A. H. An investigation of transition to turbulence in bounded oscillatory Stokes flows. Part 1. Experiments. *Journal of Fluid Mechanics 225* (1991), 395–422.

[2] Akhavan, R., Kamm, R. D., and Shapiro, A. H. An investigation of transition to turbulence in bounded oscillatory Stokes flows. Part 2. Numerical simulations. *Journal of Fluid Mechanics 225* (1991), 423–444.

[3] Alving, A. E., and Fernholz, H. H. Turbulence measurements around a mild separation bubble and downstream of reattachment. *Journal of Fluid Mechanics 322* (1996), 297–328.

[4] Armenio, V., and Piomelli, U. A lagrangian mixed subgrid-scale model in generalized coordinates. *Flow, Turbulence and Combustion 65* (2000), 51–81.

[5] Aubertine, C. D., and Eaton, J. K. Turbulence development in a non-equilibrium turbulent boundary layer with mild adverse pressure gradient. *Journal of Fluid Mechanics 532* (June 2005), 345–364.

[6] Baggett, J. On the feasibility of merging LES with RANS in the near-wall region of attached turbulent flows. Tech. rep., Center for Turbulent Research, Annual Research Briefs, Stanford University, 1998.

[7] Balaras, E., and Benocci, C. Subgrid scale models in finite difference simulations of complex wall bounded flows. In *AGARD, Application of Direct and Large Eddy Simulation to Transition and Turbulence* (Dec. 1994), J. K. Kaldellis and G. A. Georgantopoulos, Eds.

[8] Balaras, E., Benocci, C., and Piomelli, U. Two layer approximate boundary conditions for large-eddy simulations. *AIAA Journal 34* (1996), 1111–1119.

[9] Bandyopadhyay, P. R., and Ahmed, A. Turbulent boundary layers subjected to multiple curvatures and pressure gradients. *Journal of Fluid Mechanics 246* (Jan. 1993), 503–527.

[10] Barlow, R. S., and Johnston, J. P. Structure of a turbulent boundary layer on a concave surface. *Journal of Fluid Mechanics 191* (June 1988), 137–176.

[11] Baskaran, V., Smits, A. J., and Joubert, P. N. A turbulent flow over a curved hill. I - Growth of an internal boundary layer. *Journal of Fluid Mechanics 182* (Sept. 1987), 47–83.

[12] Baskaran, V., Smits, A. J., and Joubert, P. N. A turbulent flow over a curved hill. II - Effects of streamline curvature and streamwise pressure gradient. *Journal of Fluid Mechanics 232* (Nov. 1991), 377–402.

[13] Bou-Zeid, E., Meneveau, C., and Parlange, M. A scale-dependent Lagrangian dynamic model for large eddy simulation of complex turbulent flows. *Physics of Fluids 17* (Feb. 2005), 0251051–18.

[14] Boussinesq, J. Théorie de Í écoulement Tourbillant. *Mem. Présentés par Divers Savants Acad. Sci. Inst. Fr 23* (1877), 46–50.

[15] Bradshaw, P. Turbulent secondary flows. *Annual Review of Fluid Mechanics 19* (1987), 53–74.

[16] Bradshaw, P., and Pontikos, N. S. Measurements in the turbulent boundary layer on an 'infinite' swept wing. *Journal of Fluid Mechanics 159* (1985), 105–130.

[17] Bradshaw, P., and Wong, F. Y. F. The reattachment and relaxation of a turbulent shear layer. *Journal of Fluid Mechanics 52* (1972), 113–135.

[18] Cabot, W. H. Near-wall models in large eddy simulations of flow behind a backward-facing step. Tech. rep., Center for Turbulence Research, Stanford University, California., 1996.

[19] Cabot, W. H., and Moin, P. Approximate wall boundary conditions in the large-eddy simulation of high reynolds number flows. *Flow, Turbulence and Combustion 63* (2000), 269–291.

[20] Canuto, C., Hussaini, M., Quarteroni, A., and Zang, T. *Spectral Methods in Fluid Dynamics*. Springer Verlag, 1988.

[21] Castro, I. P., and Haque, A. The structure of a turbulent shear layer bounding a separation region. *Journal of Fluid Mechanics 179* (June 1987), 439–468.

[22] Chandrsuda, C., and Bradshaw, P. Turbulence structure of a reattaching mixing layer. *Journal of Fluid Mechanics 110* (Sept. 1981), 171–194.

[23] Chapman, D. R. Computational aerodynamics development and outlook. *AIAA Journal 17* (1979), 1293–1313.

[24] Chen, H., and Patel, V. Near-wall turbulence models for complex flows including separation. *AIAA Journal 26* (1988), 641–648.

[25] Chow, F. K., and Moin, P. A further study of numerical errors in large-eddy simulations. *Journal of Computational Physics 184* (2003), 366–380.

[26] Colebrook, C. F. Turbulent flow in pipes with particular reference to the transition region between smooth- and rough-pipe laws. *J. Inst. Civ. Eng. 11* (1939), 133–156.

[27] Coleman, G., Kim, J., and Le, A.-T. A numerical study of three-dimensional wall-bounded flows. *International journal of heat and fluid flow 17* (1996), 333–342.

[28] Daly, B. J., and Harlow, F. H. Transport Equations in Turbulence. *Physics of Fluids 13* (1970), 2634–49.

[29] Davidson, L., and Billson, M. Hybrid LES-RANS using synthesized turbulent fluctuations for forcing in the interface region. *International journal of heat and fluid flow 27* (2006), 1028–1042.

[30] Davidson, L., and Dahlström, S. Hybrid LES-RANS: an approach to make LES applicable at high reynolds number. *International Journal of Computational Fluid Dynamics 19* (2005), 415–427.

[31] Davidson, L., and Peng, S. Hybrid LES-RANS modelling: a one equation sgs model combined with a $k-omega$ model for predicting recirculating flows. *International Journal for Numerical Methods in Fuids 43* (2003), 1003–1018.

[32] Deardorff, J. W. A numerical study of three-dimensional turbulent channel flow at large Reynolds numbers. *Journal of Fluid Mechanics 41* (1970), 453–480.

[33] DeGraaff, D. G. *Reynolds number scaling of the turbulent boundary layer on a flat plate and on a swept and unswept bumps.* PhD thesis, Dept of Mechanical Engg, Stanford University, 1999.

[34] Dengel, P., and Fernholz, H. H. An experimental investigation of an incompressible turbulent boundary layer in the vicinity of separation. *Journal of Fluid Mechanics 212* (Mar. 1990), 615–636.

[35] Diurno, G., Balaras, E., and Piomelli, U. Wall-layer models for LES of separated flows. In *In Modern Simulation Strategies forTurbulent Flows* (Philadelphia, PA, 2001), B. Geurts, Ed., RT Edwards, pp. 207–222.

[36] Driver, D. M., and Seegmiller, H. L. Features of a reattaching turbulent shear layer in divergent channelflow. *AIAA Journal 23*, 2 (1985), 163–171.

[37] Driver, D. M., Seegmiller, H. L., and Marvin, J. G. Time-dependent behavior of a reattaching shear layer. *AIAA Journal 25*, 7 (1987), 914–919.

[38] Dubief, Y., and Delcayre, F. On coherent vortex identification in turbulence. *Journal of Turbulence 1* (2000), 1–22.

[39] Eaton, J. Effects of mean flow three dimensionality on turbulent boundary-layer structure. *AIAA journal 33*, 11 (1995), 2020–2025.

[40] Eaton, J., and Johnston, J. A Review of Research on Subsonic Turbulent Flow Reattachment. *AIAA Journal* (1981).

[41] Fernholz, H. H., and Warnack, D. The effects of a favourable pressure gradient and of the reynolds number on an incompressible axisymmetric turbulent boundary layer. part 1. the turbulent boundary layer. *Journal of Fluid Mechanics 359* (1998), 329–356.

[42] Ferziger, J., and Peric, M. *Computational Methods for Fluid Dynamics*. Springer, 2002.

[43] Germano, M. Turbulence - The filtering approach. *Journal of Fluid Mechanics 238* (1992), 325–336.

[44] Germano, M., Piomelli, U., Moin, P., and Cabot, W. A dynamic subgrid-scale eddy viscosity model. *Physics of Fluids A 3* (1991), 1760–1765.

[45] Ghosal, S. An analysis of numerical errors in large-eddy simulations of turbulence. *Journal of Computational Physics 125* (1996), 187–206.

[46] Gillis, J. C., and Johnston, J. P. Turbulent boundary-layer flow and structure on a convex wall and its redevelopment on a flat wall. *Journal of Fluid Mechanics 135* (Oct. 1983), 123–153.

[47] Grant, W. D., and Madsen, O. S. The continental-shelf bottom boundary layer. *Annual Review of Fluid Mechanics 18* (1986), 265–305.

[48] Grötzbach, G. Direct numerical and large eddy simulation of turbulent channel flows. In *Encyclopedia of Fluid Mechanics* (1987), N. Cheremisinoff, Ed., vol. 6, West Orange, NJ, Gulf Publication, pp. 1337–91.

[49] Hamba, F. A hybrid RANS/LES simulation of turbulent channel flow. *Theoretical and Computational Fluid Dynamics 16* (2003), 387–403.

[50] Hamba, F. A hybrid RANS/LES simulation of high-reynolds-number channel flow using additional filtering at the interface. *Theoretical and Computational Fluid Dynamics 20* (2006), 89–101.

[51] Hino, M., Kashiwayanagi, M., Nakayama, A., and Hara, T. Experiments on the turbulence statistics and the structure of a reciprocating oscillatory flow. *Journal of Fluid Mechanics 131* (1983), 363–400.

[52] Hoffmann, P. H., Muck, K. C., and Bradshaw, P. The effect of concave surface curvature on turbulent boundary layers. *Journal of Fluid Mechanics 161* (Dec. 1985), 371–403.

[53] Hsu, C.-T., Lu, X., and Kwan, M.-K. Les and rans studies of oscillating flows over flat plate. *Journal of Engineering Mechanics 126*, 2 (2000), 186–193.

[54] Hunt, J. C. R., Wray, A. A., and Moin, P. Eddies, streams, and convergence zones in turbulent flows. In *Studying Turbulence Using Numerical Simulation Databases, 2. Proceedings of the 1988 Summer Program p 193-208 (SEE N89-24538 18-34)* (Dec. 1988), pp. 193–208.

[55] Jensen, B. L., Sumer, B. M., and Fredsøe, J. Turbulent oscillatory boundary layers at high reynolds numbers. *Journal of Fluid Mechanics 206* (1989), 265–297.

[56] Jiménez, J. Turbulent flows over rough walls. *Annual Reviews of Fluid Mechanics 36* (2004), 173–196.

[57] Johnston, J., and Flack, K. Review-Advances in three-dimensional turbulent boundary layers with emphasis on the wall-layer regions. *Journal of fluids engineering 118* (1996), 219–232.

[58] Jones, W., and Launder, B. E. The prediction of laminarization with a two-equation model of turbulence. *International Journal of Heat and Mass Transfer 15* (1972), 301–314.

[59] Kannepalli, C., and Piomelli, U. Large-eddy simulation of a three-dimensional shear-driven turbulent boundary layer. *Journal of Fluid Mechanics 423* (2000), 175–203.

[60] Keating, A., and Piomelli, U. A dynamic stochastic forcing method as a wall-layer model for large-eddy simulation. *Journal of Turbulence 7*, 12 (2006), 1–24.

[61] Kiesow, R. O., and Plesniak, M. W. Near-wall physics of a shear-driven three-dimensional turbulent boundary layer with varying crossflow. *Journal of Fluid Mechanics 484* (June 2003), 1–39.

[62] Kim, J., and Moin, P. Application of a fractional step method to incompressible navier-stokes equations. *Journal of Computational Physics 59* (1985), 308–323.

[63] Kolmogorov, A. N. The local structure of turbulence in incompressible viscous fluid for very large Reynolds numbers. *(Doklady) Acad. Sci. SSSR 30* (1941), 301–305.

[64] Kravchenko, A., and Moin, P. On the Effect of Numerical Errors in Large Eddy Simulations of Turbulent Flows. *Journal of Computational Physics 131* (1997), 310–322.

[65] Launder, B. Second-moment closure: present ... and future? *International Journal of Heat and Fluid flow 10*, 4 (1989), 282–300.

[66] Launder, B. E., Reece, G. J., and Rodi, W. Progress in the development of a Reynolds-stress turbulence closure. *Journal of Fluid Mechanics 68* (Apr. 1975), 537–566.

[67] Launder, B. E., and Sharma, B. I. Application of the energy-dissipation model of turbulence to the calculation of flow near a spinning disc. *Letters Heat Mass Transfer 1* (Dec. 1974), 131–137.

[68] Le, H., Moin, P., and Kim, J. Direct numerical simulation of turbulent flow over a backward-facing step. *Journal of Fluid Mechanics 330* (1997), 349–374.

[69] Leonard, A. Energy cascade in large-eddy simulations of turbulent fluid flows. *Advances in Geophysics 18A* (1974), 237–248.

[70] Lilly, D. K. The representation of small scale turbulence in numerical simulation experiments. In *Proceedings of the IBM Scientific Computing Symposium on Environmental Sciences* (1967), pp. 195–210.

[71] Lilly, D. K. A proposed modification of the Germano subgrid-scale closure method. *Physics of Fluids 4* (Mar. 1992), 633–635.

[72] Lohmann, I. P., Fredsøe, J., Sumer, B. M., and Christensen, E. D. Large eddy simulation of the ventilated wave boundary layer. *Journal of Geophysical Research 111*, C06036 (2006), 1–21.

[73] Lund, T. S. The use of explicit filters in large-eddy simulations. *Computers and Mathematics with Applications 46* (2003), 603–616.

[74] Lund, T. S., and Moin, P. Large-eddy simulation of a concave boundary layer. *International Journal of Heat and Fluid Flow 17* (1996), 290–295.

[75] Lund, T. S., Wu, X., and Squires, K. D. Generation of inflow data for spatially-developing boundary layer simulations. *Journal of Computational Physics 140* (1998), 233–258.

[76] Marusic, I., Kunkel, G. J., and Porté-Agel, F. Experimental study of wall boundary conditions for large-eddy simulation. *Journal of Fluid Mechanics 446* (Nov. 2001), 309–320.

[77] Mellor, G. Oscillatory bottom boundary layers. *Journal of Physical Oceanography 32*, 11 (2002), 3075–3088.

[78] Meneveau, C., and Lund, T. S. The dynamic smagorinsky model and scale-dependent coefficients in the viscous range of turbulence. *Physics of Fluids 9* (1997), 3932–3934.

[79] Meneveau, C., Lund, T. S., and Cabot, W. H. A lagrangian dynamic subgrid-scale model of turbulence. *Journal of Fluid Mechanics 319* (1996), 353–385.

[80] Menter, F. R. Two-equation eddy-viscosity turbulence models for engineering applications. *AIAA Journal 32*, 8 (1994), 1598–1605.

[81] Moin, P. *Fundamentals of Engineering Numerical Analysis*. Cambridge University Press, 2001.

[82] Moin, P., and Kim, J. Numerical investigation of turbulent channel flow. *Journal of fluid mechanics 118* (1982), 341–377.

[83] Moin, P., and Mahesh, K. Direct Numerical Simulation: A Tool in Turbulence Research. *Annual Review of Fluid Mechanics 30* (1998), 539–578.

[84] Moin, P., Shih, T.-H., Driver, D., and Mansour, N. N. Direct numerical simulation of a three-dimensional turbulent boundary layer. *Physics of Fluids 2* (Oct. 1990), 1846–1853.

[85] Morinishi, Y., Lund, T., Vasilyev, O., and Moin, P. Fully Conservative Higher Order Finite Difference Schemes for Incompressible Flow. *Journal of Computational Physics 143*, 1 (1998), 90–124.

[86] Moser, R. D., and Moin, P. The effects of curvature in wall-bounded turbulent flows. *Journal of Fluid Mechanics 175* (1987), 479–510.

[87] Muck, K. C., Hoffmann, P. H., and Bradshaw, P. The effect of convex surface curvature on turbulent boundary layers. *Journal of Fluid Mechanics 161* (Dec. 1985), 347–369.

[88] Na, Y., and Moin, P. Direct numerical simulation of a separated turbulent boundary layer. *Journal of Fluid Mechanics 374* (1998), 379–405.

[89] Nicoud, F., Baggett, J. S., Moin, P., and Cabot, W. Large eddy simulation wall-modeling based on suboptimal control theory and linear stochastic estimation. *Physics of Fluids 13* (Oct. 2001), 2968–2984.

[90] Nikitin, N. V., Nicoud, F., Wasistho, B., Squires, K. D., and Spalart, P. R. An approach to wall modeling in large-eddy simulations. *Physics of Fluids 12* (2000), 1629–1632.

[91] Orlanski, I. A simple boundary condition for unbounded hyperbolic flows. *Journal of Computational Physics 21* (1976), 251–269.

[92] Patel, V., and Sotiropoulos, F. Longitudinal curvature effects in turbulent boundary layers. *Progress in Aerospace Sciences 33* (1997), 1–70.

[93] Patel, V. C. Calibration of the Preston tube and limitations on its use in pressure gradients. *Journal of Fluid Mechanics 23* (1965), 185–208.

[94] Patel, V. C., and Head, M. R. Reversion of turbulent to laminar flow. *Journal of Fluid Mechanics 34* (1968), 371–392.

[95] Piomelli, U., and Balaras, E. Wall-layer models for large-eddy simulations. *Annual Reviews of Fluid Mechanics 34* (2002), 349–374.

[96] Piomelli, U., Balaras, E., Pasinato, H., Squires, K. D., and Spalart, P. R. The inner-outer layer interface in large-eddy simulations with wall-layer models. *International Journal of Heat and Fluid Flow 24* (2003), 538–550.

[97] Piomelli, U., Ferziger, J. H., Moin, P., and Kim, J. New approximate boundary conditions for large eddy simulations of wall-bounded flows. *Physics of Fluids 1* (1989), 1061–1068.

[98] Piomelli, U., Zang, T. A., Speziale, C. G., and Hussaini, M. Y. On the large-eddy simulation of transitional wall-bounded flows. *Physics of Fluids A 2*, 2 (1990), 257–265.

[99] Porté-Agel, F., Meneveau, C., and Parlange, M. B. A scale-dependent dynamic model for large-eddy simulation: application to a neutral atmospheric boundary layer. *Journal of Fluid Mechanics 415* (2000), 261–284.

[100] Ramaprian, B. R., and Shivaprasad, B. G. The structure of turbulent boundary layers along mildly curved surfaces. *Journal of Fluid Mechanics 85* (Mar. 1978), 273–303.

[101] Reynolds, W. C. The potential and limitations of direct and large eddy simulations. In *Whither Turbulence? Turbulence at the Crossroads* (1990), J. L. Lumley, Ed., vol. 357 of *Lecture Notes in Physics, Berlin Springer Verlag*, pp. 313–343.

[102] Rhie, C., and Chow, W. Numerical study of the turbulent flow past an airfoil with trailing edge separation. *AIAA Journal 21* (1983), 1525–1532.

[103] Robinson, S. K. Coherent motions in the turbulent boundary layer. *Annual Review of Fluid Mechanics 23* (1991), 601–639.

[104] Saffman, P., and Wilcox, D. Turbulence-model predictions for turbulent boundary layers. *AIAA Journal 12*, 4 (1974), 541–546.

[105] Salon, S., Armenio, V., and Crise, A. A numerical investigation of the stokes boundary layer in the turbulent regime. *Journal of Fluid Mechanics 570* (2007), 253–296.

[106] Sarpkaya, T. Coherent structures in oscillatory boundary layers. *Journal of Fluid Mechanics 253* (1993), 105–140.

[107] Schumann, U. Subgrid-scale model for finite difference simulation of turbulent flows in plane channels and annuli. *Journal of Computational Physics 18* (1975), 376–404.

[108] Shiloh, K., Shivaprasad, B. G., and Simpson, R. L. The structure of a separating turbulent boundary layer. Part 3. Transverse velocity measurements. *Journal of Fluid Mechanics 113* (Dec. 1981), 75–90.

[109] Silva Lopes, A., and Palma, J. M. L. M. Simulations of isotropic turbulence using a non-orthogonal grid system. *Journal of Computational Physics 175*, 2 (2002), 713–738.

[110] Silva Lopes, A., Piomelli, U., and Palma, J. M. L. M. Large-eddy simulation of the flow in an s-duct. *Journal of Turbulence 7*, 11 (2006), 1–24.

[111] Simpson, R. L. Turbulent boundary-layer separation. *Annual Review of Fluid Mechanics 21* (1989), 205–234.

[112] Simpson, R. L. Aspects of turbulent boundary-layer separation. *Progress in Aerospace Sciences 32* (Oct. 1996), 457–521.

[113] Simpson, R. L., Chew, Y.-T., and Shivaprasad, B. G. The structure of a separating turbulent boundary layer. Part 1. Mean flow and Reynolds stresses. *Journal of Fluid Mechanics 113* (Dec. 1981), 23–51.

[114] Simpson, R. L., Chew, Y.-T., and Shivaprasad, B. G. The structure of a separating turbulent boundary layer. Part 2. Higher- order turbulence results. *Journal of Fluid Mechanics 113* (1981), 53–73.

[115] Sleath, J. F. A. Turbulent oscillatory flow over rough beds. *Journal of Fluid Mechanics 182* (1987), 369–409.

[116] Smagorinsky, J. General circulation experiments with the primitive equations I. The basic experiment. *Monthly Weather Review 91* (1963), 99–164.

[117] Smits, A. J., and Wood, D. H. The response of turbulent boundary layers to sudden pertubations. *Annual Review of Fluid Mechanics 17* (1985), 321–358.

[118] Smits, A. J., Young, S. T. B., and Bradshaw, P. The effect of short regions of high surface curvature on turbulent boundary layers. *Journal of fluid mechanics 94* (1979), 209–242.

[119] So, R., and Mellor, G. An experimental investigation of turbulent boundary layers along curved surfaces. Tech. Rep. NASA-CR-1940, NASA, 1972.

[120] So, R. M. C., and Mellor, G. L. Experiment on convex curvature effects in turbulent boundary layers. *Journal of Fluid Mechanics 60* (1973), 43–62.

[121] So, R. M. C., and Mellor, G. L. Experiment on turbulent boundary layers on a concave wall. *Aeronautical Quarterly 26* (Feb. 1975), 25–40.

[122] Song, S. *Reynolds number effects on a turbulent boundary layer with separation, reattachment and recovery.* PhD thesis, Stanford University, Dept of Mechanical engineering, 2002.

[123] Song, S., DeGraaff, D., and Eaton, J. K. Experimental study of a separating, reattaching and redeveloping flow over a smoothly contoured ramp. *International Journal of Heat and Fluid Flow 21* (2000), 512–529.

[124] Song, S., and Eaton, J. K. Reynolds number effects on a turbulent boundary layer with separation, reattachment, and recovery. *Experiments in Fluids 36* (2004), 246–258.

[125] Spalart, P., and Allmaras, S. A one-equation turbulence model for aerodynamic flows. *La Recherche Aérospatiale 1* (1994), 5–21.

[126] Spalart, P., and Baldwin, B. Direct simulation of a turbulent oscillating boundary layer. In *Turbulent shear flows 6* (Heidelberg, 1988), J. Andre, J. Cousteix, F. Durst, B. E. Launder, F. W. Schmidt, and J. Whitelaw, Eds., Springer-Verlag, pp. 417–440.

[127] Spalart, P. R., Jou, W. H., Strelets, M. K., and Allmaras, S. R. Comments on the feasibility of les for wings, and on a hybrid rans/les approach. In *Advances in DNS/LES* (Columbus, OH, 1997), C. Liu and Z. Liu, Eds., Greyden Press, pp. 137–148.

[128] Stokes, G. G. On the effect of the internal friction of fluids on the motion of pendulums. *Cambr Phil Tran 9*, 8-106 (1851).

[129] Stoll, R., and Porté-Agel, F. Effect of Roughness on Surface Boundary Conditions for Large-Eddy Simulation. *Boundary-Layer Meteorology 118* (Jan. 2006), 169–187.

[130] Temmerman, L., Hadziabdic, M., Leschziner, M. A., and Hanjalic, K. A hybrid two-layer URANS-LES approach for large eddy simulation at high reynolds numbers. *International Journal of Heat and Fluid Flow 26* (2005), 173–190.

[131] Templeton, J. A., Wang, M., and Moin, P. An efficient wall model for large-eddy simulation based on optimal control theory. *Physics of Fluids 18* (Feb. 2006), 5101.

[132] Tsuji, Y., and Morikawa, Y. Turbulent boundary layer with pressure gradient alternating in sign. *Aeronautical Quarterly 27* (Feb. 1976), 15–28.

[133] van Driest, E. On turbulent flow near a wall. *Journal of Aerospace Sciences 23* (1956), 1007–1011.

[134] Verzicco, R., and Vittori, G. Direct simulation of transition in stokes boundary layers. *Physics of Fluids 8*, 6 (1996), 1341–1343.

[135] Vittori, G., and Verzicco, R. Direct simulation of transition in an oscillatory boundary layer. *Journal of Fluid Mechanics 371* (1998), 207–232.

[136] Vreman, B., Geurts, B., and Kuerten, H. On the formulation of the dynamic mixed subgrid-scale model. *Physics of Fluids 6* (Dec. 1994), 4057–4059.

[137] Webster, D., DeGraaff, D. B., and Eaton, J. K. Turbulence characteristics of a boundary layer over a two-dimensional bump. *Journal of Fluid Mechanics 320* (1996), 53–69.

[138] Webster, D. R., Degraaff, D. B., and Eaton, J. K. Turbulence characteristics of a boundary layer over a swept bump. *Journal of Fluid Mechanics 323* (1996), 1–22.

[139] Wu, X., and Squires, K. D. Numerical investigation of the turbulent boundary layer over a bump. *Journal of Fluid Mechanics 362* (1998), 229–271.

[140] Wu, X., and Squires, K. D. Prediction of the High-Reynolds-Number Flow over a Two-Dimensional Bump. *AIAA Journal 36* (1998), 799–808.

[141] Wu, X., and Squires, K. D. Prediction of the three-dimensional turbulent boundary layer over a swept bump. *AIAA Journal 36*, 4 (1998), 505–514.

[142] Yoshizawa, A. A bridging between eddy-viscosity type and second-order models using a two-scale DIA. In *9th International Symposium on Turbulent Shear Flow* (Kyoto, 1993), vol. 3.

[143] Zang, Y., Street, R. L., and Koseff, J. R. A dynamic mixed subgrid-scale model and its application to turbulent recirculating flows. *Physics of Fluids 5* (Dec. 1993), 3186–3196.